University of Crete

“Nitride polariton structures with improved characteristics”

by
Emmanouil Amargianitakis

submitted to

Department of Physics

in partial fulfillment of the requirements for M.Sc. degree in
Micro/Optoelectronics

Supervisors
Alexandros Georgakilas
Nikos Pelekanos

Examination committee
Alexandros Georgakilas
Nikos Pelekanos
Zacharias Hatzopoulos

February 2016, Heraklion

Περίληψη

Τις τελευταίες δεκαετίες υπάρχει μια έντονη ερευνητική δραστηριότητα στη δημιουργία και το σχεδιασμό μικροκοιλοτήτων από νιτρίδια ημιαγωγών III-V. Ο λόγος είναι ότι επιτρέπουν την μελέτη θεμελιωδών αλληλεπιδράσεων του μπλε φωτός με την ύλη, όταν οι ηλεκτρονικές καταστάσεις και το ηλεκτρομαγνητικό πεδίο περιορίζονται σε μία διάσταση. Όπως φανερώνει το όνομά τους, οι μικροκοιλότητες είναι οπτικές κοιλότητες που έχουν πάχος συγκρίσιμο με το μήκος κύματος του φωτός και μπορούν να παγιδεύουν φωτόνια συγκεκριμένου μήκους κύματος μέσα τους. Εάν τοποθετήσουμε σαν ενεργό υλικό ένα κβαντικό πηγάδι (QW), που εκπέμπει/απορροφάει στο ίδιο μήκος κύματος με τον τρόπο ταλάντωσης της μικροκοιλότητας που είναι ενσωματωμένο μέσα, τότε η ενέργεια "ταλαντεύεται" μεταξύ του φωτονίου της κοιλότητας και της γνωστής εξιτονικής κατάστασης. Εάν αυτή η σύζευξη είναι ταχύτερη από άλλες διεργασίες μέσα στη κοιλότητα τότε η διάκριση μεταξύ του φωτονίου και του εξιτονίου χάνεται, και νέα οιονεί-σωματίδια δημιουργούνται. Αυτές οι νέες καταστάσεις, για τις οποίες έχει καθιερωθεί η ονομασία "πολαριτόνια", αποτελούνται από μισή-ύλη και μισό-φως και περιγράφουν την αλληλεπίδραση μεταξύ εξιτονίων και φωτονίων με την ίδια ενέργεια και ορμή.

Παρόμοια με τις μικροκοιλότητες, οπτικά αντηχεία σε σχήμα μικροδίσκων έχουν βρεθεί επίσης να εμφανίζουν χαμηλές απώλειες και υψηλούς παράγοντες ποιότητας (Q-factors) λόγω του μικρού όγκου τους και χωρίς την ανάγκη κατασκευής καθρεφτών DBR. Στις κυκλικές κοιλότητες, όπως και στους μικροδίσκους, είναι γνωστό ότι μπορούν να διεγερθούν οι λεγόμενοι "Whispering Gallery Modes" τρόποι ταλάντωσης που είχαν παρατηρηθεί για πρώτη φορά από τον Λόρδο Rayleigh το 1878. Αυτοί οι τρόποι διέγερσης προσφέρουν τη δυνατότητα για την εξερεύνηση της ισχυρής σύζευξης, και ως εκ τούτου, είναι ιδανικοί υποψήφιοι για τη επίτευξη λέιζερ ακόμη χαμηλότερης κατανάλωσης. Το κύριο μειονέκτημα αυτών των δομών είναι η δυσκολία στην κατασκευή τους, δεδομένου ότι μικρές αποκλίσεις στα πλευρικά τοιχώματα, καθώς και μεγάλη τραχύτητα των επιφανειών τους, μπορεί να οδηγήσουν σε υψηλές οπτικές απώλειες.

Οι πολαριτονικές συσκευές είναι εφικτό να χρησιμοποιηθούν και ως εκπομποί σύμφωνου φωτός, αφού ο σύνθετος μποζονικός χαρακτήρας είναι υπεύθυνος για την εξαναγκασμένη σκέδαση τους, η οποία οδηγεί σε χαλάρωσή τους στην χαμηλότερη ενεργειακή κατάσταση. Αυτή η αλληλεπίδραση, για σωματίδια με ακέραιο σπίν, είναι γνωστή ως συμπύκνωση Bose - Einstein (BEC). Αυτό σημαίνει ότι σε ένα πολαριτονικό λέιζερ η αναστροφή των πληθυσμών δεν είναι πλέον απαραίτητη με αποτέλεσμα να έχουν χαμηλότερα κατώφλια λειτουργίας. Πρόσφατα, οι Schneider et al. κατασκεύασαν ένα InGaAs/GaAs πολαριτονικό λέιζερ, που λειτουργεί με ηλεκτρική έγχυση φορέων σε χαμηλές θερμοκρασίες, ενώ οι Bhattacharya et al. κατάφεραν να πετύχουν λειτουργία σε θερμοκρασία δωματίου χρησιμοποιώντας το GaN ως ενεργό υλικό με κατανάλωση πυκνότητας ρεύματος 169 A cm $^{-2}$.

Ο σκοπός αυτής της εργασίας ήταν ο σχεδιασμός και η κατασκευή μεμβρανών πάχους $3\lambda_c/2$ από υψηλής ποιότητας AlGaN, χρησιμοποιώντας τη Φωτο-ηλεκτροχημική εγχάραξη (PEC etching) για την αφαίρεση ενός στρώματος InGaN, και η χρήση τους ως ενεργό υλικό στις μικροκοιλότητες. Η κεντρική ιδέα ήταν να ενσωματωθούν δύο σετ από 4 GaN/AlGaN QWs μέσα στις AlGaN μεμβράνες, στις περιοχές των μεγίστων του ηλεκτρικού πεδίου, για τη διερεύνηση της ισχυρής σύζευξης όταν αυτές τοποθετηθούν ανάμεσα σε δύο DBR καθρέφτες. Επιπλέον, έγινε μια πρώτη προσπάθεια για να κατασκευαστούν μικροδίσκοι διαφορετικών μεγεθών, με βάση την ίδια τεχνική, ώστε να γίνει

εξερεύνηση των WGMs.Η συγκέντρωση του Al στο AlGaN διατηρήθηκε σε χαμηλά επίπεδα ώστε να μειωθούν όσο το δυνατόν περισότερο οι αναντιστοιχίες στις πλεγματικές σταθερές μεταξύ των δυο υλικών. Η τεχνική ανάπτυξης των δειγμάτων ήταν η επίταξη με μοριακές δέσμες (MBE) πάνω σε υποστρώματα c-GaN/c-Sapphire από την ομάδα CEA στη Γαλλία.

Στα δείγματα που λάβαμε πραγματοποιήθηκαν μετρήσεις περίθλασης ακτίνων Χ (XRD) και, στη συνέχεια, χαρακτηρίστηκαν με φωτοφωταύγεια και ανακλαστικότητα με τη χρήση ενός κρυοστάτη συνδεδεμένου με ένα ρυθμιστή θερμοκρασίας. Η διέγερση των δομών έγινε με ένα λέιζερ συνεχούς λειτουργίας στα 325 nm και μια πηγή λευκού φωτός, αντίστοιχα. Χρησιμοποιώντας τη προσέγγιση της ενεργού μάζας και τη θεωρία της k.p διαταραχής έγινε προσομοίωση των εξιτονικών ενεργειακών καταστάσεων A_x, B_x και C_x μέσα στα GaN/AlGaN QWs με χρήση του λογισμικού Nextnano. Παράλληλα, έγινε ανάλυση ενός εύρους θερμοκρασιών με βάση την εμπειρική σχέση Varshni και λαμβάνοντας υπόψη το επαγόμενο πεδίο εξαιτίας των φορτίων πόλωσης στις διεπαφές των κβαντικών πηγαδιών, σε σύγκριση με τις κορυφές από PL μετρήσεις για την ίδιες θερμοκρασίες. Οι παράμετροι Varshni που χρησιμοποιήθηκαν στις προσομοιώσεις εξήχθησαν από τα πειραματικά δεδομένα. Επιπλέον, στα δείγματά μας παρατηρήθηκε μια συμπεριφορά "S-σχήματος", όπου αποδίδεται σε παγιδευμένα εξιτόνια σε αρκετά χαμηλές θερμοκρασίες (T <100 K) και εξήχθησαν οι ενέργειες εντοπισμού τους.

Στη συνέχεια, με τη χρήση της τεχνικής Reactive Ion Etching (RIE), κατασκευάστηκαν τετραγωνικά και κυλινδρικά μοτίβα στα δείγματά μας για τη δημιουργία μεμβρανών και μικροδίσκων διαφόρων μεγεθών. Στη διαδικασία PEC, χρησιμοποιήθηκε ένα διοδικό λέιζερ στα 405 nm για την επιλεκτική εγχάραξη του στρώματος InGaN. Έπειτα, οι μεμβράνες μεταφέρθηκαν στα bottom-DBR/Sapphire υποστρώματα φτιαγμένα με evaporation, αποτελούμενα από εναλλασόμενα ζεύγη υλικών με υψηλό και χαμηλό δείκτη διάθλασης, ώστε να γίνει η εναπόθεση του top-DBR. Αντιθέτως, στους μικροδίσκους δεν είναι αναγκαία η εναπόθεση DBR για την παρατήρηση των WGMs. Για την κατασκευή των top-DBR καθρεφτών, οι δύο μέθοδοι που δοκιμάστηκαν είναι οι rf-sputtering και e-gun evaporation, σε συνεργασία με την ομάδα CEA.

Όσον αφορά την πειραματική ανάλυση των καθρεφτών, έγιναν προσομοιώσεις των φασμάτων ανακλαστικότητας, απορρόφησης και διαπερατότητας με τη χρήση ενός κώδικα Matlab βασιζόμενου στη μέθοδο μεταφοράς πινάκων, γραμμένο από τον Δρ. Rahul Jayaprakash. Οι δείκτες διάθλασης των διηλεκτρικών υλικών των DBR καθρεφτών εξήχθησαν από μετρήσεις Φασματοσκοπικής Ελλειψομετρίας (SE) για πιο ακριβείς προσομοιώσεις. Για το χαρακτηριμό της τραχύτητας των επιφανειών, καθώς και των παχών των μεμβρανών, πραγματοποιήθηκαν μετρήσεις με την τεχνική AFM, όπου παρατηρήθηκαν αποκλίσεις από τις αναμενόμενες τιμές. Μεταξύ των τριών μεθόδων ανάπτυξης καθρεφτών, τα καλύτερα αποτελέσματα ήταν με e-gun evaporation, όπου τα δείγματα βρέθηκε να έχουν αρκετά χαμηλή τραχύτητα και καλή κρυσταλλική ποιότητα.

Παρόλα αυτά, με καμία από τις δύο μεθόδους δεν ήταν δυνατή η επίτευξη της ισχυρής σύζευξης. Στην περίπτωση του rf-sputtering οι μεμβράνες ήταν κατεστραμένες, ενώ με τη μέθοδο του e-gun evaporation οι περισσότερες μεμβράνες βρέθηκε να έχουν κάποια κλίση ως προς το επίπεδο ανάπτυξης των DBR. Περαιτέρω μελέτη με προσομοιώσεις έδειξε πως για διαφορετικές τιμές ενός διάκενου με αέρα κάτω από τις μεμβράνες με κλίση, εξαιτίας οξειδίων ή σπασμένων κομματιών από μεμβράνες, μπορεί να δημιουργήσουν ένα εύρος τρόπων ταλάντωσης μέσα στη κοιλότητα. Από την άλλη μεριά, οι προσομοιώσεις για πάχη των μεμβρανών μεγαλύτερα από τα αναμενόμενα το αποτέλεσμα θα ήταν η μετατόπιση του τρόπου ταλάντωσης προς μεγαλύτερα μήκη κύματος.

Contents

Acknowledgments

First of all, I would like to express my deep gratitude to Professors Alexandros Georgakilas and Nikos Pelekanos for trusting me and approving my placement at “Microelectronics Research Group”, in the field of polariton physics, at the FORTH’s Institute of Electronic Structure and Laser, and for their continuous guidance throughout my project. Moreover, I am grateful to Prof. Zacharias Hatzopoulos, who accepted to be in my examination committee, and especially for his crucial support.

In addition, I would like to offer my special thanks for the assistance given by Dr. Rahul Jayaprakash for his patient guidance, providing me with advices and useful critiques with the experimental setups and understanding any problems that occurred during this research project. I would like also to thank him for giving me access to his Matlab code based on the Transfer Matrix Method theory for simulating my structures.

Many thanks to Dr. Fotis Kalaitzakis for supporting me in any technical and theoretical issue in this field, fabricating mesas on my samples with Reactive Ion Etching technique, and for his aid transferring the free-standing nitride membranes on other substrates for further characterization or deposition of the DBR mirrors. Additionally, I wish to acknowledge the help provided by Ms. Maria Androulidaki for explaining me the principles of the Photoluminescence and Reflectance techniques and how to handle the cryostat that was used for this research.

Special thanks go to Ph.D. student Stelios Kazazis for analyzing my dielectric materials with Spectroscopic Ellipsometry in order to identify the refractive indices and thicknesses, especially for the DBR mirror fabrication, and Ms. Katerina Tsagaraki for doing X-ray Diffraction, Scanning electron microscopy and Atomic Force Microscopy in order to determine the concentrations, thicknesses and surface roughnesses of the layered structures.

To continue, I am particularly grateful to Dr. Babis Katsidis, for his precious aid on teaching me how to perform simulations with Nextnano software, designed by Dr. Stefan Birner, and for his beneficial advices and contribution in the interpretation of my results, regarding exciton states inside the quantum wells, in correspondence to the experimental data.

Furthermore, I would like to thank also the rest of the people in MRG lab for their small or huge contribution to my work and for all the time we spend together. My special thanks are extended to the staff of the CNRS group in France, where they used growth methods for fabricating our high quality nitride samples and for the deposition of the Distributed Bragg Reflectors. Last but not least, I wish to thank my family for their support and encouragement in my decision of pursuing a Master’s Degree in Micro/Optoelectronics.

1. Abstract

Over the last decades, there has been an intensive research in the field of strong light-matter coupling in III-V nitride semiconductor microcavities. The reason is that they allow performing fundamental studies of blue light-matter interaction when electronic states and electromagnetic field are confined in one dimension. As their name reveals, microcavities are wavelength-sized optical cavities that can trap light of a specific wavelength depending on the cavity length [1]. If a layer, such as a quantum well (QW), emitting/absorbing at the same wavelength of the cavity mode that is embedded in, and strong coupling conditions are satisfied, then energy "oscillates" between the cavity photon and the known exciton. The distinction between light and matter is lost if this interaction rate is engineered to be faster than other processes and new quasiparticles are generated. These new quasiparticles, the so-called "polaritons", which are half-light and half-matter, describe the interaction between excitons and photons with the same energy and momentum.

Similar to microcavities, microdisk optical resonators were found also to exhibit low losses and high Q-factors even at room temperature due to small modal volumes without the use of any DBR mirror fabrication [2]. In circular cavities, such as microdisks "whispering gallery modes" can be excited, originally observed for the first time by Lord Rayleigh in 1878. These excitation modes offer the possibility for exploring the strong coupling regime and hence, they are possible candidates for low threshold lasing. The main drawback of these structures is the difficulty in fabrication, since deviations from circularity and sidewall roughness can lead to optical losses. Furthermore, it has been shown that small diameter disks lead to less excited modes, which in combination to excitonic transitions from quantum wells can couple together and perform single mode excitation with sharp peaks and ultra-high Q-factors [3].

Polariton devices can be used as coherent light emitters, since the bosonic character of these quasiparticles is responsible for the stimulated light emission due to relaxation at the ground state. This effect, which is followed by integer spin particles, is known as Bose-Einstein condensation (BEC) [4]. For a polariton laser [5], inversion of populations is no longer necessary for a successful operation, resulting in reduced operating thresholds. Recently, Schneider et al. [6] fabricated an InGaAs/GaAs electrically driven multiple quantum well polariton laser operating at low temperatures, while Bhattacharya et al. [7] managed to reach room temperature operation for a bulk GaN-based microcavity approaching a threshold current density of 169 A cm^{-2}. Nevertheless, there is still space for further improvement in the III-V based nitride systems by implementing quantum wells or quantum dots towards the realization of even lower thresholds at room temperature.

The aim of this project was the design and fabrication of $3\lambda_c/2$ thick high-quality AlGaN membranes by etching a sacrificial InGaN layer, with the use of Photo-electrochemical (PEC) wet etching method, and their use as active material of micro-sized cavities. AlGaN layer had embedded two sets of 4 GaN quantum wells (QWs) at the antinodes of the electric field for investigating the strong coupling regime when the fabricated membranes are sandwiched by two distributed Bragg reflectors (DBRs). The concentration of Al in the AlGaN layer was kept at low levels to reduce any lattice mismatch and strain effects. Moreover, an initial attempt was done towards making various sized microdisks in one of the samples for exploring the well-known whispering gallery modes (WGMs) by the same fabrication

techniques. The growth of our samples was performed by Molecular Beam Epitaxy (MBE) on c-GaN/c-Sapphire substrates by the CEA group in France.

After receiving the samples from France, X-Ray Diffraction (XRD) measurements were utilized for examining any deviations from the theoretically designed structures and, then they were characterized by photoluminescence and reflectivity techniques with the use of a He-cooled cryostat with an attached heater and connected to a temperature meter. The excitation of the structures was done by a He - Cd cw laser and a Deuterium - Halogen white lamp source, respectively. In addition, effective mass approximation [8] and k.p perturbation theory [9] were performed for simulating the A_x, B_x and C_x exciton energy states inside the GaN/AlGaN quantum wells with Nextnano software [10]. Moreover, the simulation analysis was done from low up to elevated temperatures by using Varshni's empirical relation [11] and by taking into account the built-in field induced from the polarization charge at the interfaces of the quantum wells [12], while compared with the obtained PL peaks for the same temperatures. The Varshni parameters used in the simulations were extracted from the experimental data of both samples. Last but not least, in the PL peak energy versus temperature curve, an "S-shape" behavior was observed, which is attributed to delocalization of excitons from confinement potentials at relatively low temperatures (T < 100 K) [13], and a localization energy was derived.

To move on, by using Reactive Ion Etching (RIE) technique for patterning, we created rectangular and cylindrical mesas on our samples, which were later used in the etching process for the creation of free-standing membranes and standing microdisks of various sizes. For the PEC process, a 405 nm diode laser was used for the lateral selective etching of the InGaN layer. Membranes were then transferred on bottom-DBR/Sapphire substrates, made by evaporation method, of alternating pairs of high and low refractive indices and later were sandwiched with top-DBR mirrors. On the other hand, microdisks were not removed from their original substrates, since no mirror deposition is necessary for the observation of WGMs. For the top-DBR deposition, two different methods were tried namely rf-sputtering and e-gun evaporation in collaboration with the CEA group.

For the experimental analysis, simulations of reflectivity spectra were performed with the use of a Matlab code based on the transfer matrix method (TMM) [14], written by Dr. Rahul Jayaprakash, in correspondence to the experimental results for all the DBRs and full microcavity structures. Refractive indices of some dielectric materials were extrapolated from Spectroscopic Ellipsometry (SE) measurements for more accurate simulations. Furthermore, AFM technique was utilized for measuring surface roughnesses and thicknesses of the membranes, which were different than the ones expected. Between the three growing methods, e-gun evaporation exhibited the best results. The samples that were grown by this method showed to have very low roughness and high crystal quality.

Nevertheless, it was not possible to achieve strong coupling in our devices. In the case of rf-sputtering the membranes were found to be cracked, while in the case of e-gun evaporation the membranes were observed to have an inclination in respect to the growth direction, and therefore were not adhered to the bottom-DBR surface. Simulations showed that the varied air-gap thickness due to broken pieces or oxides under the membranes can induce a range of cavity modes inside the cavity, which can lead to a very low quality factor of the microcavity structure. On the contrary, simulations showed that thicker membrane thickness can only shift the cavity mode towards higher wavelengths.

2. Properties of the materials

2.1. GaN, AlN and InN nitrides and their AlGaN and InGaN alloys

Nitride materials are III-V direct bandgap semiconductors, for which the band edge is located at the Γ point, and can be found in two different forms: hexagonal wurtzite (Wz) and zinc blende (ZB) crystal structures [15]. In this project only Wz was under examination, which is the thermodynamically stable state of all the III-V nitrides and is described by two lattice constants α and c. Wz structure consists of two interpenetrating hexagonal close-packed (hcp) sublattices, each with one type of atom, with an offset along the c-axis of 5/8 of the cell height. The biatomic stacking sequence is AaBbAa… in the [0001] direction with 6 atoms in the hexagonal unit cell contained in it.

Due to the lack of an inversion plane perpendicular to the c-axis in Wz III nitrides, nitride surfaces have either a group III element (Al, Ga or In) polarity, named as "Ga-face" polarity, with a designation of $[0001]$, or a "N-face" polarity with a designation of $[000\bar{1}]$. The result of this uniaxial anisotropy due to the wurtzite crystal structure is presented in Figure 2.1. Depending on the growing direction, the polarity of the polarization charge changes. The product of $\mathrm{u.c}$ corresponds to the length of the bonds parallel to $[0001]$ direction, with u the internal parameter equal to 3/8. The electrostatic interactions, arising from the large ionicity, reduce the interlayer ion (N^{3-}) - cation (Ga^{3+}) distances A-b and B-a, and result in increased values of u larger than the ideal value of 3/8. This relative displacement from the ideal structure induces spontaneous polarization (P_{sp}) with high carrier concentrations at the surfaces of the materials.

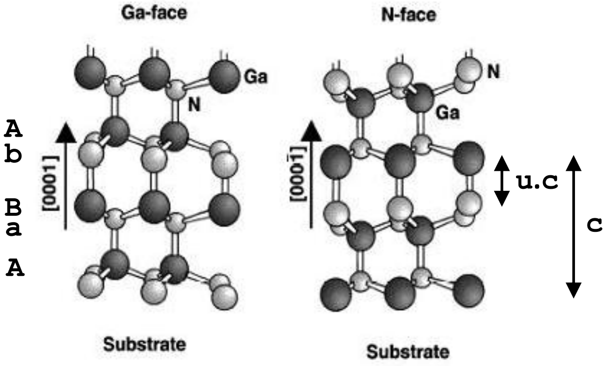

Figure 2.1 Ga-face or N-face polarity depending on the growth direction with c the A-A distance and $\mathrm{u.c}$ corresponding to the length of the bonds parallel to [0001] [16].

Back in 1991, Nakamura [17] managed to grow high quality GaN on Sapphire without the use of Aluminum Nitride (AlN) buffer layer, as did his predecessors. In present, many groups fabricate GaN with low density of threading dislocations (TDs) and low doped films [18; 19]. GaN, which is widely used in "blue" optoelectronic devices, finds many applications in lasers, detectors, displays, high power amplifiers etc. due to the large bandgap and stability at high temperatures. Based on reference [20], GaN wurtzite structure has a direct bandgap (without excitons) of 3.510 eV at 0 K and 3.437 eV at 300 K. Crystal symmetry of wurtzite structure and weak spin-orbit interaction split the valence band to three non-degenerate sub-bands referred to as A (Heavy holes), B (Light holes) and C (Split-off) bands corresponding to the optical transitions of Γ_{9v} crystal-field, upper Γ_{7v} and lower Γ_{7v} spin-orbit split valence bands (Dresselhaus 1957 and Hopfield 1960), as illustrated in Figure 2.2. For each of these bands, an excitonic transition occurs named similarly as A_x, B_x and C_x for thick GaN samples [21]. In Figure 2.3 (b) are depicted the three exciton transitions at T = 77 K.

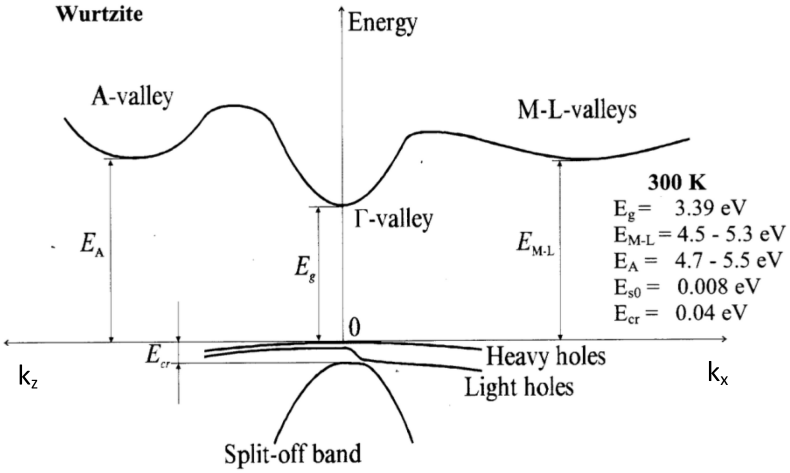

Figure 2.2 Important minima of the conduction band and maxima of the valence band in GaN Wurtzite band structure. Valence band splitting results from crystal symmetry and spin-orbit interaction [22].

Binding energy (E_B) of A_x exciton is ~ 26 meV according to Skromme et al. 1997 and Yamaguchi et al. 1998a. This value is large enough compared with other III-V semiconductors (eg. 4.8 meV for GaAs) exhibiting strong light-matter coupling in microcavities even at room temperature. At 295 K, GaN's exciton linewidth increases up to 25 meV, mainly due to phonon interactions, with the two distinct peaks of the A_x and B_x excitons having a strong overlap. This must be taken into consideration when fabricating room temperature operating devices. On the other hand, C_x exciton shows just a small change in the slope (Muth et al. in 1997).

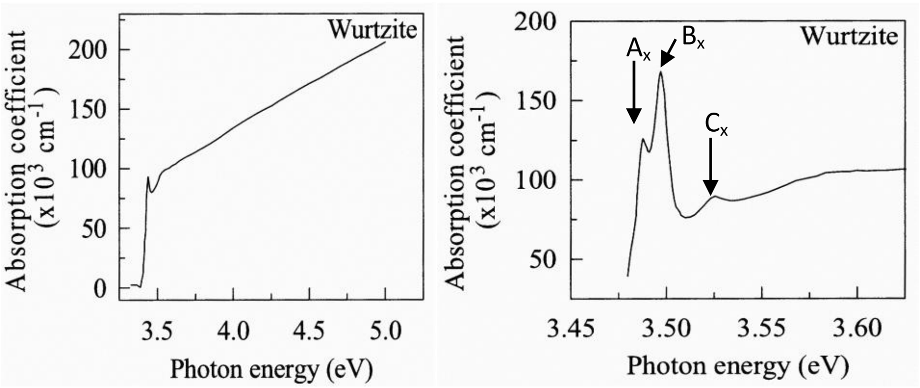

(a) **(b)**

Figure 2.3 Experimental data of bulk wurtzite GaN grown on c-Saphire: (a) Absorption coefficient versus photon energy T = 295 K and (b) Absorption coefficient versus photon energy T = 77 K [23].

Similar to GaN, Aluminum Nitride (AlN) has been also an attractive material due to its high energy gap added to his other outstanding characteristics. Some main properties of AlN are summarized in Table 2.1. By adjusting the concentration of Al, one can synthesize alloys of $Al_xGa_{1-x}N$ by combining AlN and GaN characteristics and lead to fabrication of various band gap semiconductors, which are mainly used as barriers in quantum well structures. As regards Indium Nitride (InN), it is not as famous as its other two relatives, since its low band gap makes it non practical for blue light operation. Hence, its applications are mainly limited to its combination with GaN and AlN to form alloys.

Table 2.1 Material properties of wurtzite GaN, AlN and InN [15; 20]

	GaN	**AlN**	**InN**
E_g(300 K) (eV)	3.437	6.00	0.608
Band gap temperature coefficient $\frac{dE_g}{dT}$ (eV/K)	$-6.0\text{x}10^{-4}$	$-5.1\text{x}10^{-4}$	$-1.8\text{x}10^{-4}$
Lattice constant a (Å)	3.189	3.112	3.545
Lattice constant c (Å)	5.185	4.982	5.703
Thermal expansion Δa/a (1/K)	$5.59\text{x}10^{-6}$	$4.2\text{x}10^{-6}$	$3.8\text{x}10^{-6}$
Thermal expansion Δc/c (1/K)	$3.17\text{x}10^{-6}$	$5.3\text{x}10^{-6}$	$2.9\text{x}10^{-6}$

Going back in 80's, Hagen et al. [24] and Baranov et al. [25] were the first to demonstrate that Al_xGa_xN alloys can be synthesized on a wide range. Nowadays, it is possible to make ternary alloys such as Al_xGa_xN or In_xGa_xN by using different concentrations of Al and In resulting in a range of energy bandgaps and lattice constants covering most of the visible spectrum [26; 27]. Moreover, it has been found that these alloys exhibit also increased sheet charge densities at the $GaN/Al_xGa_{1-x}N$ and $GaN/In_xGa_{1-x}N$ interfaces [28]. In this thesis, $Al_xGa_{1-x}N$ was used as a barrier for the quantum wells, while $In_xGa_{1-x}N$ was used as a sacrificial etching layer in our heterostructure devices. The graph in Figure 2.4 illustrates the bandgap energy (E_g) versus the lattice constant (a) of the III-V nitride materials.

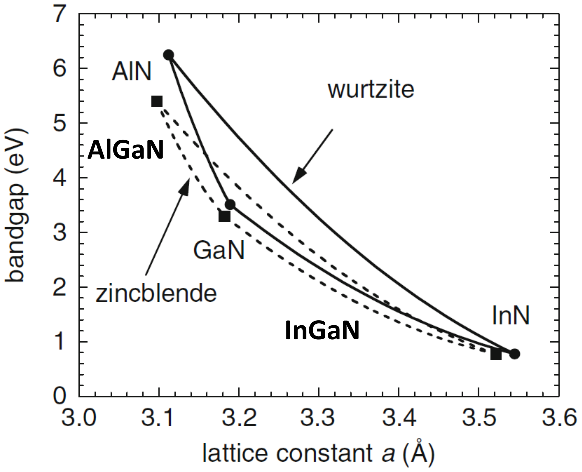

Figure 2.4 Bandgap energy at T = 300K (E_g) versus lattice constant (a) of III-N semiconductors of Wurtzite (solid line) and Zinc Blende (dashed line) structures [29].

By varying the concentration (x) in $Al_xGa_{1-x}N$ and $In_xGa_{1-x}N$ alloys, the desired lattice constant and energy bandgap can be obtained. Towards this end, Vegard's model has been found to be the most appropriate to simulate the characteristics of these materials. In addition, it has been established that both alloys are direct semiconductors with the minima located at the Γ point (k = [000]) of the BZ.

As regards a and c lattice constants versus concentration the relations taken from Liou et al. [27] are

$$\alpha(x) = x.\alpha_{AlN/InN} + (1-x).a_{GaN} - \delta_{\alpha}.x.(1-x) \quad (2.1)$$

$$c(x) = x.c_{AlN/InN} + (1-x).c_{GaN} - \delta_{c}.x.(1-x) \quad (2.2)$$

where δ_α and δ_c are the deviation parameters for the α and c constants. Similarly, energy gap (E_g) of the two alloys is described by Vegard's law equation with a curvature term, since they have a parabolic compositional dependence for their bandgap. The parabolic factor is named as bowing parameter b, showing that the energy band gap has a strong dependence on the alloy composition. The values of this parameter obtained by other groups are $b_{AlGaN} = 0.71$ eV [30; 31] and $b_{InGaN} = 1.7$ eV [30], respectively. Vegard's law empirical relation for the band gap is given by

$$E_{g,AlGaN/InGaN}(x) = x.E_{g,AlN/InN} + (1-x).E_{g,GaN} - b.x.(1-x) \quad (2.3)$$

Figure 2.5 is taken from the work of Meyer et al. [31] for $Al_xGa_{1-x}N$ films grown on GaN via MOCVD at different concentrations. As presented, PL experiments showed that the higher the Al-content, the higher the bandgap emission of the $Al_xGa_{1-x}N$ material as expected from theory. The energy band gap reaches AlN's value at very high Al concentration. Apart from energy shift, there is a linewidth broadening of the luminescence peak relative to the Al concentration, due to the alloy disorder seen by the excitons.

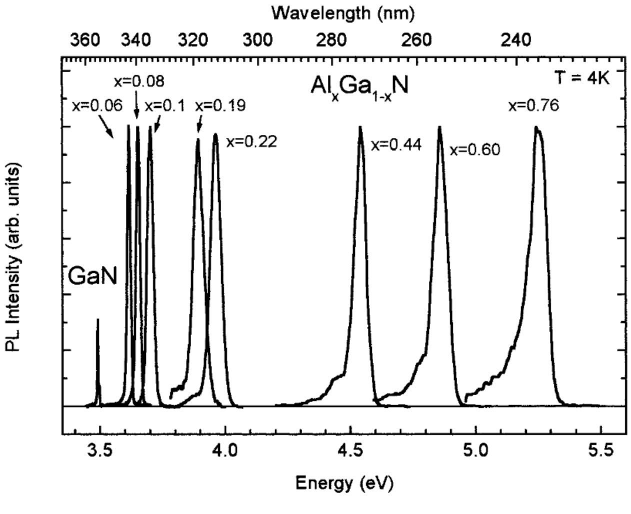

Figure 2.5 Photoluminescence spectra of series of AlGaN on GaN epitaxial films showing the increment of the bandgap energy and the linewidth broadening relative to the Al content [31].

2.2. Piezoelectric and spontaneous polarization

When an electric field is applied in some materials, they exhibit mechanical deformation. If now these materials are subjected to mechanical stress, electric charges appear on their surface. These materials are called piezoelectric materials and the effect is known as piezoelectricity [32]. Furthermore, depending on the arrangement of the anion and cation sublattices in wurtzite structure, another effect arises named as spontaneous polarization [32]. This polarization exists inside the material in the absence of any external stress.

Summarizing the above, the total polarization field within the structure can be described by the Equation 2.4, where ρ_{polar} is the polarization charge density. As one may notice from this equation, there will be a polarization sheet charge density at an abrupt hetero-junction interface arising from the difference in spontaneous polarizations $\Delta P_{spont,z}$ (C/m^2) and from the discontinuity in $P_{piezo,z}$ (C/m^2) coming from the abrupt change due to strain ε_{ij} between the two materials.

$$\nabla . P_{total} = \nabla . (P_{piezo,z} + P_{spont,z}) = -\rho_{polar} \quad (2.4)$$

In III-V nitride hetero-structures, such as quantum wells, it has been found that piezoelectric and spontaneous polarizations account for the carrier concentrations at the interfaces of the alternating materials [33]. Temperature expansion should also be accounted for in piezoelectric polarization for a more detailed calculation. Piezoelectric polarization is caused from strain effects at the interfaces of the materials due to the different values in lattice constants. On the other hand, spontaneous polarization is due to the lack of inversion symmetry in nitrides along the [0001] direction [12]. Figure 2.6 depicts GaN, AlGaN and InGaN materials when grown pseudomorphically on a GaN layer. In the case of AlGaN grown on a Ga-faced GaN, it feels tensile strain, while for InGaN grown on GaN compressive strain is developed.

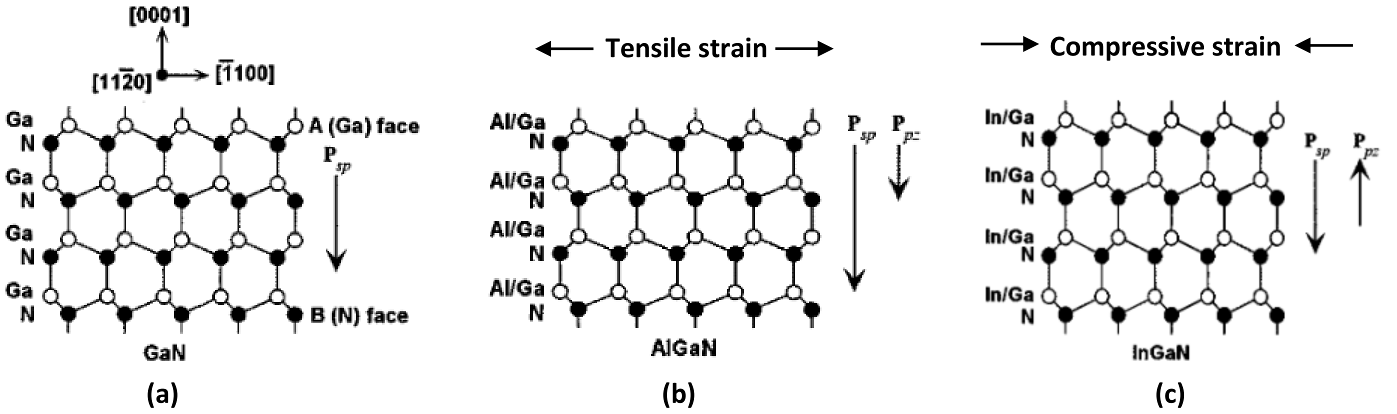

(a) (b) (c)

Figure 2.6 Crystal structure, spontaneous polarization fields (P_{sp}) and piezoelectric polarization fields (P_{pz}) for (a) GaN, (b) $Al_xGa_{1-x}N$ and (c) $In_xGa_{1-x}N$ coherently strained to GaN [0001] [34].

For strained III-V nitride epitaxial layers grown in [0001] direction, piezoelectric polarization is calculated as follows

$$P_{piezo,z} = 2.(\frac{a_{GaN}-a_{Al/InGaN}}{a_{Al/InGaN}}).(e_{31} - e_{33}.\frac{C_{13}}{C_{33}}) \quad (2.5)$$

where e_{ij} are the piezoelectric constants, C_{ij} the elastic coefficients and α the lattice parameters of the materials [34]. The spontaneous polarization of the alloy is calculated by

$$P_{spont,z} = xP_{spont,AlN/InN} + (1-x)P_{spont,GaN} \quad (2.6)$$

where P_{spont} is the spontaneous polarization of the unstrained material and x is the concentration of Al or In, respectively. The total spontaneous polarization is the difference $\Delta P_{spont,z}$ at each interface.

From previous reports [12; 34; 35], it has been found that spontaneous polarization of GaN, AlN and InN is in the $[000\bar{1}]$ direction, while piezoelectric polarization can be in the $[000\bar{1}]$ direction for tensile strain or in the $[0001]$ direction for compressive strain, respectively. The calculated total polarizations for AlGaN/GaN and InGaN/GaN interfaces are - 0.096x and 0.18x, where x is the AlN mole fraction, based on reference [32], by considering the parameters presented in Table 2.2.

Table 2.2 Spontaneous polarization, piezoelectric constants and elastic coefficients of WZ materials [12]

	$P_{spont,z}$ (C/m^2)	e_{33} (C/m^2)	e_{31} (C/m^2)	C_{13} (GPa)	C_{33} (GPa)
GaN	-0.029	0.73	-0.49	106	398
AlN	-0.081	1.46	-0.60	108	373
InN	-0.032	0.97	-0.57	92	224

The built-in electric fields, which are intimately dependent on piezoelectric and spontaneous polarizations, cause the quantum-confined Stark effect (QCSE) and alter the rectangular shape of the quantum wells to a triangular one. This in turn decreases the spatial overlap of the electron-hole wavefunctions due to the band bending and, as a result, there is a lower radiative recombination rate and an additional modification of the energy states [36]. The electric field in MQWs [37], caused by the polarization sheet charges at the hetero-interfaces of a superlattice structure, is expressed as

$$F_{qw} = -\frac{\Delta P}{\varepsilon_o \varepsilon_r}\frac{L_{barrier}}{L_{barrier}+L_{well}} \quad (2.7), \quad \text{where } \Delta P = \Delta P_{piezo,z} + \Delta P_{spont,z}$$

where ε_o is the vacuum permittivity and $\varepsilon_r = 1 + \chi_e$ (χ_e - electric susceptibility) is the relative permittivity of the material. As explained in references [34; 38; 39], a small fraction of Al concentration can generate very strong internal fields. In the case of GaN/AlGaN interface for a 7 % Al-content, this field is several hundreds kV/cm. As can be understood from the above, nitride-based materials are known to exhibit strong piezoelectric effects compared to other traditional III-V semiconductors.

An approach to control the piezoelectric strain arising from lattice mismatch is to use low concentration alloys. By varying slightly the concentration x, the desired lattice constant and bandgap can be succeeded [40]. For this reason, Aluminum concentration was kept low (x = 0.07) in our theoretical design with a quantum well and a barrier thicknesses of 2.7 nm to succeed higher binding energies (E_B) and oscillation strengths (f_{exc}) for the excitons [41].

3. Excitons in semiconductors

3.1. Quantum and semi-classical model of 3D excitons

The first experimental observation of excitonic states was in organic molecules, almost one century ago, which were later explained theoretically by Frenkel in 1931. Excitons can exist also in inorganic semiconductors, named as Wannier-Mott excitons, but due to the low binding energy they are difficult to observe at room temperature. An exciton is formed when a valence-band electron is excited by the absorption of an incident photon and leaves a positively–charged hole in the valence band. This hole then interacts through Coulomb forces with the previous electron and creates a bound state at energy just below the energy gap.

In essence, what really happens is that when an excited electron does not have sufficient energy to reach the conduction band, it tries to recombine with a hole of the same momentum in the valence band but the large number of electrons, which are surrounding the hole, repel the excited electron with electrostatic Coulomb forces. On the other side, the attraction felt by the localized hole overrules this repulsion and results to formation of a quasi-state inside the bandgap. The resulting bound state is electrically neutral and can transport energy without transporting net electric charge. By supplying sufficient energy, named as binding energy, the exciton can split to a conduction band electron and a valence band hole.

If the electron recombines with the hole, caused by their close proximity, we have then the decay of the exciton with a characteristic lifetime τ. However, the decay time τ alters with temperature T and is related with the radiative (τ_r) and non-radiative recombination (τ_{nr}) times by the following formula $\frac{1}{\tau} = \frac{1}{\tau_r} + \frac{1}{\tau_{nr}}$ [42].

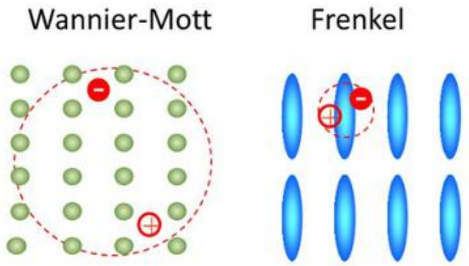

Figure 3.1 Schematic of Wannier-Mott and Frenkel exciton depicting the variation of the radius [43].

Excitons are categorized in two cases according to the properties of the material. They are named as Frenkel (1931) and Wannier-Mott (1937-1938) excitons (shown in Fig. 3.1). Frenkel excitons, are small in size, and are found in organic materials since they have small dielectric constants and thus the Coulomb interaction is strong [44; 45]. Typical values of the binding energy are 100 - 300 meV. On the other hand, Wannier-Mott excitons are found usually in inorganic semiconductors, which have relatively large dielectric constants. Thus, Coulomb interactions are reduced by the screening of the electric field and the average radius is larger than the lattice spacing [46; 47]. As a result, binding energy values are between a few meV up to tens of meV.

Due to the existence of excitons, excitonic peaks are observed in the optical spectra below the characteristic band gap energy. For bulk materials, these peaks can be very clearly seen at low temperatures, since thermal effects ionize carriers from exciton levels. Furthermore, by having a strong overlap between the wavefunctions of the bound electrons and holes in the exciton state compared to when the wavefunctions are delocalized, the matrix element of optical transitions involving excitons is much greater than that from interband transitions. By solving Schrödinger equation for the relative motion of the electron-hole pair, which is analogous to the motion of an electron in the atom, and by taking into consideration the Coulomb interactions, one yields the wavefunctions and binding energies of the exciton states. In this thesis, we used only inorganic materials, thus we focus on Wannier-Mott excitons, whose mathematical model is well explained in reference [1].

Quantum-mechanically, excitons can be described as free particles with a parabolic dispersion within the effective mass approximation model neglecting thus the periodic crystal potential [1]. The effective masses in this case are directly dependent on the crystal parameters, which are usually less than the free-electron mass in vacuum m_e. Another assumption used here is that the electron-hole pair behaves similar to the hydrogen atom. Therefore, a Schrödinger equation can easily be written for this electron-hole relative motion with a wavefunction Ψ(r) as

$$-\frac{\hbar^2}{2\mu}\nabla^2\Psi(r)-\frac{e^2}{4\pi\varepsilon_r\varepsilon_o r}\Psi(r)=E_{B,n}\Psi(r) \quad (3.1)$$

where $\mu=\frac{m_e^* m_h^*}{m_e^*+m_h^*}$ the reduced mass, ε_r and ε_o are the relative and vacuum permittivities and $r=|r_e-r_h|$ the distance between electron and hole. The solution of the above equation gives the expression for the binding energy E_B for each level n as follows

$$E_{B,n}=-\frac{\mu e^4}{2(4\pi\varepsilon_r\varepsilon_o)^2\hbar^2}\frac{1}{n^2}=-\frac{1}{(\varepsilon_r)^2}\frac{\mu}{m_e}\frac{R_y}{n^2}=-\frac{R_y^*}{n^2}\ ,\ n=1,2,\dots,\infty \quad (3.2)$$

where m_e is the rest mass of the electron, R_y = 13,6 eV is the Rydberg energy and R_y^* is the effective Rydberg energy. The total dispersion energy of an exciton is defined as

$$E_{exc,n}=E_g+\frac{\hbar^2K^2}{2M}+E_{B,n} \quad (3.3)$$

where E_g is the energy gap, $K = k_e + k_h$ the wavevector and $M=m_e^*+m_h^*$ the translational mass of the exciton. The effective Bohr radius of the exciton is expressed as

$$a_B^*=\varepsilon_r\frac{m_e}{\mu}a_B \quad (3.4)$$

where α_B = 0.53 Å is the Bohr radius. Typical values for bulk wurtzite GaN material at cryogenic temperatures are E_{gap} = 3.51 eV, $E_{B,1}$ = 26 meV and $\alpha_{B,1}$ = 30 Å. Room temperature energy is k_BT ~ 25 meV in comparison with the exciton binding energy. Schematics of the optical transitions of the ground and excited exciton states that are inside the bandgap of a typical semiconductor with the corresponding absorption spectra are presented in Figure 3.2.

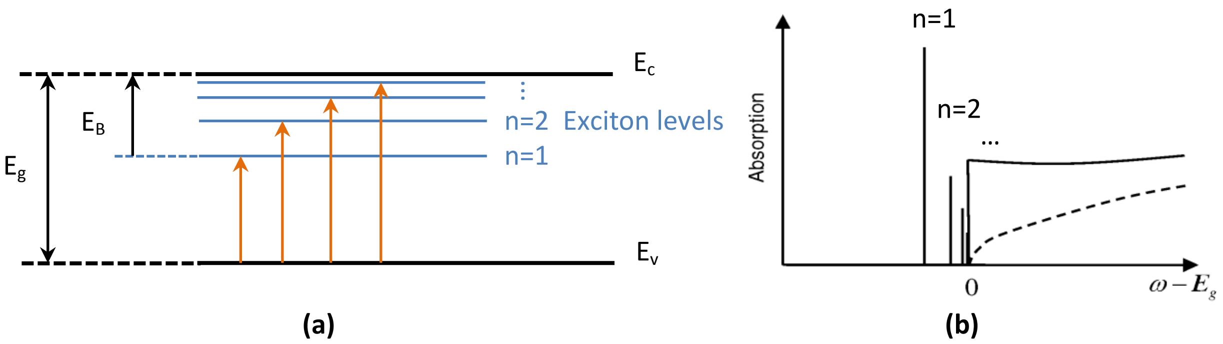

Figure 3.2 (a) Illustration of exciton energy levels and (b) absorption spectra vs energy (solid line low T and broken line high T) [48].

Semi-classically, the exciton is described as a mechanical system of two masses bound together by a spring known as Lorentzian oscillating dipole and light is governed by Maxwell's equations. The equation describing the electron's movement $x(t)$ under the influence of an applied electric field is expressed as

$$m_o\ddot{x}(t) + 2\gamma m_o\dot{x}(t) + \omega_o^2 m_o x(t) = -eE(t) \quad (3.5)$$

m_o is the electron mass, γ is the damping factor due to energy radiation, ω_o is the natural frequency of the oscillator, - e is the electron charge and $E(t) = E_o\cos\omega t$ the electric field. If we consider a three dimensional array of oscillators with N density (number of oscillators per unit volume) for the bulk case, the polarization arising from external electromagnetic radiation is described as

$$P = N\alpha E = \frac{Ne^2}{m}(\omega_o^2 - \omega^2 - i\omega\gamma)^{-1}E \quad (3.6)$$

The dielectric displacement yields

$$D = \varepsilon_o E + P = \varepsilon_o[1 + \frac{Ne^2}{m}(\omega_o^2 - \omega^2 - i\omega\gamma)^{-1}]E \quad (3.7)$$

and the dielectric ε(ω) function is described by

$$\varepsilon(\omega) = 1 + \frac{Ne^2}{m}(\omega_o^2 - \omega^2 - i\omega\gamma)^{-1} \quad (3.8)$$

In this classical model, the term Ne^2/m gives the coupling strength (f_{exc}) of the electromagnetic field to the oscillators. As will be explained within the quantum model for the confined excitons, this coupling is given by the square of the transition matrix element. The second correction is that one should account for the field created from all the dipoles. This results in a shift of the transition frequency.

As a consequence of the previous equation, refractive index is modulated describing the exciton transition in a dielectric material ($\mu(\omega) = 1$) as,

$$\tilde{n}(\omega) = n(\omega) + ik(\omega) = \sqrt{\varepsilon(\omega)} \quad (3.9)$$

where $k(\omega)$ is the imaginary part and accounts for the absorption inside the medium. When modelling microcavities based on transfer matrix method (TMM), it is essential to use this modulated refractive index.

3.2. Confined excitons in quantum wells

Semiconductor structures such as quantum wells (QWs), quantum wires (QWs), quantum dots (QDs), superlattices (SLs) or other novel micro/nano structures significantly modify the properties of excitons due to quantum confinement. When a thin layer is sandwiched between two higher band gap layers, the emission from exciton states in the single quantum well are shifted towards higher energies [49]. As the dimensions of the a crystal become smaller or comparable to the Bohr radius, exciton entity is described by quantum states as a particle inside a box and therefore the overlap of the wavefunctions of the electrons and holes is increased. This leads to higher binding energies (E_B) and oscillation strengths (f_{exc}) for the electron-hole pair. More specifically, transition energies in QWs vary in a non-trivial manner based on the excitation intensity [50], doping profile [51; 52; 53], QCSE due to built-in strain [50; 54] and lastly, on the well (Fig. 3.3) and barrier widths [52; 55]. Therefore, dimensionality is a crucial but not the only parameter that someone has to account for calculating the emission energy.

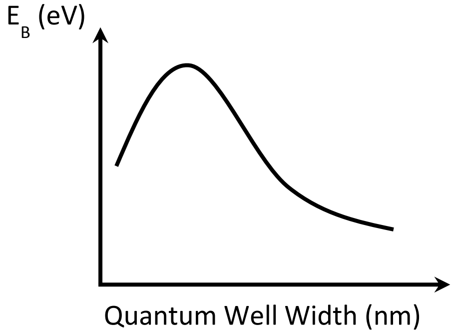

Figure 3.3 Illustration showing the peak of the exciton binding energy versus the width of the QW.

By modelling the exciton as a particle in a box with electron and hole seen as hydrogen nucleus, we can replace nucleus with the hole having positive charge and negative electron mass. We consider again the effective mass approximation model and the solution for this system is similar to a particle inside a box with the mass being replaced by the reduced mass. As a result, this quantization of both electrons and holes alters the energy spectrum of the confined system.

As presented in Figure 3.4, the low-bandgap layer creates quantum wells for both electrons and holes and leads to a high-energy shift in the energy spectrum due to the forbidden states below the ground state of the well $E_{g,qw} = E_{e1} - E_{h1} > E_g$. Starting from the same theory as before, Schrödinger equation for an exciton inside a QW is similar to the previous one. However, at lengths $|L| > L_{qw}$, the confining potential in z direction must be taken into account, which is the energy difference between the two bandgaps of the materials used. Thus, Schrödinger equation results to

$$\left(-\frac{\hbar^2}{2\mu}\nabla^2\Psi(r) - \frac{e^2}{4\pi\varepsilon_r\varepsilon_o r}\Psi(r) + V_e(z_e) + V_h(z_h)\right)\Psi(r) = E\Psi(r) \quad (3.10)$$

where V_e and V_h are the confining potentials for the electron and hole on the z-axis. The solution for the exciton binding energy inside the QW is

$$E_B^{2D} = -\frac{R_y^*}{\left(n-\frac{1}{2}\right)^2} \text{ , } n = 1, 2, \ldots, \infty \quad (3.11)$$

and is theoretically 4 times higher than the value for the bulk case ($E_B^{2D} \approx 4E_B^{3D}$). For real QWs, a trial wavefunction, with a variational parameter α, is used in order to express the binding energy as function of the QW width [1]. By maximizing the $E_B^{2D}(a)$, it yields the value of the binding energy inside the QW. Many algorithms have been used following this route in order to estimate the real values for the E_B^{2D}. The schematics below represent the energy states in a quantum well (QW) without and with the built-in electric field caused by QCSE and by taking periodic boundary conditions.

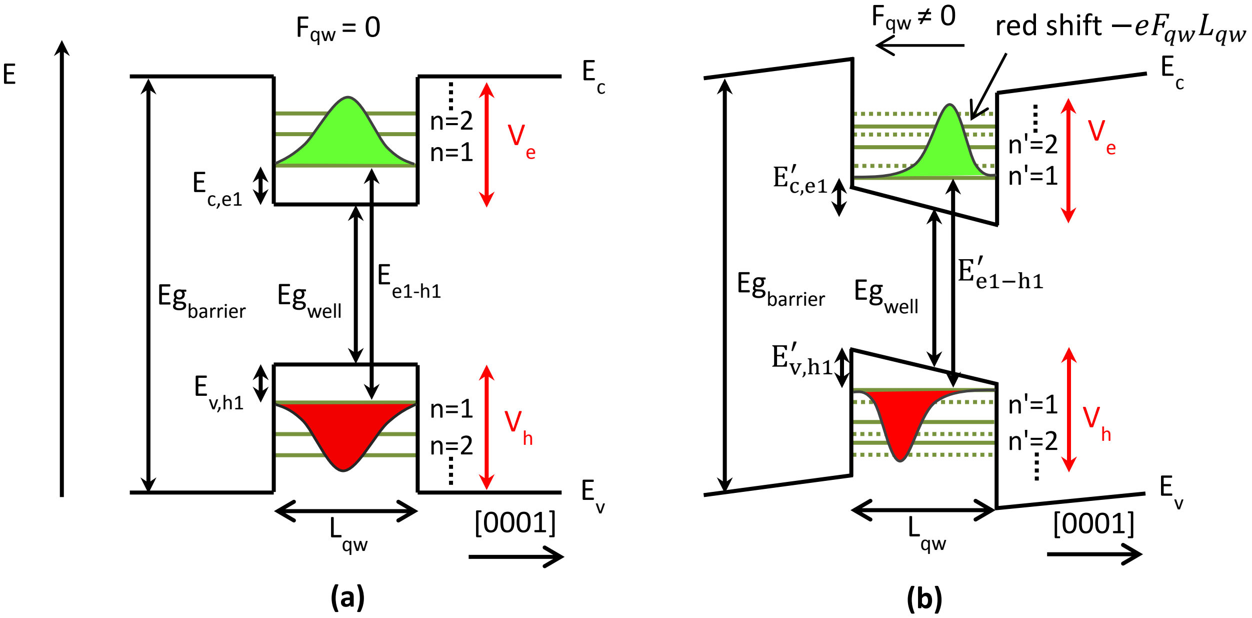

Figure 3.4 Energy levels of electrons and holes in a QW (a) without and (b) with built-in electric field F_{qw}.

By adding the built-in field component in the Hamiltonian of the system, the total exciton transition energy in a QW is expressed as

$$E_{exc,n'} = E_{en'-hn'}(F_{qw}) + E_B^{2D}(F_{qw}) - eF_{qw}L_{qw} + \frac{\hbar^2 K_{//}^2}{2M} \quad (3.12)$$

where $E_{en'\text{-}hn'}(F_{qw}) = E_g + E_{c,en'}(F_{qw}) - E_{v,hn'}(F_{qw})$ is the transition in the QW for each n, E_B^{2D} is the binding energy of the 2D excitons, F_{qw} is the field inside the QW, L_{qw} the width of the QW and $K_{//}$ is the in plane wavevector. The term $-eF_{qw}L_{qw}$ in equation 3.12 represents the redshift of the gap induced by the built-in field for each n. Note that in the case where the width of the QW is larger than the Bohr radius of excitons, E_B can be neglected.

Depending on the QW width, the thermal broadening of the exciton peak is not so strong as opposed to the bulk case. In QWs, lineshape broadening is a convolution of homogeneous and inhomogeneous terms, the former coming from short lifetime and the latter from variation in thickness of the well. The lineshape distribution of a homogeneous broadening is Lorentzian, while in the case of inhomogeneous broadening is a Gaussian. Therefore, homogeneous and inhomogeneous broadening resulting in a decay rate γ_x of excitons is added to the energy relation as $-i\gamma_{x,K_{//}}$.

It should be pointed here that in QW structures the density of states (DOS) is modified from that in a bulk material, meaning that the DOS does not have the same energy dependence as in the 3D case. Within parabolic approximation for the energy bands, the DOS for a 2D structure becomes

$$\rho_{2D} = \sum_{n_z} \frac{M}{\pi\hbar^2} H(E - E_{n_z}) \quad (3.13)$$

where H[E] is the Heavyside function. When the structure consists of N similar QWs close to each other, we have to multiply the density of states with the number of the QWs. A change in DOS entails that there will be a change in the optical transition rate $W_{f\rightarrow i}$ governed by the Fermi's Golden Rule for first order transitions as

$$W_{f\rightarrow i} = \frac{2\pi}{\hbar}\sum_{f,i}\left|\langle f|\widehat{H'}|i\rangle\right|^2 \rho_{2D} \quad (3.14)$$

where i, f initial and final states with energies E_i and E_f, respectively, and H' = - e**r**.**E** is the interaction Hamiltonian. Light-exciton interaction is defined by the transition matrix element $\mathrm{M}_{fi} = |\langle f|\widehat{H'}|i\rangle|$ which describes the overlapping between electron Ψ_e(r) and hole Ψ_h(r) wavefunctions. The square of this matrix element ($|\langle f|\widehat{H'}|i\rangle|^2$) is known as the transition probability. The transition rate $W_{f\rightarrow i}$ is proportional to the transition probability multiplied by the square of the amplitude of the perturbation H' ~ $|E_o|^2$ ~ I where I is the intensity (energy flux per area and time).

In QWs, this overlapping is much higher than in bulk semiconductors. A major parameter in these transitions is the oscillator strength, which tells us how strong is the optical transition and is defined as

$$f_{exc} = \frac{2N\omega_{fi}}{\varepsilon_o\hbar}|\langle f|\widehat{H'}|i\rangle|^2 \quad (3.15)$$

where N is the number of oscillators per unit volume, ω_{fi} is the transition frequency and ε_o the vacuum permittivity. Following the quantum theory, one can show that the oscillator strength for 2D excitons can be, theoretically, up to 8 times higher than for 3D ($f_{exc}^{2D} \approx 8\, f_{exc}^{3D}$), since the Bohr radius α_B is reduced due to confinement. Usually, more confinement increases the overlapping of the wavefunctions and leads to higher oscillation strengths for the exciton entities.

4. Quantum microcavity structures

4.1. Cavity photons in weak and strong coupling regime

Microcavity (MC) is defined a structure that confines photons in order to control photonic interactions in the semiconductor structure. MCs are usually formed by reflecting metallic mirrors or Distributed Bragg reflectors (DBRs) on the two sides of an active medium and follow the same principles of a Fabry-Perot cavity with an optical length of L_c. A DBR is an alternating layered structure of dielectric materials of high and low refractive indices n_H and n_L. For a large number of those alternating pairs, DBR forms a frequency region, named as stop-band, in which reflectivity is close to unity. In planar microcavities, photon quantization occurs in the growth z-direction but the planar (x,y-direction) states are not affected by any confinement.

The name microcavity implies that the optically active material is only a few micrometers thick but sometimes it can be even in the submicron scale [2]. Unlike long the long optical cavities, typically used in standard edge emitting diodes, inside microcavities the quantum effects of the light's electromagnetic field are easily noticeable. Therefore, we can attribute the name quantum microcavity structures (QMCs) and we can use them for the investigation of exciton-polariton phenomena in semiconductors. Moreover, the major difference between the long cavities and microcavities is the cavity length L_c.

The confined optical wave inside the planar microcavity is represented by the following equation

$$\frac{d^2 F_k(z)}{d^2 z} + \left(\frac{\omega^2}{c^2}\varepsilon(z) - k_{//}^2\right) F_k(z) = 0 \quad (4.1)$$

where $F_k(z)$ are the one dimensional modes of the optical wave, the wavevector equals to $k = k_{//} + K_z$ and $\varepsilon(z)$ is the dielectric constant chosen to be z-dependent due to confinement [56]. The solutions of this wave equation are the standing waves inside the structure as simplified in Figure 4.1.

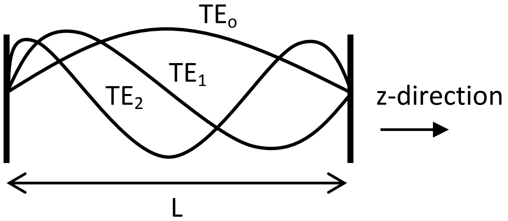

Figure 4.1 Illustration showing the standing waves (TE$_o$, TE$_1$ and TE$_2$) inside a planar microcavity.

Regarding microcavities, the thickness of the cavity material is of the order of the wavelength divided by the refractive index. This attributes to the low number of eigenmodes and the large frequency separation between successive cavity modes (FSR) in microcavities that, in most cases, stop-bands contain only one of these modes. On the contrary, the opposite accounts for the long cavities cavities, where spacing between eigenmodes is small and many of them are present.

Furthermore, the length of the active material in the microcavity must be an integer number times half the wavelength in the cavity as

$$L_c = m\frac{\lambda_c}{2} = m\frac{\lambda_{air}}{2n_c} \quad (4.2)$$

where m ∈ ℕ. Depending on the thickness of the optical spacer, we have a characteristic "cavity-mode" inside the resonator. This is visible as a profound dip at wavelength λ_{air} in the center of the high reflectivity stop-band region in a reflectivity spectrum. Each layer of the multiple repeated pairs (N) in a DBRs mirror has a thickness of $L_{n_i} = \frac{\lambda_i}{4}$ (where $\lambda_i = \frac{\lambda_{air}}{n_i}$).

As the number of pairs increases, there is an exponential influence to the mirror reflectivity. An explanation for this is that all Fresnel reflections add in phase and reflectivity of the mirror increases as a function of mirror thickness (or number of pairs N). For various lengths of the cavity L_c between the two DBRs, the cavity gives one or more antinodes of electric field inside the active region. An example of the λ-sized microcavity (m = 2), where one antinode of the field can exist inside it, is shown in Figure 4.2.

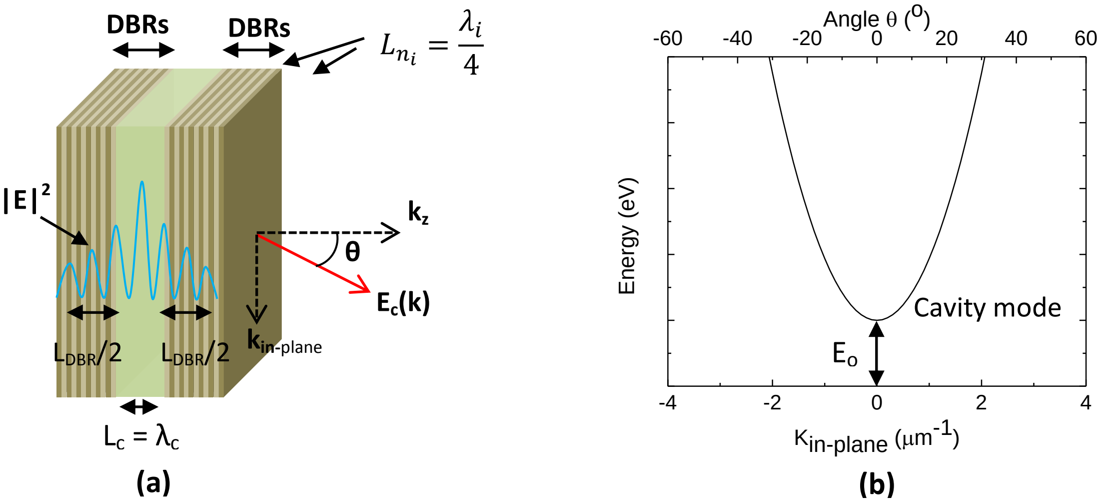

Figure 4.2 (a) Schematic of planar microcavity for m = 2 and (b) energy dispersion versus $k_{//}$ and angle.

A characteristic parameter describing the quality of a microcavity is named Quality Factor (Q) (see Appendix A). Q has a direct relation with the photon lifetime τ_{ph} and gives information on how much time a cavity photon stays in the microcavity before it decays. The definition of Q is

$$Q = \frac{\lambda_o}{\delta\lambda} \quad (4.3)$$

where λ_o is again the resonant wavelength and δλ is the full width at half maximum (FWHM) of the resonant peak. As explained in references [57; 58], DBRs are penetrated by the cavity field and thus the Fabry-Perot cavity length has to be replaced by

$$L_{eff} = L_c + L_{DBR},\ where \quad L_{DBR} = \frac{\lambda_c}{2n_c}\frac{n_L n_H}{|n_H - n_L|},\ n_L < n_H \quad (4.4)$$

By taking into account that the growth direction is parallel to z-axis, the relation for the k_z wavevector in the medium is $k_{zn} = \frac{2\pi}{\lambda_n} = \frac{m\pi}{L_{eff}}$ and the energy of the cavity mode by using Taylor expansion becomes

$$E_{cav,n_z} = \frac{\hbar c}{n_{eff}} k = \frac{\hbar c}{n_{eff}} \left[\left(\frac{m\pi}{L_{eff}} \right)^2 + k_{//}^2 \right]^{1/2} \cong \frac{\hbar c}{n_{eff}} \frac{m\pi}{L_{eff}} + \frac{\hbar c}{2n_{eff}} \frac{k_{//}^2}{(m\pi/L_{eff})} = E_o + \frac{\hbar^2 k_{//}^2}{2m_{ph}} \quad (4.5)$$

where m is the quantum number, n_{eff} is named as effective refractive index and is obtained by the weighted average of the group refractive index of the cavity and the contribution of the DBR layers that are penetrated by the EM field of the cavity mode and, lastly $m_{ph} = \frac{\hbar\pi m n_{eff}}{c L_{eff}} \approx 10^{-5} m_e \ or \ 10^{-4} m_{exc}$ is the effective photon mass, which is responsible for the curvature cavity dispersion. The decay rate γ_c of the photons is added to the energy relation as $- i\gamma_{c,k_{//}}$. For small values of $k_{//}$, the dispersion can be approximated by a parabola as shown in Figure 4.2 (b). There is a direct relation that connects $k_{//}$ with the angle of incidence and energy dispersion as shown below

$$k_{//} = \frac{E_c(k)}{\hbar c} \sin(\theta) \quad (4.6)$$

Consider now the case where an exciton in a quantum well decays to a lower state by the emission of a photon equal to the energy difference of the two states. This spontaneous emission can be affected by the surrounding media and alter the transition matrix element M_{fi} that was described in the previous paragraph. By placing this quantum well inside a cavity, there is an amplification of the spontaneous emission from the excitonic states when being in resonance with the cavity mode, known as Purcell effect.

The light emission can be done in two different ways, named as weak (WC) and strong (SC) coupling regimes. In the WC regime, the emitted photon has a low probability to be reabsorbed and the whole process can be described by perturbation theory, while the emission follows Fermi's Golden Rule. This regime is used in vertical-cavity surface emitting lasers (VCSELs). In the SC regime, the emitted photon has a high probability to be reabsorbed and re-emitted by the exciton and hence Fermi's Golden Rule is no longer valid. A polariton formalism must be used in this case since absorption and emission oscillation is so fast that the photon stimulates several times the exciton before it escapes from the cavity. These oscillations are called Rabi oscillations with a frequency (Ω_R) equal to the energy splitting at the anti-crossing k point divided by $\hbar$.

Strong coupling is rather demanding to occur, since it requires a high reabsorption probability meaning that Rabi frequency must be higher that the decay rate of the system. Hence, it is vital to have a well-designed microcavity such that optical transition must be coupled in resonance with the cavity mode of the microcavity. For this reason, well defined states are needed with low FWHM even at room temperature. In many cases, several QWs are used inside the active region of the microcavity by taking advantage of the sharpness of excitonic states. Excitons in QWs are characterized by a continuum of in-plane wavevector states and are also quantized in the growth direction by the alternating high and low energy gap materials. Apart from that, excitons in QWs have enhanced intensity due to the low radiative recombination times in comparison to the ones for the bulk case.

Investigation of exciton-photon strong coupling can be accomplished by obtaining as narrow cavity and exciton linewidths as possible. These two factors are mainly controlled by the growth parameters and the quality of crystal structure. Quantum well width, as well as alloy fluctuations, increase exciton linewidth, while photon scattering inside the cavity, absorption losses and escape through the DBR can increase the cavity linewidth. Up to now, MOCVD or MBE are the most well-known techniques for growing such high-quality structures. By adjusting all the above parameters, one can fabricate a successful microcavity operating at the strong coupling regime.

4.2. Exciton–photon strong coupling

Starting by basic terminology, cavity polaritons denote the exciton-photon eigenstates in microcavities (MCs), by analogy to exciton-photon modes in bulk materials [59; 60]. When this occurs, there is a strong coupling between excitons and photons inside the MCs. In planar microcavities, there is a continuum of cavity modes labeled by their in-plane wavevector $k_{//}$ similar to the excitonic states. The difference in dispersions between these two modes is illustrated in Figure 4.3. When adding a QW in the microcavity, formation of excitons occurs with an abrupt change in dielectric function. By varying the incident angle (θ) in order to tune the cavity mode frequency to the exciton transition frequency, a characteristic dispersion occurs, where the two modes anticross [61]. If carefully observed, at this anticrossing there are two distinct peaks in the optical spectra instead of one. The nature of this phenomenon comes from the quantum coupling between excitons and photons by the creation of new quasi-particles, named as polaritons. Polaritons can be manipulated as coherent superpositions of light and matter which exhibit new properties.

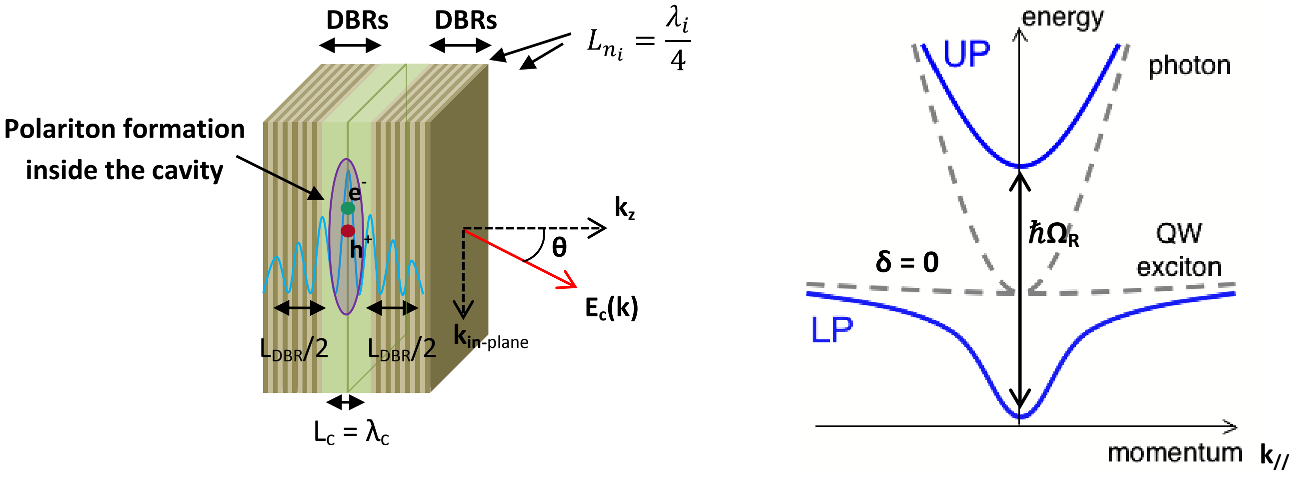

(a) **(b)**

Figure 4.3 (a) Illustration representing a microcavity with an embedded quantum well (QW) working in the strong coupling regime and (b) Dispersion relation of exciton-polaritons depicting Rabi frequency (Ω_R) due to splitting and the upper (UP) and lower (LP) polariton branches [62].

In the case where quantum wells are outside a microcavity, excitons are decaying into one of the continuum photon states within a finite lifetime [63]. On the other hand, since photon states are quantized inside microcavities, only one can couple to an in-plane exciton state of the same momentum. If this occurs, there is no irreversible decay of excitons and the new quasi-states, the cavity polaritons arise. These excitations oscillate on a sub-picosecond timescale before the photon finally escapes from the cavity. The period of this oscillation can be found from the Rabi frequency (Ω_R) by $T = 1/\Omega_R$. The framework of microcavity devices for obtaining the analytical expressions for the exciton-polariton mode energies can be treated in both semi-classical and full quantum theory, which has been proved to be equivalent based on the work of Savona et al. [64].

For simplicity, the semi-classical model is more often used in combination with the transfer matrix method for simulating polariton branches with very good approximations to the real structures [65]. On the other hand, quantum mechanical description is more appropriate with the linear Hamiltonian of the two coupled oscillators within rotating-wave approximation, which is defined as

$$H = H_{cav} + H_{exc} + H_{int} = \sum_{k_{//}} E'_{cav,k_{//}} a^{\dagger}_{k_{//}} a_{k_{//}} + \sum_{k_{//}} E'_{exc,k_{//}} b^{\dagger}_{k_{//}} b_{k_{//}} + \sum_{k_{//}} V(a^{\dagger}_{k_{//}} b_{k_{//}} + a_{k_{//}} b^{\dagger}_{k_{//}}) \quad (4.7)$$

where H_{cav} and H_{exc} describe the photon and exciton Hamiltonians and H_{int} is the interaction term, $a^{\dagger}_{k_{//}}$, $b^{\dagger}_{k_{//}}$ and $a_{k_{//}}$, $b_{k_{//}}$ are the creation and annihilation operators for cavity photons and excitons.

The linewidths of cavity ($\gamma_{c,k_{//}}$) and exciton ($\gamma_{x,k_{//}}$) modes acting as damping parameters are included in the energies $E'_{cav,k_{//}}$ and $E'_{exc,k_{//}}$ of the uncoupled cavity and exciton mode energy, respectively. The linewidth of exciton γ_x arises from homogeneous and inhomogeneous broadening in the case of excitons (due to disorder) and the linewidth of photon γ_c from the finite values of finesse (mirror losses) for the cavity modes, respectively. Lastly, V is the interaction parameter of the light field with the dipole moment of the electron-hole pair.

In order to find the normal modes, we have to diagonalize the above Hamiltonian by using a transformation of operators, in which new operator p_k is defined as a linear combination of the creation and annihilation operators, as follows

$$p_{k_{//}} = Aa_{k_{//}} + Bb_{k_{//}} \quad (4.8)$$

These new operators describe the mixed states. By forcing p_k to follow the eigenvalue problem $[p_k, H] = E_k p_k$ one yields the dispersion relation for the lower (LP) and the upper polariton (UP) states

$$E_{\substack{UP \\ LP},k_{//}} = \frac{(E_{cav,k_{//}} + E_{exc,k_{//}})}{2} - \frac{i}{2}(\gamma_{c,k_{//}} + \gamma_{x,k_{//}}) \pm \frac{1}{2}\sqrt{4V^2 + \left(E_{cav,k_{//}} - E_{exc,k_{//}} - i(\gamma_{x,k_{//}} - \gamma_{c,k_{//}})\right)^2} \quad (4.9)$$

In the case where there is zero detuning ($E_{exc} = E_{cav}$) at $k_{//} = 0$, if the coupling strength (V) of exciton-photon interaction is much greater than the linewidths of cavity (γ_c) and exciton (γ_x) modes, the square root in the previous relation (Eq. 4.9) becomes purely real, and the cavity is said to be in strong coupling regime [66]. The condition for strong coupling then is defined as

$$V = \hbar \sqrt{\frac{2\pi\, e^2 N_{qw} f_{exc}}{4\pi\, n_{eff}{}^2 m_e L_{eff}}} \gg \left|\frac{\gamma_{c,k_{//}} - \gamma_{x,k_{//}}}{2}\right| \quad (4.10)$$

where e is the electric charge, N_{qw} is the number of the QW, f_{exc} is the oscillator strength, n_{eff} and L_{eff} are the effective refractive index and effective length of the cavity and m_e is the electron mass in vacuum [64; 67]. Rabi splitting (Ω_R) is approximated as

$$\hbar\Omega_R \approx \sqrt{4|V|^2 + \left(\delta - i\left(\gamma_{x,k_{//}} - \gamma_{c,k_{//}}\right)\right)^2} \quad (4.11)$$

where δ is the detuning ($\delta = E_{cav,k_{//}} - E_{exc,k_{//}}$) between cavity and exciton mode. Based on the above relation, f_{exc} can be deduced by measuring Ω_R from a Reflectivity or a Photoluminescence graph at the anticrossing of the cavity mode (E_{cav}) and the QW exciton (E_{exc}) [68]. Reported Rabi splitting Ω_R value for GaN is around 70 meV. Moreover, it can be shown that for $k_{//}$ close to zero, polariton mass (m_{pol}) is approximately 2 times the cavity photon mass.

For planar microcavities, photoluminescence and reflectivity experiments can reveal directly the strong coupling regime since the external photons result from polaritons due to the finite lifetime of the photonic component inside the cavity [69; 70]. Thus, it is not needed for polaritons to reach the surface to result in external photons as it holds for the bulk case. It should be mentioned that between the external photons and the cavity polaritons there is one to one correspondence as an outcome of the quantization in the z-direction. When a sufficient number of polaritons condensates at $k_{//} = 0$, Bose-Einstein condensation (BEC) is said to occur and the device is emitting coherent photons. This regime of the microcavity is called polariton lasing and is manifested at various temperatures depending on the binding energies of the excitons in every system. It is possible to achieve polariton condensation at large temperatures by using materials with high binding energies such as GaN or ZnO [71; 72]. Apart from the previous cases, Lagoudakis et al. [73] have reported an intermediate situation where strong and weak regimes can coexist due to the population of localized states by non-resonant optical excitation.

When the cavity and exciton modes are not in resonance at $k_{//} = 0$ there is a detuning ($\delta \neq 0$). Therefore, we can distinguish two other cases defined as negative ($\delta < 0$) and positive ($\delta > 0$) detuning. As a consequence, this detuning affects the shape of the energy states to more "photon" or "exciton-like", respectively. More specifically, in the case of a negative detuning ($E_{cav} < E_{exc}$), LPB is more photonic while UPB is more excitonic. Exactly the opposite holds for the positively detuned ($E_{cav} > E_{exc}$) structure. It should be pointed out here that when we excite planar microcavities, the oscillators which can be excited with the same eigenfrequency are in the xy plane normal to z-axis or with another eigenfrequency parallel to z only. In the first case, we obtain only twofold degenerate upper and lower polariton branch, but no longitudinal branch for k//z since both oscillators in the xy are transverse. If now the excitation is in the x-axis, there is a nondegerate transverse polariton branch for E//y and a longitudinal branch from the x-oriented oscillators. In this case, the oscillators do not couple and we obtain intersecting dispersion curves.

5. Quantum microdisk structures

5.1. Whispering Gallery Modes

Whispering gallery waves were originally observed by Lord Rayleigh in St Paul's Cathedral circa back in 1878. Lord Rayleigh explained that the sound waves propagating close to the cylindrical wall are specific resonances of a wave field traveling around a concave surface due to internal reflection. This phenomenon is similarly found in optical waves, where the continuous internal reflection from the surface acts as a microresonator. These whispering gallery mode optical resonators have been found to possess very intriguing properties such as high Q-factors [74; 75], tunability [76] and small modal volumes [77].

Theoretical analysis of these optical modes has shown that whispery gallery modes can exist in microspheres, microcylinders or even microdisks [1; 3; 78]. Furthermore, it has been reported that radius and surface roughness play a crucial role to the field distribution and effective volume of the resonator. This chapter introduces the derivation of whispering gallery modes from the wave theory for a 2D cylindrical disk resonator and the effect of the resonator parameters. Figure 5.1 illustrates the simulation of the first order and the second order whispering gallery modes of a 1.2 µm disk.

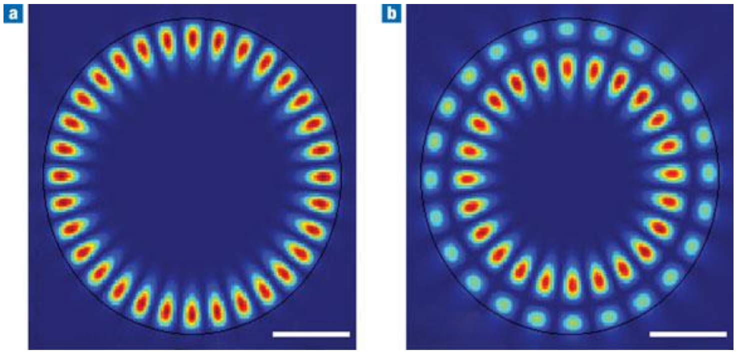

Figure 5.1 FDTD simulation data for a 1.2 µm diameter disk. (a) First-order whispering gallery mode and (b) second-order whispering gallery mode at 428 nm. Red corresponds to the highest field density and blue is the lowest field density. The black circle indicates the edge of the microdisk [3].

Following the same idea as Lord Rayleigh for a 2D cylindrical cavity, we start by considering that inside the cavity the wave speed is u_c, while outside u_o. Hence, the refractive index inside the cavity is

$$n_c = \frac{u_c}{u_o} \quad (5.1)$$

In order to find the eigenmodes of the system, we define $k_i = \frac{\omega}{u_i}$ and try to solve the Helmholtz equation in cylindrical coordinates

$$\nabla^2 \Psi(r,\varphi,z) + k_i^2 \Psi(r,\varphi,z) = 0 \quad (5.2)$$

where i = c for inside ($r \leq \alpha$) and i = o ($r > \alpha$) for outside the cavity, while r, ϕ and z denote the cylindrical coordinate system. Within the cylindrical cavity, WGMs are described by the azimuthal (m) and the radial (n) number of the Bessel functions $J_m(n_c k_o r)$, where n-1 denotes the number of nodes along the radius r [79]. On the other hand, outside the cavity the field is described by the Hankel functions $H^{(1)}{}_m(k_o r)$. For the given geometry, the TE mode is defined by the triplet B_r, B_z and E_ϕ, while the TM mode by E_r, E_z and B_ϕ.

By imposing the appropriate boundary conditions and connect the solutions at the boundary r = a, we obtain a transcendental equation (Eq. 5.3) which combines Bessel and Hankel functions and has to be solved numerically to find the eigenmodes of the cavity [1].

$$\frac{J'_m(n_c k_o a)}{J_m(n_c k_o a)} = \frac{1}{n_c}\frac{H'_m(k_o a)}{H_m(k_o a)} \quad (5.3)$$

The criteria for having resonant modes is

$$2\pi n_c R = m\lambda_c \quad (5.4)$$

where n_c and λ_c are the refractive index and wavelength, R is the radius and m is the mode number of the resonator. For each $m \in \mathbb{Z}$ there are infinite solutions defined by a second integer $n \in \mathbb{N}$ in terms of increasing k_o. First-order whispery gallery modes are called the ones with n = 1 and m >> 1.

Similarly to microcylinders, the same theory can be applied to microdisks. The use of them acting as resonators does not require a DBR deposition since reflection comes from the circular edges and not from the vertical surfaces of the samples [79]. This reduces the crystal growth time necessary in microcavities, where many quarter-wave layers are required. Furthermore, in the disk geometries there is a strong optical confinement leading to gain enhancement up to twenty times more than in vertical cavities. Considering the small modal volume of the disks, several modes can overlap with the QW emission depending on the radius.

An illustration of the side view image of a mushroom-shaped microdisk is shown in Figure 5.2 [3]. The shape and the size of the post layer can be varied depending on the desired geometry. Usually thinner posts tend to exhibit higher quality of WGMs since light is more confined between the air (n = 1) and the disk (n > 1) layer. Moreover, Ruth et al. [80] have reported that by depositing a capping layer on top of the disk, it can enhance the emission from the disk and the WGMs become more prominent in comparison to the spontaneous emission.

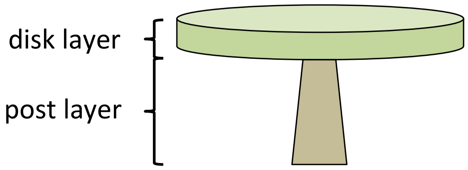

Figure 5.2 Illustration of a mushroom-shaped microdisk optical resonator consisting of a disk and a post layer after being photo-electrochemically etched.

6. Optical Characterization

6.1. Photoluminescence

Optical characterization has been very popular in areas where non-contacting measurements are needed and most of the times fast data acquisition is supported through automated systems. Optical measurements are usually taken by absorbed, emitted, reflected or transmitted light and have high sensitivity. A useful technique that is used for the determination of shallow- and deep-level impurities in semiconductors, without destroying the samples, is Photoluminescence (PL) or Fluorescence. For the specification of deep level impurities, it must be provided that the recombination is radiative.

Photoluminescence plays a major role in characterization of III/V semiconductors that have high internal efficiency, since most of them are direct semiconductors. Internal efficiency gives us information on how many of the optically generated excitons recombine radiatively and thus emitting light. The spectrum region that is of common interest is from ultraviolet up to the far infrared wavelengths. The relationship that connects energy and wavelength is

$$E = \frac{hc}{\lambda} \quad (6.1)$$

As presented in Figure 6.1, the main parts of the PL setup are a laser source (with hv > Eg), a cryostat to cool the sample at temperatures close to liquid Helium and vacuum pumps. It should be noted that the sample must have no strain when placed to the holder since this alters the emitted light. In order to obtain the maximum spectroscopic information possible about the sample’s structure, low temperatures are desired. If not, thermal effects arise that broaden the linewidth of a band in the PL spectrum due to thermal excitation of carriers, giving a width of kT/2. PL measurements at room temperature are mostly used for mapping the trap densities and doping of semiconductors.

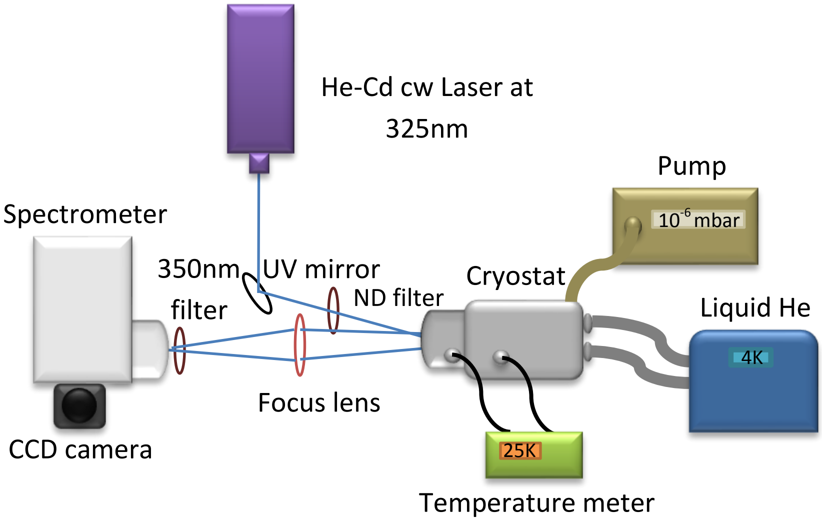

Figure 6.1 Sketch of the Photoluminescence setup where a laser was used as an excitation source at various temperatures and light is focused on the sample and spectrometer by using mirrors and lenses.

At low temperatures (< 10 K), bound exciton recombination occurs, where a free electron (hole) from the conductance (valence) band is combined with a neutral acceptor (donor). For intermediate temperatures 20 - 100 K and pure materials, free exciton recombination dominates, where an excited state of electron and hole bound together resides inside the band gap. If the material is not pure, having shallow or deep states, bound exciton recombination is more powerful. Bound excitons transitions are distinguished from the donor-acceptor recombination, where an electron on a neutral donor can recombine with a hole on a neutral acceptor, by the different FWHM linewidth. At room temperature band-to-band recombination is the main process of emitting light, where electrons from conductance band recombine with valence band electrons with emission of photon of energy equal or greater than the band gap. Figure 6.2 illustrates the most important radiative transitions.

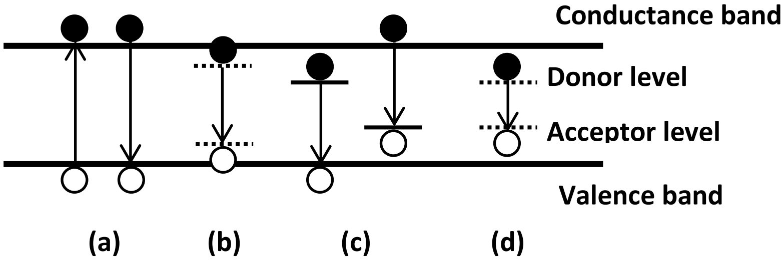

Figure 6.2 Schematic of most important radiative transitions in a semiconductor: (a) band to band, (b) free exciton, (c) bound exciton and (d) donor-acceptor recombination.

After the generation of electron-hole pairs, excitons recombine by one of the radiative or non-radiative mechanisms. If the recombination is radiative, emission of photons takes place. Some of these photons can be reabsorbed by the sample or be focused through a lens into a spectrometer to analyze the emitted spectrum. The relation that connects FWHM with temperature is the following

$$FWHM(T) = \Gamma_o + \gamma_{ph}T + \frac{\Gamma_{LO}}{[e^{h\nu_{LO}/kT} - 1]} \quad (6.2)$$

where Γ_o is of inhomogeneous origin linewidth at 0 K, γ_{ph} is electron-acoustic phonon coupling constant and Γ_{LO} is the strength of electron-LO phonon interaction [81]. LO phonon energies $h\nu_{LO}$ are of the order of 91 meV in GaN.

For all PL measurements, samples were mounted on a closed-cycle Helium cryosystem with a vacuum pressure system of 10^{-6} mbar by the aid of a mechanical and a turbo pump. The samples were excited by a 325 nm CW Kimmon IK He - Cd laser and analyzed through an ACTON i500 spectrometer with a resolution of 0.08 nm by using a 600 grating and a 50 µm slit. Neutral density filters were used to adjust the excitation power of the laser and the analyzed spectrum was then recorded by a nitrogen-cooled CCD camera connected to a computer. Temperature dependent PL measurements were done by using Scientific Instruments, series 5500 temperature controller.

6.2. Reflectance

When electromagnetic wave hits a surface or interface, with media having different refractive indices, two processes may occur, reflection and transmission. The fraction of this incident power which is not penetrated in the other medium is the reflectance. Reflectance is a positive number and mathematically can be expressed as the square of the Fresnel reflection coefficient, which is obtained by the solution of Maxwell's equations [14]. For oblique angles of incidence a mixture of s- (TE wave) and p- (TM wave) polarizations occur.

For obtaining Reflectance data, white light has to be used which contains wavelengths from ultraviolet to far infrared. This is done because each wavelength will respond differently when interacting with an interface. As illustrated in Figure 6.3, the only difference between PL and Reflectance setup is that the excitation is a DH 2000 Deuterium - Halogen white light source with the aid of an optical fiber to illuminate the samples on small areas.

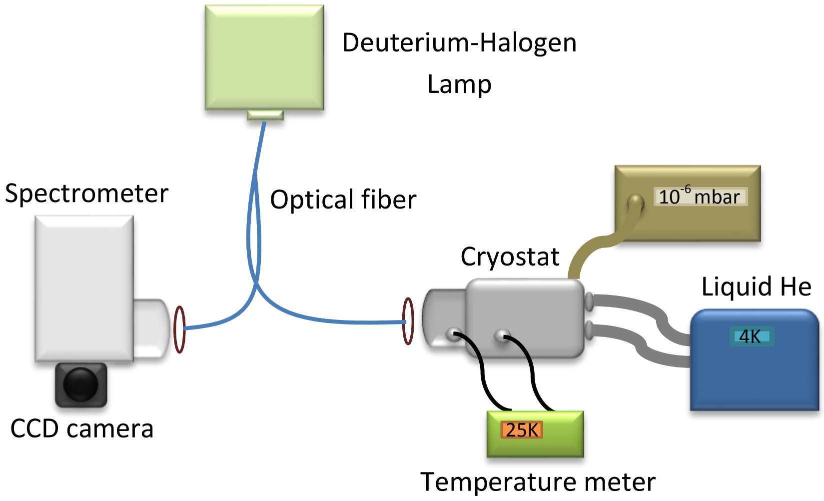

Figure 6.3 Illustration of the Reflectance setup where excitation was done by a white-light source at different temperatures and focused onto the sample and spectrometer by the aid of an optical fiber.

Reflectance spectra are very useful in confined structures such as quantum wells where excitonic transitions are likely to occur due to the strong overlap of the electron-hole pair and can alter the dielectric function of the material. As a result, this has a direct response to the reflectance spectrum and can be seen as an abrupt change. Hence, a reflectance spectrum in combination to a photoluminescence spectrum can determine which features are excitonic transitions. This information is vital in understanding the transitions occurring inside the QW for designing a more eligible microcavity.

Apart from finding excitonic transitions, Reflectance can be used in Distributed Bragg Reflectors (DBR) multilayered structures. DBRs are used as mirrors in microcavity structures, thus it is important to know the region where Reflectance is close to unity. By measuring reflectance data and analyzing them through a spectrometer one obtains a plot like in Figure 6.4. The spectrum exhibits two oscillating side-lobes and a central high reflectivity stop-band. By adjusting the contrast of refractive indices and the thicknesses of the DBR alternating layers, the desired reflectivity response of the DBR mirror can be obtained. The bandwidth of the Bragg reflector ("stop-band"), determined by the forbidden band of the periodic layered structure, is given by

$$\Delta\lambda = \frac{8c}{\lambda_c}\left(\frac{\pi}{2} - arccos\frac{n_2-n_1}{n_2+n_1}\right) \approx \frac{8c}{\lambda_c}\left(\frac{n_2-n_1}{n_2+n_1}\right) \quad (6.3)$$

where n_1 and n_2 are the alternating refractive indices and λ_c is the design wavelength of the cavity [1].

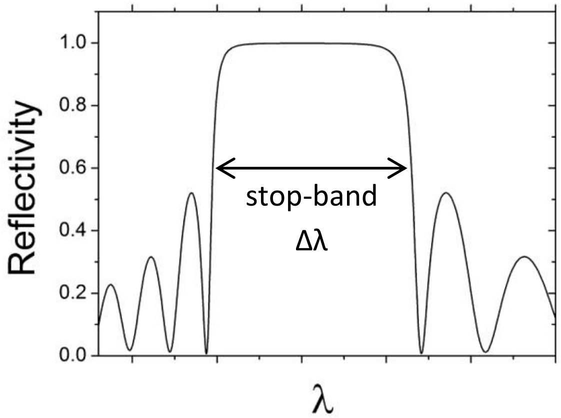

Figure 6.4 Reflectance dispersion spectrum exhibiting a stop band region at the center and two oscillating lobes at the two sides [82].

As concerns planar microcavities, a defect/active layer is sandwiched between two DBR mirrors for successful light trapping. Reflectance spectra can show directly if excitons are strongly coupled to cavity modes by the appearance of two pronounced features in the spectra, corresponding to lower polariton (LP) and upper polariton (UP) states [83]. The minimum energy difference between the two dips in the reflectivity is named as Rabi splitting Ω_R and is controlled by the properties of the quantum wells and the cavity.

All Reflectance simulations for the DBR and microcavity structures that are presented in this thesis were calculated with the use of a Matlab code written by Dr. Rahul Jayaprakash in combination with the input parameters of each structure. The code follows the transfer matrix method (TMM) (Appendix B) [84] to simulate the structures, where the contribution of the field components from all layers are described by an effective transfer matrix $M_{Total} = M_m M_{m-1} \dots M_1$. The Sellmeier formula was used in simulating the refractive index dependence on the wavelength for our materials defined as

$$n(\lambda)^2 = 1 + \sum_{i=1}^{m} A_i \frac{\lambda^2}{\lambda^2-\lambda_i} \quad (6.4)$$

where in most of the cases m = 3 is enough to express any material and for this reason the name Sellmeier equation often refers the equation with the three oscillator terms. In essence, by using at least 6 different wavelengths we can calculate the 6 constants A_1, A_2, A_3, λ_1, λ_2 and λ_3 of the equation and approximate the dispersion curve.

7. Photo-electrochemical Etching

7.1. InGaN as a sacrificial etching layer

Photo-electrochemical wet etching (PEC) technique was originally developed by Minsky et al. to etch group III nitride materials under ambient conditions [85]. The method is characterized by minimal damage to surrounding areas, rapid etch rates, lateral, anisotropic and bandgap selective etching relative to the direction and the wavelength of the photo-excitation used. Other wet-etching methods are isotropic and are too slow for efficient processing. On the other hand, current dry-etching methods have failed to produce the desired result due to ion induced damages resulting in rough surfaces [86].

Figure 7.1 depicts the energy band diagrams for n-type InGaN in contact with an electrolyte under several conditions. In the first case, where equilibrium is reached between sample and solution, the Fermi level (E_F) is equal to the redox potential (E_{redox}) of the KOH solution if no UV laser light is used to illuminate the semiconductor. If UV laser light, with above-bandgap energy, is on and circuit is shorted, there will be light-induced generation of electrons and holes in the space charge region. As illustrated in the second case (Fig. 7.1 (b)), the photo-generated electrons are pushed into the bulk of the semiconductor by the built-in electric field (F_{bi}), which then raise E_F and generate a photo-voltage V_{ph}. On the other hand, photo-generated holes move toward and accumulate at the surface. This hole accumulation is fundamental to PEC etching, since the presence of a hole at the surface works essentially as a broken chemical bond. As a result, the holes facilitate oxidation and dissolution of the semiconductor by the electrolyte. In the last case, a reverse bias V_r is applied to the semiconductor to ensure further confinement of the holes at the electrolyte/semiconductor interface.

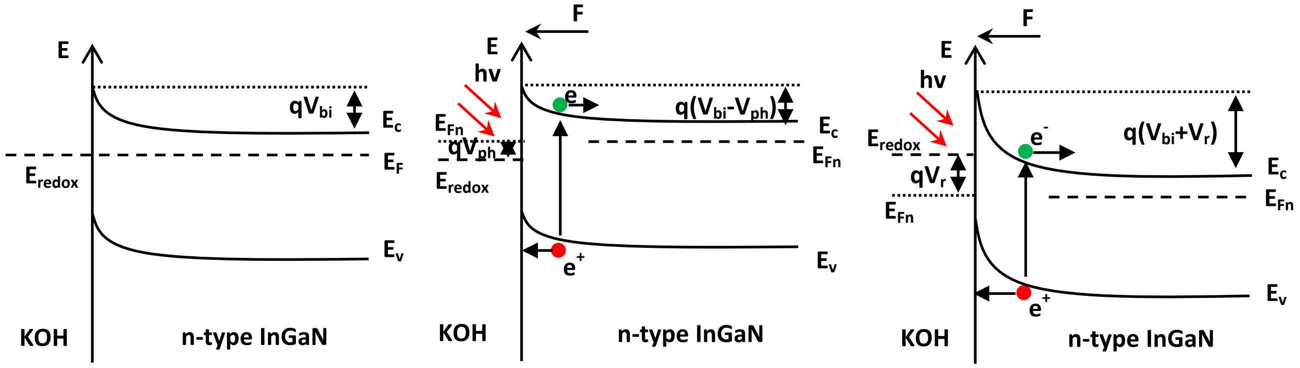

(a) (b) (c)

Figure 7.1 Energy bands of an electrolyte/n-type semiconductor interface showing the three most important states: (a) in equilibrium, (b) under illumination and (c) under illumination and a reverse applied bias V_r. Accumulation of holes is needed for the selectivity of PEC etching.

In PEC processing, a semiconductor is immersed in a conductive electrolyte with the sample acting as an anode and a dipped electrode (Platinum) in the electrolyte as a cathode. The illumination intensity is kept low to control etching rate and to avoid heating problems. The work function of the electrolytic solution depends on the PH value of the solution. Following previous work of Trichas et al. [87] and, more recent, Jayaprakash et al. [88], PEC was carried out in an electrochemical cell at room temperature by using a concentration of 0.0004 M KOH diluted in deionized water to successfully etch the InGaN sacrificial layer in the lateral direction and create high quality free-standing 200-nm thick AlGaN membranes and microdisks on pre-patterned samples by Reactive Ion Etching (RIE).

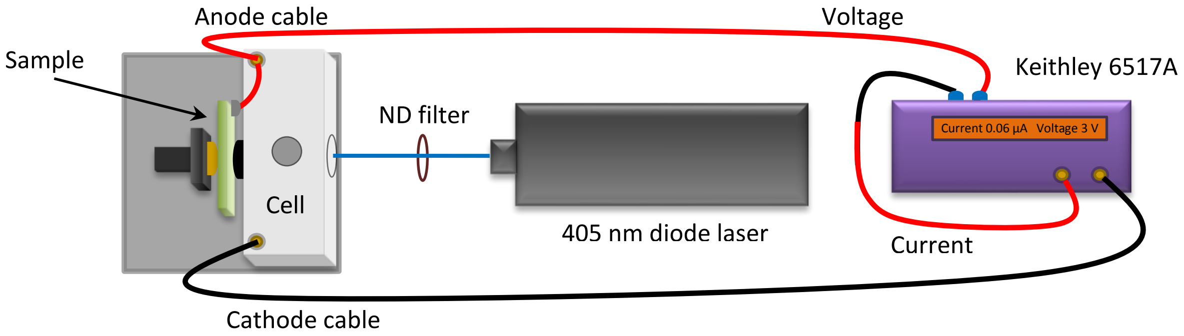

Figure 7.2 Schematic showing the Photo-electrochemical etching (PEC) setup where a diode laser is used as an excitation source. KOH is inside the electromechanical cell and the sample is stabilized on the back area vertically to the laser beam. The contact between the sample and KOH is through a pinhole.

In our experiments, for excitation we use a 405 nm diode laser with energy slightly above InGaN's, but below AlGaN's, bandgap. The etching was performed on a ring area of 0.78 mm^2, which was determined by a pinhole on the electrochemical cell. A Keithley 6517A power supply connected to a computer through an Agilent GPIB cable and the Agilent VEE software were used to apply the desired voltage and acquire the output current data versus time (I - t). By using this computer-based setup to plot the recorded data every second, we had a direct response of current values which helped us to observe any errors that could occur during etching process. An illustration of the PEC experimental setup is presented in Figure 7.2, where the sample (shown by the arrow) is held vertically to the laser beam behind the electromechanical cell. Excitation power can be adjusted by using a Neutral Density (ND) filter. The only contact between the sample and KOH was through the pinhole. The output result of an ideal I - t characteristic curve is shown in Figure 7.3.

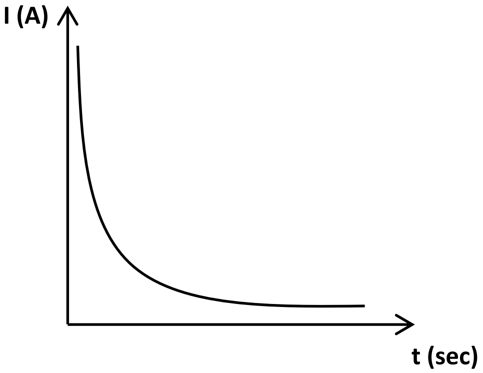

Figure 7.3 Characteristic I - t curve of the Photo-electrochemical (PEC) etching process showing the decay of current versus time due to reduced contact area between the two layers as they are being etched.

8. Theoretical design of the devices

8.1. E3364 and E3365 structures

Before the fabrication of any devices, a theoretical investigation was done in order to find the optimal parameters of each layer in the nitride structures. The idea was to place two sets of 4 QWs at the antinodes of the electric field inside the $3\lambda_c/2$ thick active region of the microcavity. The reason why we are using such a thick active region was just for mechanical stability. Two similar nitride configurations were designed with different Indium concentrations (x) in the sacrificial $In_xGa_{1-x}N$ layer (yellow color Fig. 8.1) as follows c-$Al_{0.07}Ga_{0.93}N$/c-$In_{0.13}Ga_{0.87}N$/c-GaN/c-Saphire (E3364) and c-$Al_{0.07}Ga_{0.93}N$/c-$In_{0.15}Ga_{0.85}n$/c-GaN/c-Saphire (E3365). Both samples were pseudomorphic on a c-GaN template and had two sets of 4 GaN/AlGaN Quantum Wells (red color Fig. 8.1) inside the c-AlGaN layer cited centrally at the antinodes of the electric field.

A similar pioneer active layer configuration has been reported by Houdré et al. in 1994 but for a GaAs-based structure [89]. By placing more than one QW at the antinode of the cavity mode, the total oscillator strength is maximized and thus, the vacuum Rabi coupling strength. Nevertheless, it has been reported by other groups [90; 64] that only up to 5 QWs at each antinode contribute to enhance the coupling. A higher number of them induces saturation and hence they are not essentially needed. The positions of the QWs resulted from calculations by considering an active layer thickness of $L_c = 3\lambda_c/2 = 211.2$ nm for the materials used.

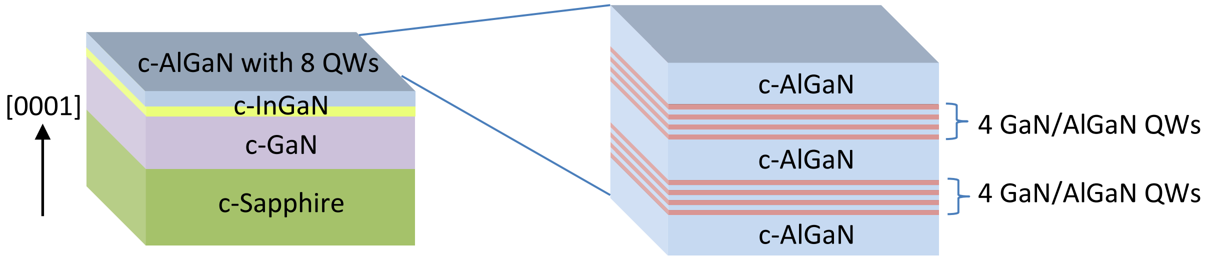

Figure 8.1 Schematic illustrating the theoretical design of the two structures with two sets of 4 GaN/AlGaN QWs embedded in the c-AlGaN layer. Aluminum concentration kept at 7 %.

The layer thicknesses and the concentrations of our theoretical design are summarized in Table 1. Indium concentration (x) in the InGaN layer was 0.13 and 0.15 for E3364 and E3365, respectively. As previously reported, when AlGaN is grown pseudomorphically on a GaN template, there is strain due to lattice mismatch at the interfaces which then induces piezoelectric polarization. For this reason, a low concentration of Al (7 %) was used to prevent any high built-in fields in the QWs resulting in a reduced binding energy of the exciton states. It should be reminded that even such low concentration of Al induces a field of ~ 450 kV/cm.

All the layers above the InGaN layer, as presented in Table 1, are the ones that are forming the membrane structure and, as will be later discussed, they were simulated with the Nextnano software [10] for extracting the A_x, B_x and C_x excitonic transitions of the QWs within the effective mass approximation and 8x8 k.p perturbation theory by varying the temperature for a more realistic evaluation of the obtained outcome.

Table 1: Theoretical design of both structures

	Thickness (nm)	Material	Concentration	
	60	c-Al$_x$Ga$_{1-x}$N	0.07	
	2.7	**c-GaN**	**-**	**4 periods**
	2.7	**c-Al$_x$Ga$_{1-x}$N**	**0.07**	
	50	c-Al$_x$Ga$_{1-x}$N	0.07	
	2.7	**c-GaN**	**-**	**4 periods**
	2.7	**c-Al$_x$Ga$_{1-x}$N**	**0.07**	
	58	c-Al$_x$Ga$_{1-x}$N	0.07	
Sacrificial layer	26	c-In$_x$Ga$_{1-x}$N	0.13 (E3364) / 0.15 (E3365)	
Pseudomorphic c-GaN	4000	c-GaN	-	
	∞	c-Sapphire	-	

As shown in Figure 8.2, refractive index variation and electric field distribution inside the microcavity were simulated with the Transfer Matrix Method (TMM). Membrane layer is sandwiched by 11 pairs of alternating high-low refractive indices in both sides for ensuring high confinement of the EM field. In real structures, one of the two sides must have less DBR layers to increase the propagation probability from that side. The thickness of the active layer equals the total membrane thickness.

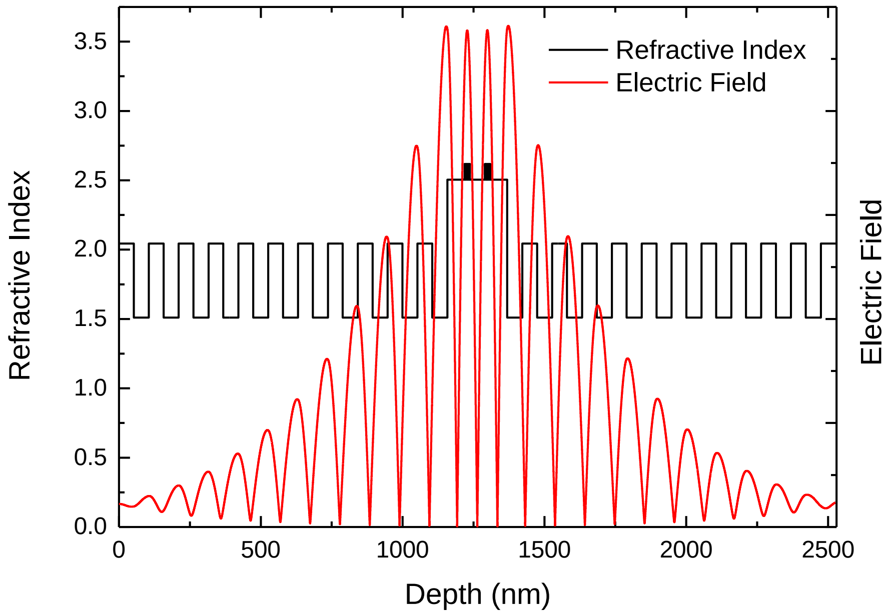

Figure 8.2 Illustration of the variation of the refractive indices and the distribution of the electric field inside the microcavity with two sets of 4 GaN/AlGaN (7 %) QWs embedded at the antinodes of the field in the cavity layer. DBRs consist of 11 pairs of Ta_2O_5 and SiO_2 as high and low refractive index dielectrics.

8.2. Fourier plane simulation of the ideal cavity mode at 365 nm

A complementary analysis, to the previous, is the simulation of the Fourier plane or $k_{//}$ – space imaging that can be obtained experimentally by detecting the PL at various angles. Similar to the cavity energy dispersion, Equation 4.6 holds also for the polaritons in a microcavity and can describe the connection between the energy of the polariton mode to the external angle. An up to date technique (Appendix D) is used to collect emitted photons by utilizing a high numerical aperture (NA) lens to analyze the sample's response on the monochromator's slit. $K_{//}$ - space imaging is vital, since it provides us with information about the distribution of polaritons inside the cavity. The angular resolution of the Fourier plane is determined every time by the pixel size of the CCD camera of the spectrometer. Although, small pixel sizes are required to attain high resolution images, the size is limited to values close to the resolution of the spectrometer. Typical values are at the order of 25 μm.

The obtained data, based on simulations, of the ideally designed microcavity with a cavity mode at exactly 365 nm ($k_{//} = 0$) are presented in Figure 13.1 (a), while the Fourier plane data for angles from - 40 up to 40 degrees are shown in Figure 13.1 (b). In the former, Absorption, Reflectance (blue color) and Transmission spectra (red color) are depicted, while in the latter only absorption spectrum is shown. Based on the previous maximum angle, the calculated $k_{//}$ reaches cavity states up to 2.3×10^{5} cm^{-1}. TE and TM modes have been accounted for in the simulated data as can be clearly seen in Bragg modes. However, in the cavity mode, it is difficult to distinguish them, due to low resolution of the illustrated image.

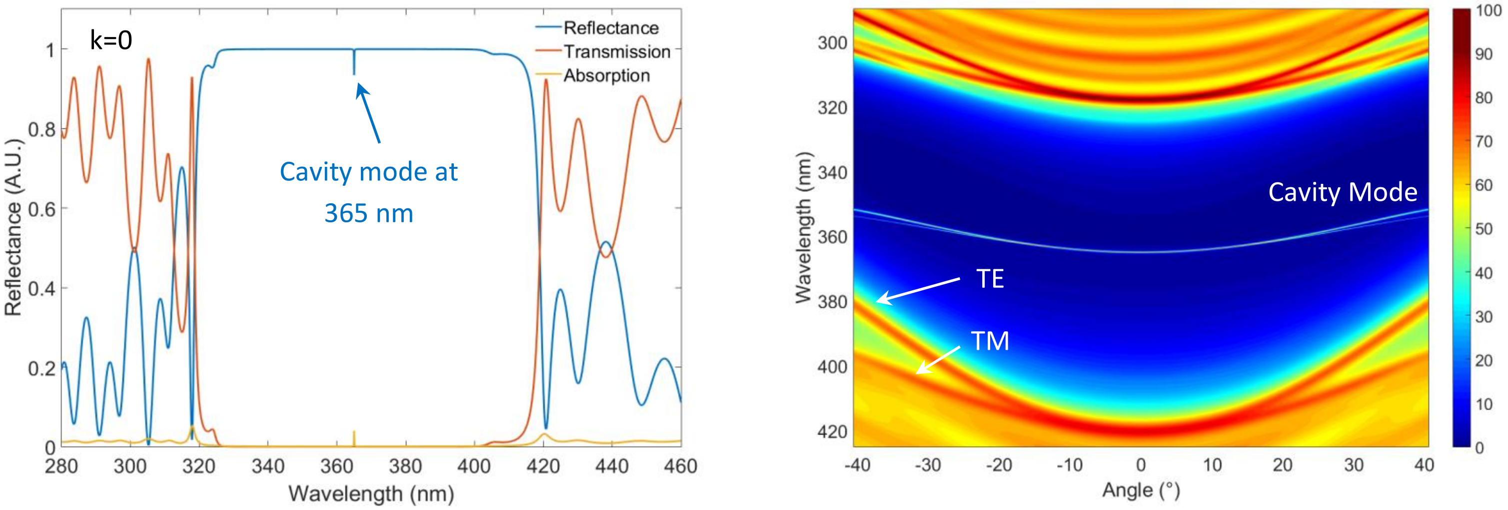

(a) **(b)**

Figure 13.1 Simulation of (a) Reflectance, Transmission and Absorption spectra at $k_{//} = 0$ and (b) Fourier plane of Absorption spectra of an ideal microcavity structure with a cavity mode at 365 nm. The column on the right indicates which colors are attributed to the high and low absorption values and does not represent a real range.

By applying all the necessary input parameters of the mixed exciton state $A_x + B_x$ in the Matlab code, and by using a theoretical value for the oscillator strength, we obtained the data summarized in Figure 13.2. Here, the microcavity structure is operating in the strong coupling regime, as can be observed from the anticrossing at 30 degrees of the external angle, while there is generation of the two lower (LPB) and upper (UPB) polariton branches, as seen in Figure 13.2 (b). The wavelength values of the LPB and UPB at $k_{//} = 0$ are 366 nm and 357 nm (Fig 13.2 (a)), respectively, while the Rabi splitting (Ω) at the anticrossing point in wavelength scale is ~ 4.5 nm.

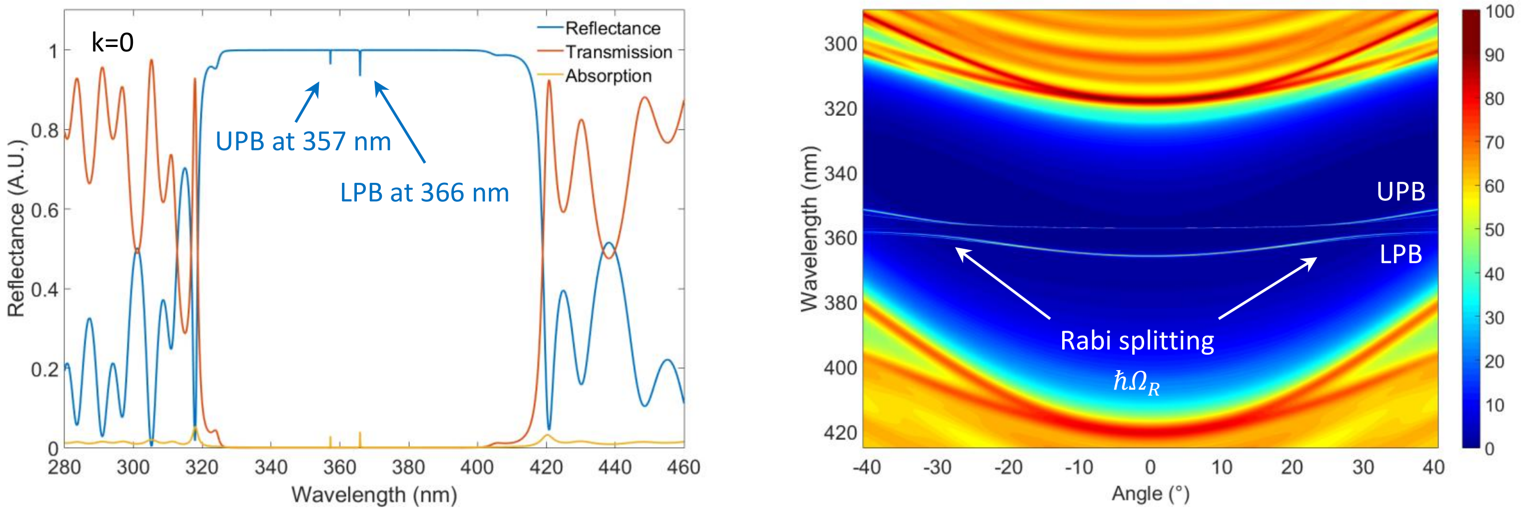

(a) **(b)**

Figure 13.2 Simulation of (a) Reflectance, Transmission and Absorption spectra at $k_{//} = 0$ and (b) Fourier plane of Absorption spectra of an ideal microcavity structure with a cavity mode at 365 nm operating in strong coupling regime. The column on the right indicates which colors are attributed to the high and low absorption values and does not represent a real range.

To move on, simulations of the Fourier planes of the fabricated structures were not performed, since we were not able to observe neither the cavity mode, nor the polariton branches in our devices, as will be later examined. By managing to simulate the exact cavity mode and polariton branches, we would be able to extract a value for the oscillator strength, coming from the electron-hole interaction. This value can be numerically calculated by measuring the Rabi energy splitting $(\hbar\Omega_R)$ of the polariton branches, which, as already discussed earlier, arises from the strong coupling between exciton and confined light.

Based on previous samples, it has been reported a Rabi splitting energies at the order of 64 meV for 33 GaN/AlGaN QWs embedded in the membrane structure with a GaN spacer layer added at the end to fulfill the standing wave condition. Therefore, the QWs were not only at the antinodes, but also at the nodes positions of the electric field. Hence, they would have a reduced performance in comparison to our new samples, where the QWs were placed only at the two antinode positions. Thus, a lower threshold power density would be expected.

9. Characterization of as-grown E3364 and E3365 samples

9.1. X-Ray Diffraction

In the first sample named as E3364, the Indium content was kept lower (x = 0.13) that in the second (x = 0.15), which was named as E3365. This was done deliberately in order to understand the correlation of the Indium concentration in the photo-electrochemical process. Finding the optimal parameters towards smoother PEC surfaces can be a significant advantage in this technique. Both samples were designed here but fabricated in Grenoble, in France. The growth direction was along [0001] by plasma-assisted molecular beam epitaxy (MBE) on 4 μm c-grown GaN non-intentionally doped (n ~ 10^{17} cm^{-3}) templates by metal organic chemical vapor deposition on Sapphire taken from Lumilog.

In order to determine any deviations from the theoretical values, X-Ray Diffraction (XRD) characterization, by a BEDE D1 High Resolution X-Ray Diffractometer, took place. In Figure 9.1 is presented the XRD intensity versus angle in a θ - 2θ scan for both samples, with the obtained data denoted by the black line, while the corresponding simulation by the red line, respectively. As illustrated in Tables 9.1 - 9.2, it was found that the concentration of the InGaN layer was 13.1 ± 0.3 % for E3364, while for E3365 was 14.6 ± 0.3 %. As concerns the AlGaN layers, it resulted that for E3364 the first set of QW had an Al content of 5.0 ± 1.0 % while the second set 7.2 ± 1.0 %. On the other hand, for the E3365, it was indicated that the concentration of all AlGaN layers was at 5.0 ± 1.0 %.

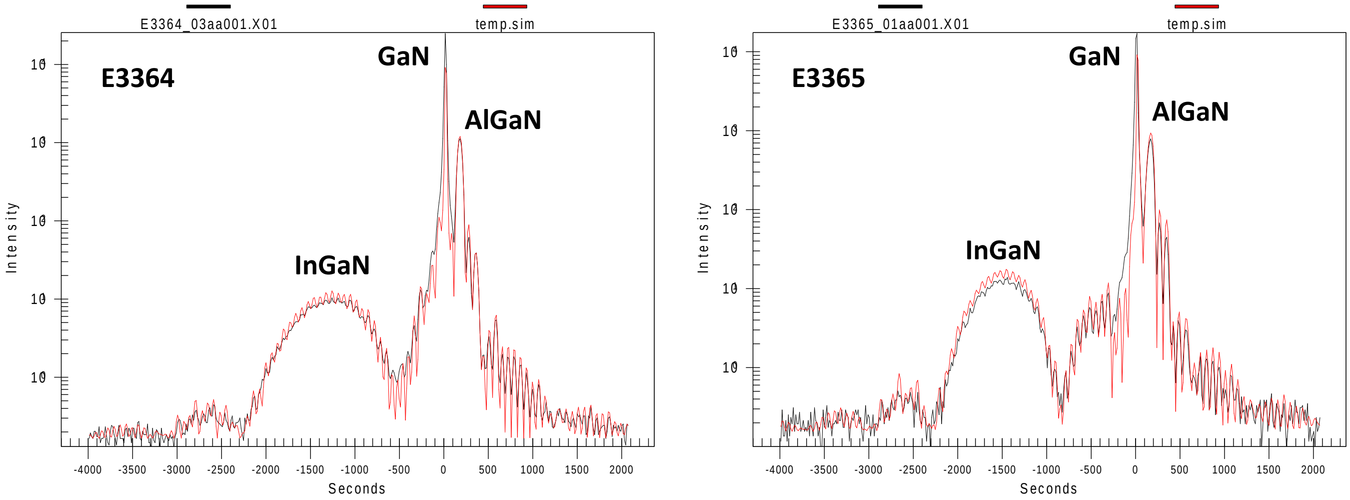

(a) **(b)**

Figure 9.1 XRD intensity versus angle in a θ - 2θ scan for (a) E3364 and (b) E3365. Black line indicates the measured data while the red line the simulation.

Additionally, XRD measurement showed that the thicknesses of all layers have variations from the ideal structure. It is worth noting that XRD uses a fitting curve (Fig. 9.1) of the measured data to simulate and give the output values. Therefore, this fitting cannot be very accurate for the thickness of thin layers such as the QWs and cannot be taken as granted. However, the total thickness of the cavity, as well as the position of the QWs, are of great importance, as already discussed in theory, and should be taken into consideration. By summing the thickness data of each table, we obtain 234.1 for the E3364 and 228.6 nm for the E3365, respectively.

For this purpose, the profilometry of few membranes was measured for both samples and the resulted thicknesses were approximately 245 nm for E3364 and 240 nm for the E3365. As can be concluded, profilometric data showed ~ 10 nm higher values than XRD results, and thus indicating that our membranes were thicker than nominal. Further proof of that, as will be shown later, was confirmed by SEM characterization of a single membrane. The resulted thickness based on SEM for the specific membrane was around 232 nm, while in profilometry it was found to be 244 nm thick.

Table 9.1: XRD results for E3364

Thickness (± 2 nm)	Material	Concentration (x ± 1%)	
66.95	c-Al$_x$Ga$_{1-x}$N	5.5	
3.50	**c-GaN**	**-**	**4 periods**
2.03	**c-Al$_x$Ga$_{1-x}$N**	**5.0**	
56.10	c-Al$_x$Ga$_{1-x}$N	5.0	
2.86	**c-GaN**	**-**	**4 periods**
3.49	**c-Al$_x$Ga$_{1-x}$N**	**7.2**	
63.53	c-Al$_x$Ga$_{1-x}$N	5.2	
18.63	c-In$_x$Ga$_{1-x}$N	13.1 ± 0.3	
∞	GaN	-	
∞	Sapphire	-	

Table 9.2: XRD results for E3365

Layers used in Nextnano and Matlab for experimental data simulation

Thickness (± 2 nm)	Material	Concentration (x ± 1%)	
63.05	c-Al$_x$Ga$_{1-x}$N	5.0	
3.50	**c-GaN**	**-**	**4 periods**
2.96	**c-Al$_x$Ga$_{1-x}$N**	**5.0**	
52.65	c-Al$_x$Ga$_{1-x}$N	5.0	
3.50	**c-GaN**	**-**	**4 periods**
2.09	**c-Al$_x$Ga$_{1-x}$N**	**5.0**	
64.72	c-Al$_x$Ga$_{1-x}$N	5.0	
22.97	c-In$_x$Ga$_{1-x}$N	14.6 ± 0.3	
∞	GaN	-	
∞	Sapphire	-	

Furthermore, as we will later observe in the optical characterization (Fig. 9.2 and 9.3), there is a deviation in the photoluminescence peak between the two samples at the AlGaN exciton region with the E3365 having a more sharp but of lower energy peak. This deviation probably results from the non-intentionally Aluminum variation in AlGaN layers. As regards the InGaN layer, Indium content will be under examination when evaluating the results of the photo-electrochemical process, since the role of InGaN was solely for the fabrication of the free-standing membranes and the standing microdisks.

9.2. Photoluminescence and Reflectance

After XRD characterization, Reflectance and Photoluminescence measurements were performed (before any etching occurred) first at low T (Fig. 9.3 - 9.4) and then by varying temperature (Fig. 9.5) and excitation power (Fig. 9.10) for further investigation. These two measurements can fully identify a sample's transitions in combination with appropriate modelling. Since the most important transitions, for a microcavity operating in the strong coupling regime, are the excitonic transitions inside the QWs (high intensities and small linewidth), understanding their behavior from cryogenic up to room temperature could provide vital information.

As stated earlier in theory, abrupt changes in a reflectivity spectrum can arise due to absorption from excitonic transitions, which alternate the dielectric function of the material. The reflected electromagnetic waves have a direct response to a sample's excitonic transitions, this is shown as a change in slope (Fig. 9.2). At low temperatures, as seen in Figures 9.2 - 9.3 and more clear in Figure 9.4, the most significant features are the changes in slope at and next to the profound dip in reflectivity at 3.50 - 3.52 eV energy range defined as A_x, B_x (dashed and dotted lines). The dashed lines represent the A_x exciton, while the dotted lines the B_x exciton transitions in the quantum wells. The obtained values for E3364 are 3.5075 and 3.5193, while for E3365 are 3.5051 and 3.5176, respectively.

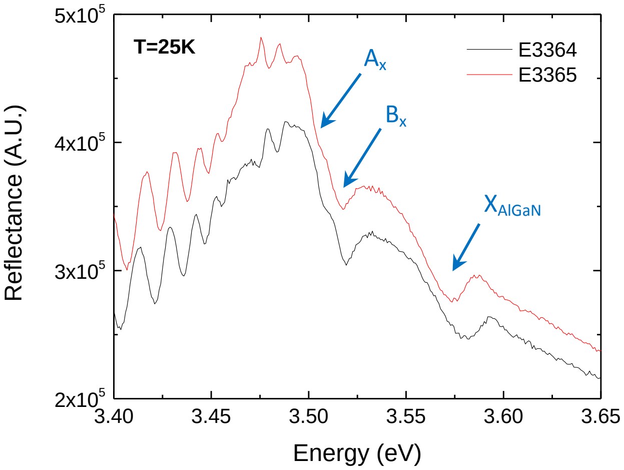

Figure 9.2 Reflectance spectra at T = 25 K before etching for E3364 and E3365. The arrows indicate the changes in slope coming from A_x and B_x QW and X_{AlGaN} exciton transitions for both samples, which exhibit similar characteristics.

The large emission at 3.450 - 3.520 eV in the PL spectrum at 25 K comes from Localized QW excitons defined as L_x. Here, L_x exciton for E3364 is at 3.490 eV, while for E3365 is at 3.488 eV. The dashed-dotted lines represent the bulk AlGaN exciton transition named as X_{AlGaN} corresponding to 3.582 eV for E3364 and 3.573 eV for E3365. These energies correspond to ~ 5.0 % Al concentrations based on G. Coli et al. [91]. Previous work in our group further confirms our results as described in reference [92]. As was analysed from the PL data, the high energy peak of X_{AlGaN} for the E3365 sample was found to have higher intensity in contradiction to that of the E3364 sample.

As concerns the two peaks at lower energies, they are LO phonon replicas of the localized excitons in the QWs as they are at energy distances ~ 91 meV and ~ 182 meV, respectively. In Reflectivity data, the low energy side in both samples is attributed to Fabry-Perot oscillations in the transparent region of the spectrum. Since the period of oscillations has a direct dependence on the thickness of the template, by measuring the energy difference between two successive peaks ΔE ~ 40 meV and doing some basic calculations, one may conclude that the resulted thickness is at the order of 5 μm. As reported from Lumilog corporation, the GaN layer grown on Sapphire template had a total thickness of around 4 μm, which is compatible with the experimental values.

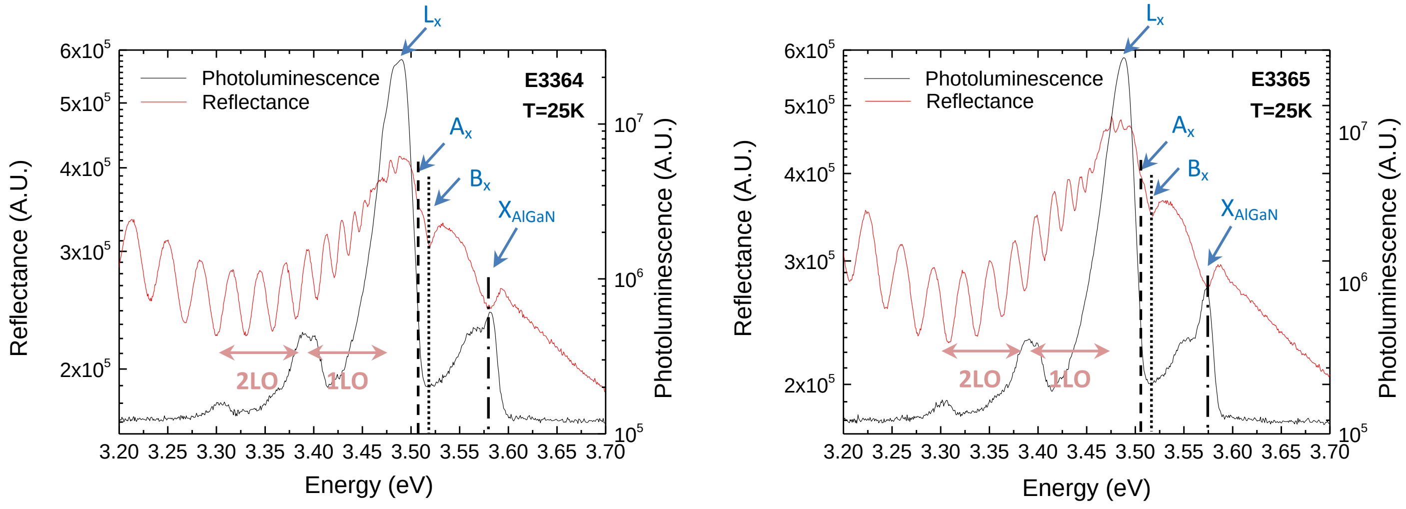

(a) **(b)**

Figure 9.3 Reflectance and PL spectra at T = 25 K before etching for E3364 (a) and E3365 (b). Dashed and dotted lines represent A_x and B_x exciton transitions in the QWs, whereas the dashed-dotted line represents X_{AlGaN} exciton transition. Localized (L_x) QW excitons account for the PL maximum peak.

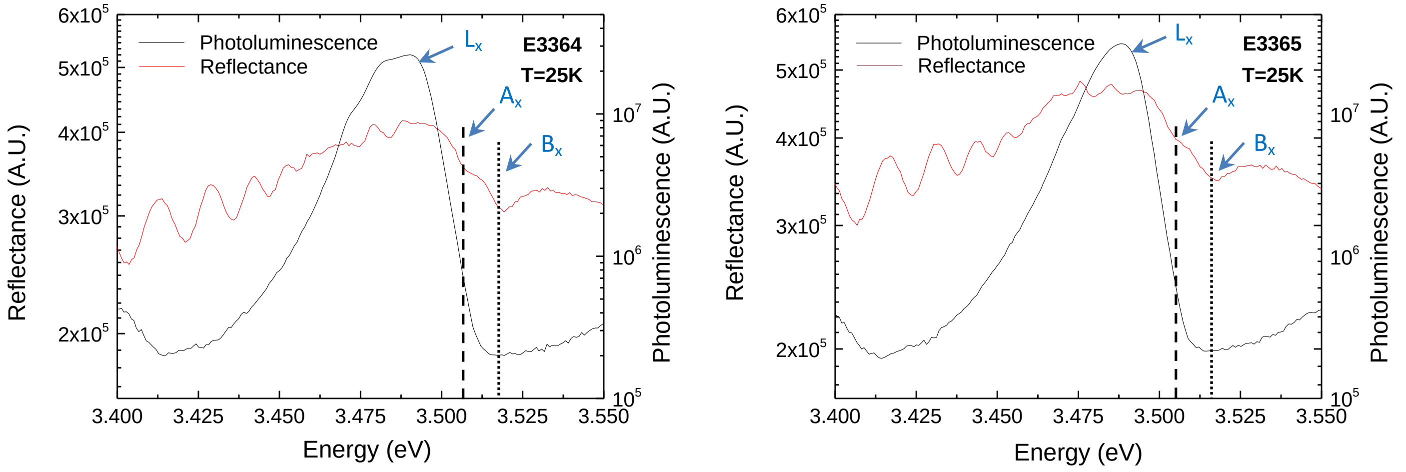

Figure 9.4 Zoom of the previous Reflectance and PL spectra at T = 25 K before etching for E3364 (a) and E3365 (b). Dashed and dotted lines represent A_x and B_x exciton transitions in the QWs. Localized (L_x) QW excitons account for the PL maximum peak.

By analyzing the temperature dependence of the two samples from 25 up to 300 K, we obtain the data presented in Figure 9.5. An important simplification to observe the variation with temperature is by taking the PL emission maximum for all temperatures [93; 94] and making new plots for both structures similar to Figure 9.6. An S-shaped behavior results from delocalization of carriers from the localized levels to the free-exciton states. This curve is a deviation from the expected Varshni fitting equation and is observed at temperatures below 150 K, while for larger values it disappears due to the complete ionization of the localized states. As can be seen for increased values of temperature (Fig. 9.5), there is linewidth broadening attributed to the exciton-phonon interactions, as already discussed before.

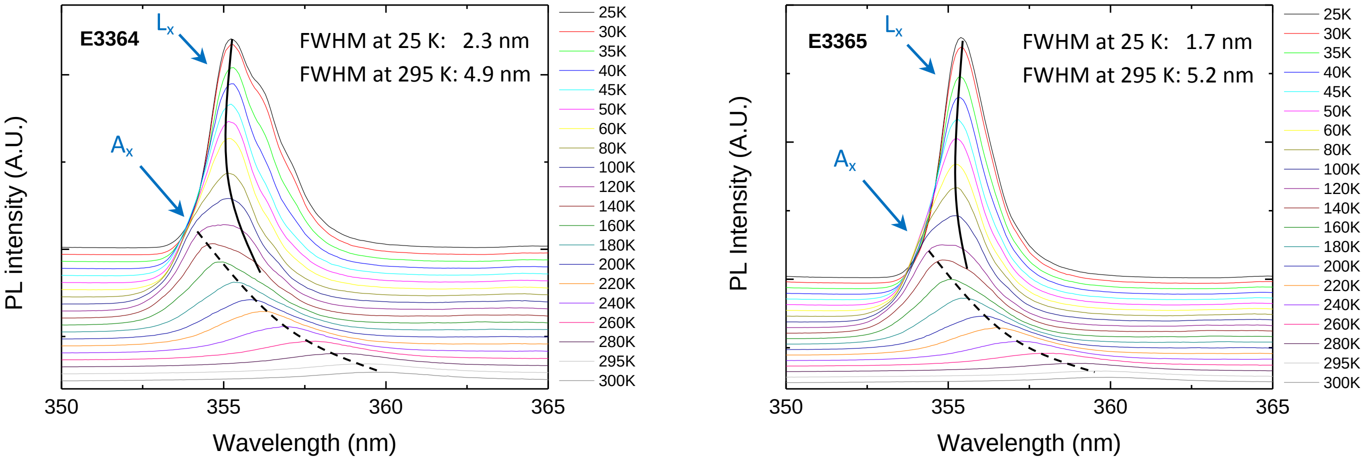

(a) **(b)**

Figure 9.5 PL intensity versus wavelength for T = 25 - 300 K before PEC for E3364 (a) and E3365 (b).

As depicted in Figure 9.6, at temperatures close to zero, localized exciton recombination dominates and the carriers thermalize to a 1st local minimum. At slightly higher temperatures, the excitons are thermally transferred to higher energy states in the local potential (1st blueshift). As the temperature rises (above 50 K), at low excitation intensity, the excitons have enough thermal energy to overcome the barriers of the local potential and relax to a 2nd potential minimum (1st redshift). These two, previously mentioned, minima are indicated by the blue arrows in Figure 9.6. An additional increase in temperature, forces excitons to reach higher energy states of the conduction band edge (2nd blueshift). For values above 140 K, there is no thermal localization and the spectrum follows the free exciton recombination (2nd redshift). For even higher temperatures, free A_x and B_x excitons are having a strong overlap due to phonon broadening and at room temperature they become one distinct peak.

As can be concluded, the simple graphs of Figure 9.6 can provide valuable information for the behavior of the energy states from low up to room temperatures. Depending on the number of data points used, one may have a more accurate and detailed representation of the shape of the plot. The temperature steps (5 - 20 K) that were utilized here were sufficient for estimating and describing both the two local minima and the Varshni fitting (as referred in the next paragraph) for our devices. The obtained data of E3365 sample were further compared to the Nextnano results, as will be explained later, and a conclusion is made.

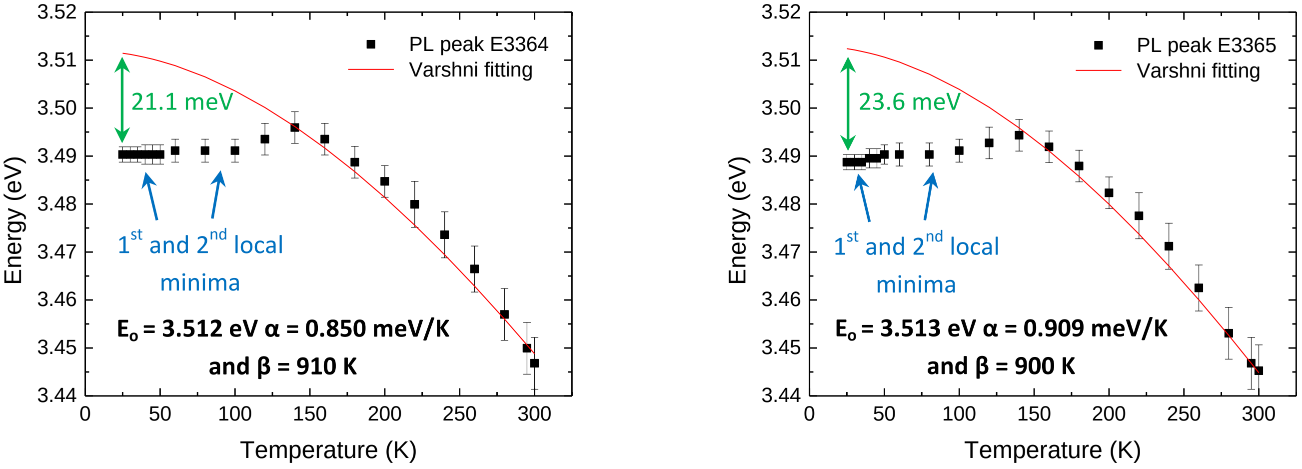

(a) **(b)**

Figure 9.6 PL peak energy versus temperature extracted from spectra in Figure 9.5 along with Varshni fitting (red solid line) for E3364 (a) and E3365 (b). The two local minima (blue color) and the localization energy (green color) are also shown.

The red solid curves in Figure 9.6 correspond to the best Varshni equation fitting (assuming no localization) at elevated temperatures based on the relation

$$E_g(T) = E_g(0) - \frac{aT^2}{(T+\beta)} \quad (9.1)$$

where $E_g(0)$ is the transition energy at T = 0 K and α and β are the Varshni thermal coefficients. For a most appropriate model, one should account also the S-shape of the graphs in the simulation equation by adding an extra term, as in reference [13], but here it was not necessary. The α and β Varshni parameters for bulk GaN are 0.909 meV/K and 830 K [95], respectively. The obtained values for our structures are E_o = 3.512 eV, α = 0.850 meV and β = 910 K for E3364 and E_o = 3.513 eV, α = 0.909 meV and β = 900 K for E3365. From the previous data, it was derived that the localization energy (green label) is 21.1 meV for E3364 and 23.6 meV for E3365, respectively.

In Figure 9.7 (a), is presented the coevolution and coalescence of the A_x and B_x excitons from low up to room temperature based on Reflectivity measurements. Nevertheless, C_x exciton could not be identified from the optical characterization. As regards A_x and B_x excitons, they are overlapping at high temperatures and cannot be distinguished as separate features. In Figure 9.7 (b) is shown the Reflectance in comparison with the Photoluminescence at 295 K for a more clear view of the overlapping. At room temperature, there is also a small contribution from the bulk AlGaN excitons at higher energy due to its close proximity to the QW excitons, as indicated in the Figure 9.7 (b), which increase slightly the Full Width at Half Maximum (FWHM). The PL energy peak at 295 K obtained from E3365 is located at 3.447 eV, whereas for E3364 is at 3.450 eV. The near identical room temperature PL spectra of the two samples are given in Figure 9.8.

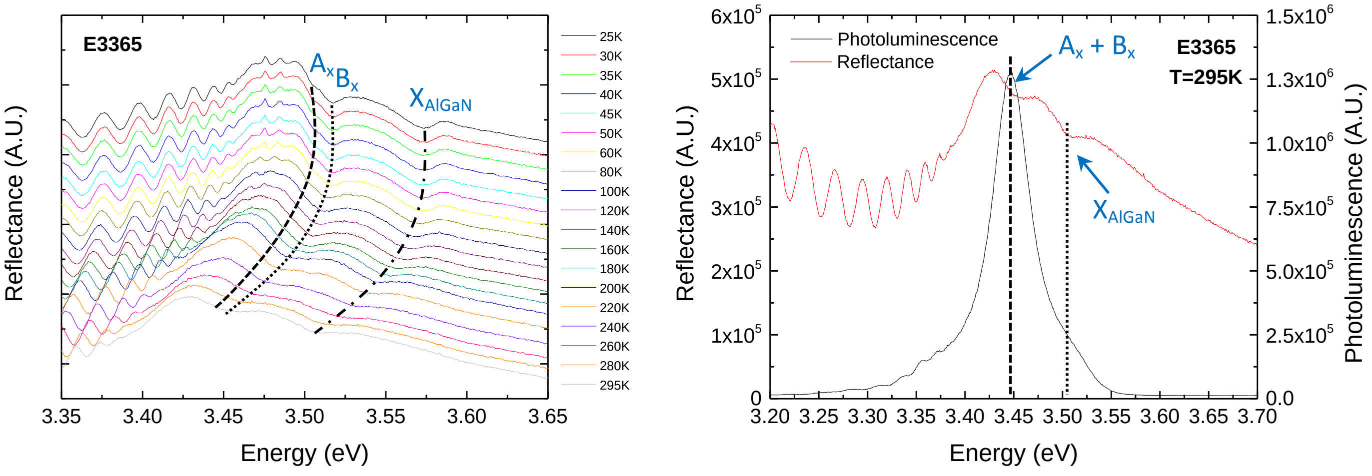

(a) **(b)**

Figure 9.7 (a) Reflectance versus energy for T = 25 - 295 K (dashed A_x, dotted B_x and dashed-dotted X_{AlGaN} exciton lines) and (b) room temperature PL and Reflectance of the E3365 sample (dashed line $A_x + B_x$ excitons and dotted X_{AlGaN} exciton).

Based on Figure 9.8, the microcavity design wavelength was tried to be at 365 nm, so that exciton energy will be close to the cavity photon energy. In this case, there will be a small negative detuning $\delta = E_{cav} - E_{exc} < 0$ of the order of 50 – 70 meV. The final result might be altered depending on the center of the DBR mirror or membrane thicknesses, which are crucial factors for having a well-defined cavity mode. Moreover, we note in Figure 9.8, a slight difference in FWHM between the two samples (~ 0.3 nm),with E3364 having a lower value than E3365.

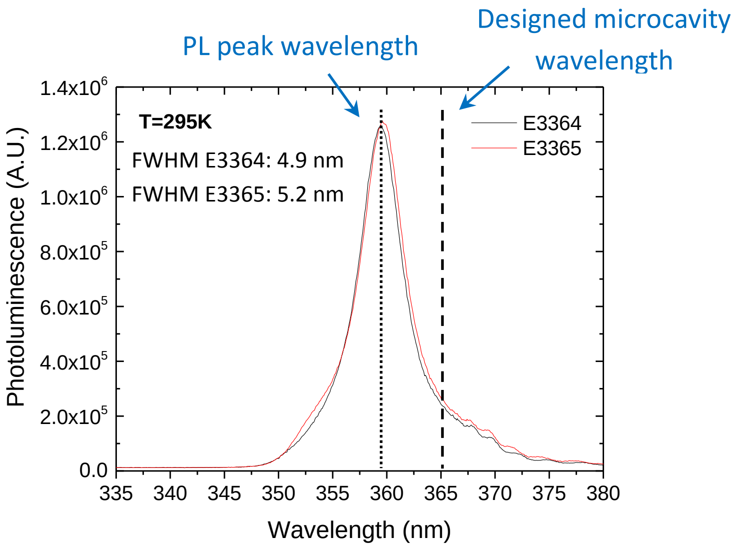

Figure 9.8 Room temperature photoluminescence of the two structures showing that the PL peak wavelength is near the designed wavelength of 365 nm. In this case, the microcavity is negatively detuned (δ < 0).

The next step was to collect PL data from various points on each sample, as outlined in Figures 9.9 and 9.10 to characterize the degree of homogeneity. The distance between the spots was < 0.5 cm. By mapping the two structures, it was easy to compare the spectra and observe any variations along the x,y plane directions, while check the consistency of the QWs and InGaN energy region. It was observed that the QW region had no significant deviation (~ 3 meV) for both samples in contradiction to the InGaN region which exhibits substantial variation in the emission energy (~ 47 meV) corresponding to deviation of In-content of 1 – 1.5 %. More specifically, the variation of Indium was around 1 % for E3364, whereas for E3365 it was approximately 1.5 % based on the work of W. Shan et al. [26].

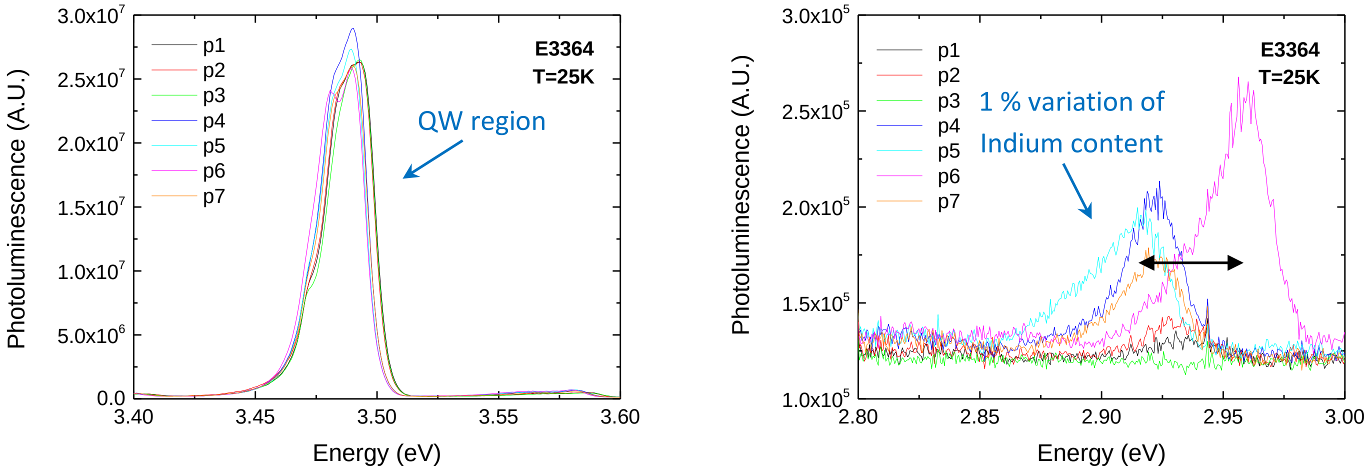

(a) **(b)**

Figure 9.9 PL versus energy at various spots on the E3364 sample at 25 K with (a) showing the exciton region and (b) showing the variation of Indium content at the InGaN layer of the same spectra.

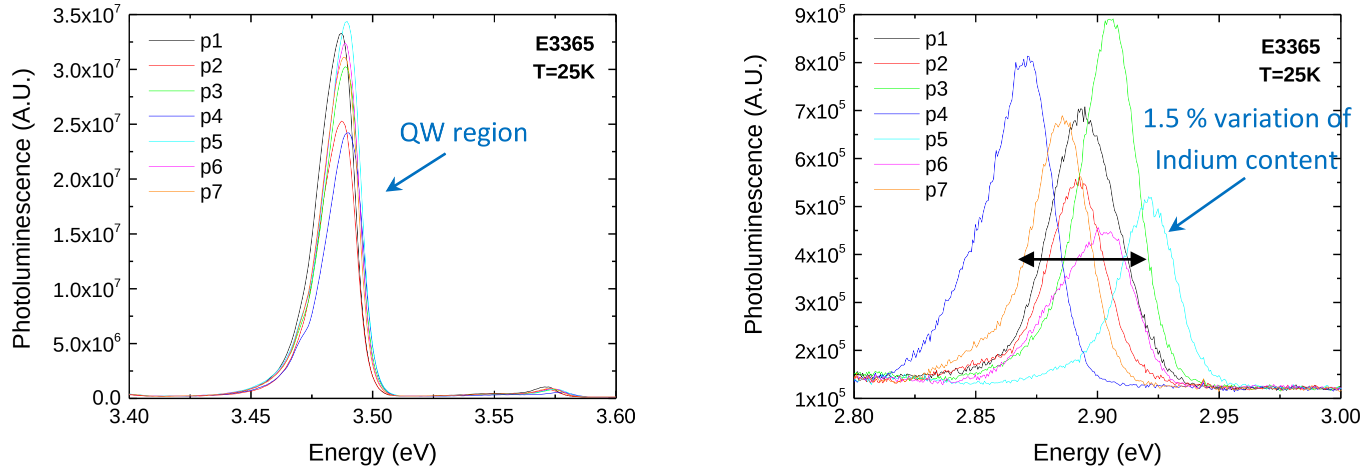

(a) **(b)**

Figure 9.10 PL versus energy at various spots on the E3365 sample at 25 K with (a) showing the exciton region and (b) showing the variation of Indium content at the InGaN layer of the same spectra.

The analyzed PL spectra revealed that the InGaN layer for both structures was not uniform across the sample. Between the two samples, InGaN of E3365 was found to be at lower energies, meaning that the concentration of In was higher in this sample in agreement with XRD characterization. A conclusion, based on the above, is that it is preferable to use low concentrations of Indium for more uniform InGaN layers. Furthermore, it should be pointed here that p7 (orange color) in the PL spectra corresponds to the point at the center of the two samples, while the other points were taken from the periphery.

To move on, the PL of the central point (p7) was taken for both samples by varying the excitation power at 25 K. This was accomplished by using Neutral Density (ND) filters of different optical density values (ND 0.1 - 4.0), which were placed in the incident beam path. The maximum output power of our He - Cd 325 nm laser was measured with a power meter and found to be approximately 30 mW. The extracted data based on the PL measurements are presented in the two plots in Figure 9.11. As revealed, by decreasing the incident power, two overlapping peaks can be distinguished at the QW energy region of E3364 sample, in comparison to the E3365 which exhibits single peak character. It is estimated that the lower energy peak is also arising due to QW-related localized states and, therefore is named as L_{x2} and is defined as “deeper localized QW states”.. L_{x2}, which is located at the energy of 3.464 eV, is shown in both plots for a more clear understanding of the position of those states.

Moreover, as can be concluded from the spectra, these states have a negative effect on the FWHM of the PL peak maximum of the QWs at low T. Having a huge linewidth is not desirable to such structures since it has a negative contribution to the exciton-photon interaction at the polariton microcavity. Sample E3365 (Fig. 9.11 (a)) is found to be less affected from these states, in contradiction to E3364 (Fig. 9.11 (b)), probably due to the better quantum well structure. However, no further analysis was done to explore other effects of the deeper states or have a better explanation why they arise only in E3364, since the purpose of this thesis was to fabricate a real polariton structure operating in the strong coupling regime.

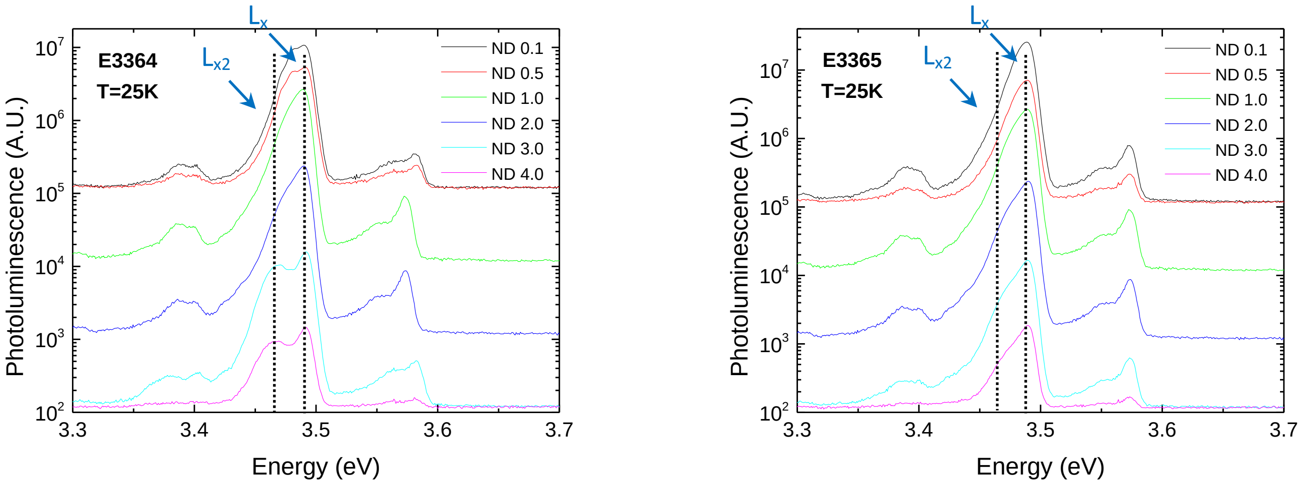

(a) **(b)**

Figure 9.11 PL versus energy at different values of excitation power attenuated by a series of Neutral Density (ND) filters for (a) E3364 and (b) E3365 samples at 25 K (dotted lines shows L_x excitons).

9.3. A_x, B_x and C_x simulation based on Nextnano software

At this point, simulations for the verification of the excitonic transitions within the effective mass approximation and the 8x8 k.p perturbation theory were made by the use of the NextNano software designed by Stefan Birner [10]. This program combines all the necessary physics that is needed for our simulations and gives very good results compared to similar works that can be found elsewhere. By declaring all the necessary parameters in an input file, Nextnano is able to perform all the calculations and give an output file with the results. For the proper heterostructure simulation, we had to create our structure in the input file of the software, according to the program's demands, and make all the proper corrections needed to the material parameters that were predefined in the software files.

In the calculations, our membrane structure had a total thickness 234.1 nm, similar to the E3365 XRD results, with all the layers grown pseudomorphically on c-GaN. The next step was to understand the piezoelectric and spontaneous polarization effects in the heterostructure, arising by strain and the lack of inversion symmetry in nitride structures. It is well known in literature [12; 34] that devices made by III-V nitrides exhibit large piezoelectric and spontaneous polarization in each layer in contrast to other materials, therefore it was important to take them into consideration. Based on the calculations, it was found that the built-in field acting on the wells is around 350 kV/cm. The QCSE effect, which is dependent on this field, induces in turn a red-shift to the exciton states, which cannot be omitted.

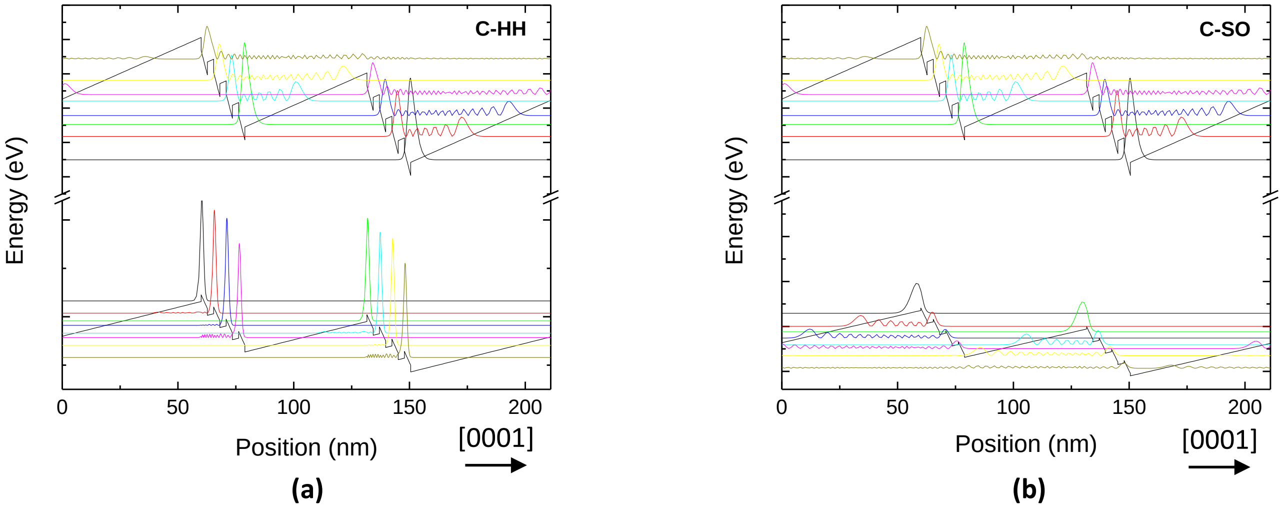

(a) **(b)**

Figure 9.12 Simulation results of the probability distribution $|\Psi|^2$ in our heterostructure for (a) conduction - heavy hole bands and (b) conduction - split off bands for 5 % Al concentration and T = 25 K within the effective mass approximation. The thicknesses of each layer are similar to the design membrane structure.

In the beginning, some first trials of the above structure were made within the effective mass model for the full 8 QW structure, but we realized that too much of computer power was needed to perform the exciton corrections and that a really large number of transitions needed to fill up all the QWs in the structure. The higher probability distributions ($|\Psi|^2$) in the quantum wells corresponding to ground states of conduction, heavy-hole and split-off bands in each quantum well are presented in Figure 9.12 (light-hole probabilities are very similar to heavy-hole and are not shown here).

To reduce computer time, we used 1 QW (Fig. 9.13) having same polarization-induced internal fields acting on the QW and the barrier as in the full structure by keeping the same width of the well (L_{qw} = 2.7 nm), and taking the respective barrier thickness as $L_{barrier}$ = 8.5 nm. Within the k.p model (Figure 9.13 (b)), the quantum states in the valence bands are mixed and not pure, due to the perturbation with a two-spin degeneracy. Al concentration (x) was kept constant at 5 % with the temperature defined at 25 K in the graphs. Simulations by varying temperature were performed in comparison to the experimental results for the E3365 sample. The Varshni parameters that were used in the Nextnano input file were extracted from the PL peak data of the same sample, while the exciton binding energies where calculated within the effective mass model and then subtracted from the transition energies that were found from both theories.

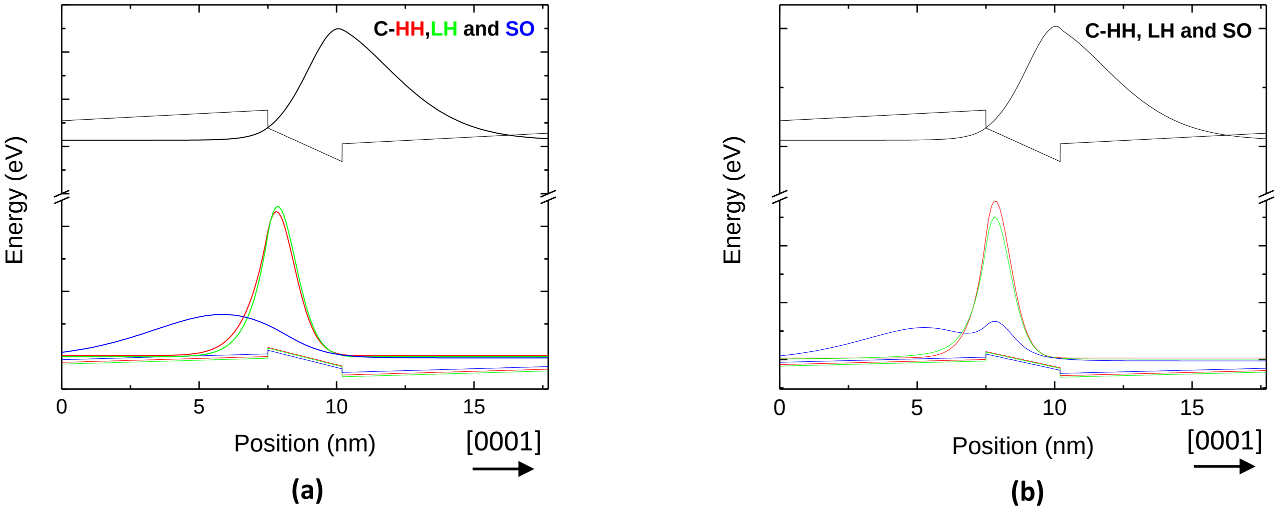

Figure 9.13 Simulation results of the probability distribution $|\Psi|^2$ for 1 QW analogue with 5 % Al concentration and T = 25 K within (a) the effective mass approximation and (b) 8x8 k.p perturbation model. The black-colored names HH, LH and SO of the valence bands declare that the states are not pure but mixed due to perturbation. The single QW was calculated based on the acting field inside the wells similar to the 8 QW structure.

In the next plot (Figure 9.14) are shown the experimental values of L_x, A_x and B_x exciton energies obtained from analysis of the PL and RFL spectra versus temperature. L_x denotes the localized excitons that create the S-shape of the PL peak vs T at low temperatures. Regarding the quantum well free exciton states, it was found that the PL maximum has a small shift (3 - 4 meV) at higher energies compared to the values of A_x exciton above 120 K as determined by RFL. As visible, this shift is attributed to the mixing and contribution from the B_x exciton. C_x exciton, as stated before, is not seen and hence is not shown in the plot. The experimental energy difference between A_x and B_x is around 13.5 meV. A_x, B_x and C_x were simulated with the Nextnano software for the same temperature region by using the extracted Varshni parameters from the PL peak maximum of E3365.

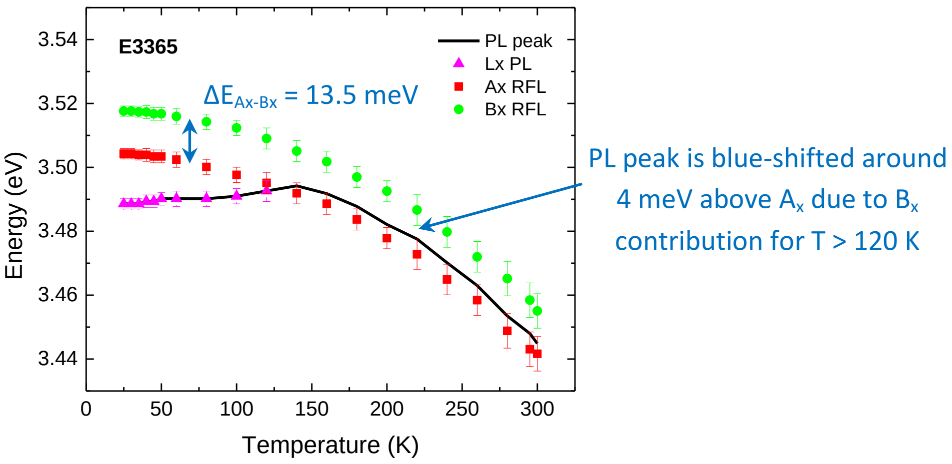

PL peak is blue-shifted around 4 meV above A_x due to B_x contribution for T > 120 K

Figure 9.14 Energy versus temperature of the experimental L_x, A_x and B_x excitonic states with the corresponding PL peak of E3365.

To continue, in Figure 9.15 (a) are compared the simulated data based on the effective mass model with the corresponding PL peak of the E3365 sample, while in Figure 9.15 (b) are outlined the simulated data based on the 8x8 k.p perturbation theory. Exciton binding energies were taken into account in both graphs. The simulated data of A_x with k.p are shifted 5 meV to lower energy than the PL peak data of E3365 sample. The energy difference between A_x and B_x from simulations within the eff. mass was 14.7 meV, while with k.p model was found to be 15.7 meV. On the other hand, ΔE of B_x and C_x was 9.2 meV and 17 meV, respectively. As can be seen, the C_x that resulted within the k.p model is located at higher energy than the corresponding values from the effective mass model. To sum up, the simulations are found to be in a good agreement with the PL values for the A_x and B_x excitons.

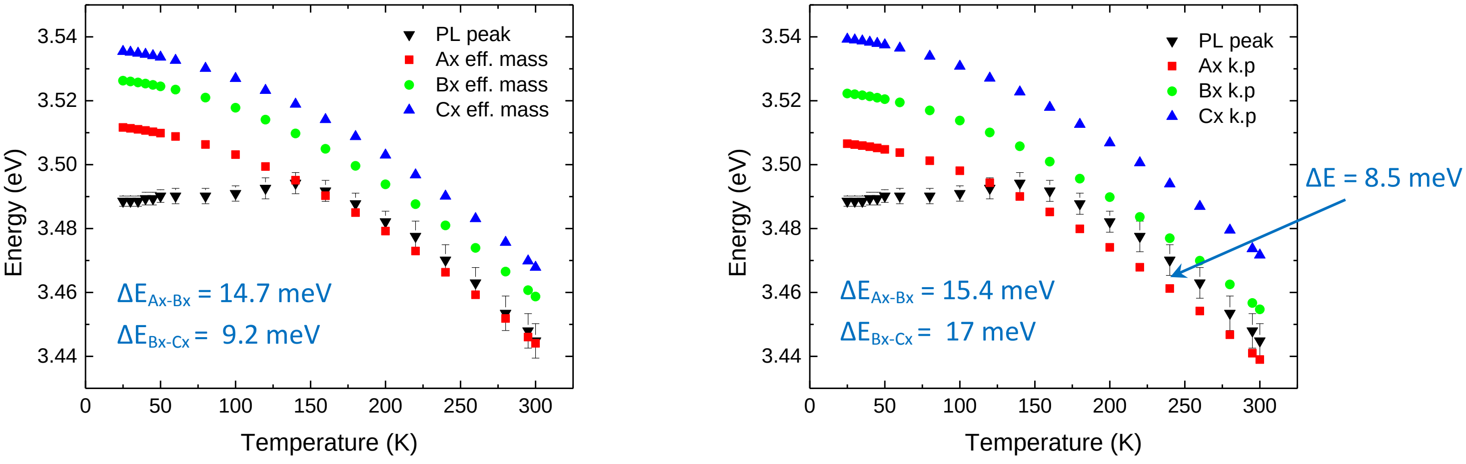

(a) **(b)**

Figure 9.15 Energy versus temperature of the A_x, B_x and C_x excitonic states based on the simulation results for 1 QW analogue with 5 % Al-content (a) within the effective mass and (b) within the 8x8 k.p.

10. Reactive Ion and Photo-electrochemical Etching

10.1. Design of various square and cylindrical-sized mesas

The next step was to perform standard lithographic process and Reactive Ion Etching (RIE) to create mesas on the surface of various dimensions and around 1 μm height. RIE is a dry etching technique, which uses chemically reactive plasma generated by an rf-electromagnetic field under low pressure to remove surface material on wafers. For this purpose, a pre-patterned metallic mask was used to protect the desired regions and selectively etch the non-desired areas. This was done so as to expose laterally the InGaN sacrificial layer for selective PEC etching. As we will see, the active area of the electrochemical cell is much larger than the fabricated squared mesas, so that it can successfully etch various dimensions simultaneously.

In Figure 10.1 (a), an illustration is presented of the squared mesas, and in Figure 10.1 (b), an optical image of one period of the pattern after RIE process. The area of the squared mesas varied from 45 x 45 to 155 x 155 μm^2. Similarly, in Figure 10.2 (a), an illustration is given of the cylindrical mesas, while in Figure 10.2 (b) an optical image of one period of the patterned mesas after RIE. The numbers in the second case denote the diameter of the above circular mesas, which range from 1 μm up to 40 μm. As seen at the optical image (Fig. 10.2 (b)), mesas smaller than 4 μm could not be observed, implying that a new mask should be used in the future.

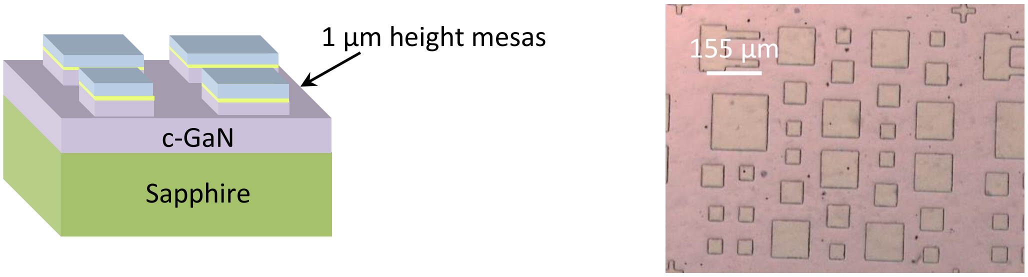

(a) (b)

Figure 10.1 (a) Illustration showing the creation of 1 μm high square mesas and (b) one period of the pattern taken by an optical microscope after processing with Reactive Ion Etching (RIE) technique.

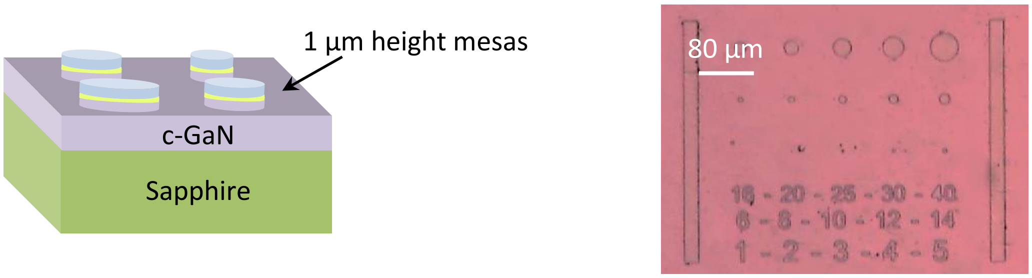

(a) (b)

Figure 10.2 (a) Illustration showing the creation of 1 μm high cylindrical mesas and (b) one period of the pattern taken by an optical microscope after processing with Reactive Ion Etching (RIE) technique.

10.2. Fabrication of free-standing membranes and standing microdisks

In the case of free standing membranes, in order to be able to peel off the desired structure from the samples, the photo-electrochemical (PEC) wet etching was used to make 200-nm thick membranes that could be later transferred and sandwiched between DBR mirrors. The highly selective etching of c-$In_xGa_{1-x}N$ sacrificial layer was done in lateral direction on the previously mentioned pre-patterned samples into a grid of mesas of various sizes. With this method, one can succeed very smooth and high quality membranes by adjusting the voltage, etching time and laser power for a constant electrolyte concentration. Here, the electrolyte solution remained constant at all times and consisted of 0.0004 M KOH concentration diluted in deionized water similar to reference [88].

After preparing the electrolyte solution, it was placed in an electrochemical cell, while the samples were attached on the backside. The active area of the pinhole was 0.78 mm^2, implying that several tens of mesas can be etched in a single run. The application of the reverse bias was done through a Platinum (Pt) electrode dipped in the solution, which was used as a cathode, and an Indium (In) contact on the top side of the samples, which acts as an anode. All the etchings were carried out at ambient conditions with a computer-controlled system, as described earlier. To ensure the selectivity of the PEC etching, a 405 nm diode laser source is used for the excitation of the carriers in the $In_xGa_{1-x}N$ layer, which corresponds to an energy well below the energy gap (E_g) of GaN.

For the square mesas, an ND 0.3 filter was used to reduce the maximum output power of the diode laser. The total power of the laser beam after passing the cell and the filter was measured to be 3.5 mW. By using low laser powers, less photo-carriers are generated and it is easier to control the whole process. Apart from that, temperature effects may arise from high laser powers, thus, they should be taken into account in every case. From the work of R. Jayaprakash et al. [88], very smooth membranes can be obtained by using low etching rates and high extents in time, therefore we tried to follow this route. A major difference in our samples is that we did not use Si-doped GaN templates but non-intentionally doped GaN grown on Sapphire.

As explained in literature, during PEC process holes at the surface of the semiconductor, in our case InGaN, combine with the OH^- of the electrolyte, thus causing oxidation of InGaN, with nitrogen and water as byproducts. The chemical reaction for oxide formation based on [88; 96] is the following

$$2InGaN + 6h^+ + 6OH^- \Rightarrow (In,Ga)_2O_3 + 3H_2O + N_2 \quad \text{(oxide formation)}$$

while the chemical reaction for the oxide dissolution is

$$(In,Ga)_2O_3 + 6OH^- \Rightarrow 2(In,Ga)O_3^{-3} + 3H_2O \quad \text{(oxide dissolution)}$$

Hence, after every etching a cleaning with deionized water has to take place to remove most of the residual oxides.

After performing some trial exposures, it was found that a good trade-off between voltage and etching time can be obtained by keeping the reverse bias constant at 3V and varying the etching time to about 40 minutes. Under these conditions, the three most promising characteristic times used for both samples were 2100, 2300 and 2500 sec. It should be noted that for higher voltages a bubbling effect can arise and lead to non-uniform exposure of the sample surfaces. On the other hand, for low voltages, time has to be extended. A characteristic I - t curve of the 2100 sec case is shown in Figure 10.3.

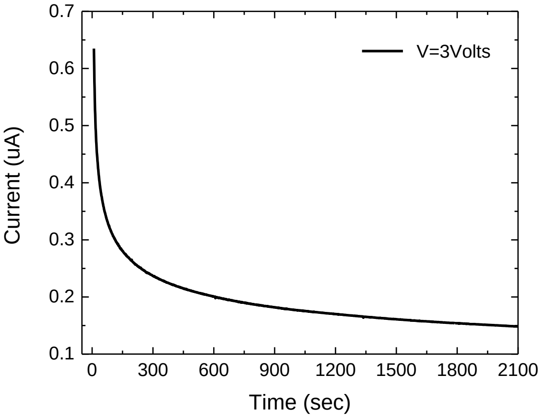

Figure 10.3 Current versus time for the 2100 sec square-membranes with reverse bias at 3 Volts in Photo-electrochemical etching (PEC).

Optical microscope images of the resulting regions after etching can be seen in Figure 10.4. The pink color of the membrane structures arises from scattering of the incident light. What was observed, between the two samples, is that E3364 exhibits more impurities in the surrounding spot area, than the E3365, probably due to residual oxides, since a small portion can still remain on the sample from undiluted oxides [88]. Especially for the 2300 sec case of E3364, it can be clearly seen that the region is covered with oxide residues around the spot and the etching of the membranes was not homogeneous as can be concluded from the different colorization of the membranes, while some of the membranes were damaged. For the 2500 time case of E3364, some membranes in the outer region have left away, probably after washing with deionized water, or they were fully destroyed. As regards the shorter etching time of 2100 sec, it is visible that it has more uniform colorization than the other two regions.

On the contrary, the 2100 sec spot of the E3365 sample exhibits very good visual results, while the other two areas, as it can be derived, they are not that uniform. As concerns the 2300 sec, the inset image shows that some good quality membranes can be found in the region. For the 2500 sec, we see again the loss of some membranes at the spot edges similarly to E3364. It is worth noting here that the fluctuations and the percentage of Indium concentration played of course an important role between the two samples. A significant drawback is that all spots have a small “burning” in the center. Therefore, lower excitation power than the ~ 3.5 mW should have been used instead. The corresponding time extent should be increased for the same conditions due to their linearity.

Finally, it has been found that similar etching conditions between the two devices can have slightly different results. From the previous analysis, the E3365 sample proved to have better etching results for the given parameters. The time extent of 2100 seconds exhibited the best outcome for both samples based on the uniform colorization of the optical images. For a more trustworthy evaluation, optical images should be compared with other techniques such as SEM, but this would mean that we had to destroy the samples. Consequently, we proceeded without any further examination, since the next step was to transfer the membranes on other substrates.

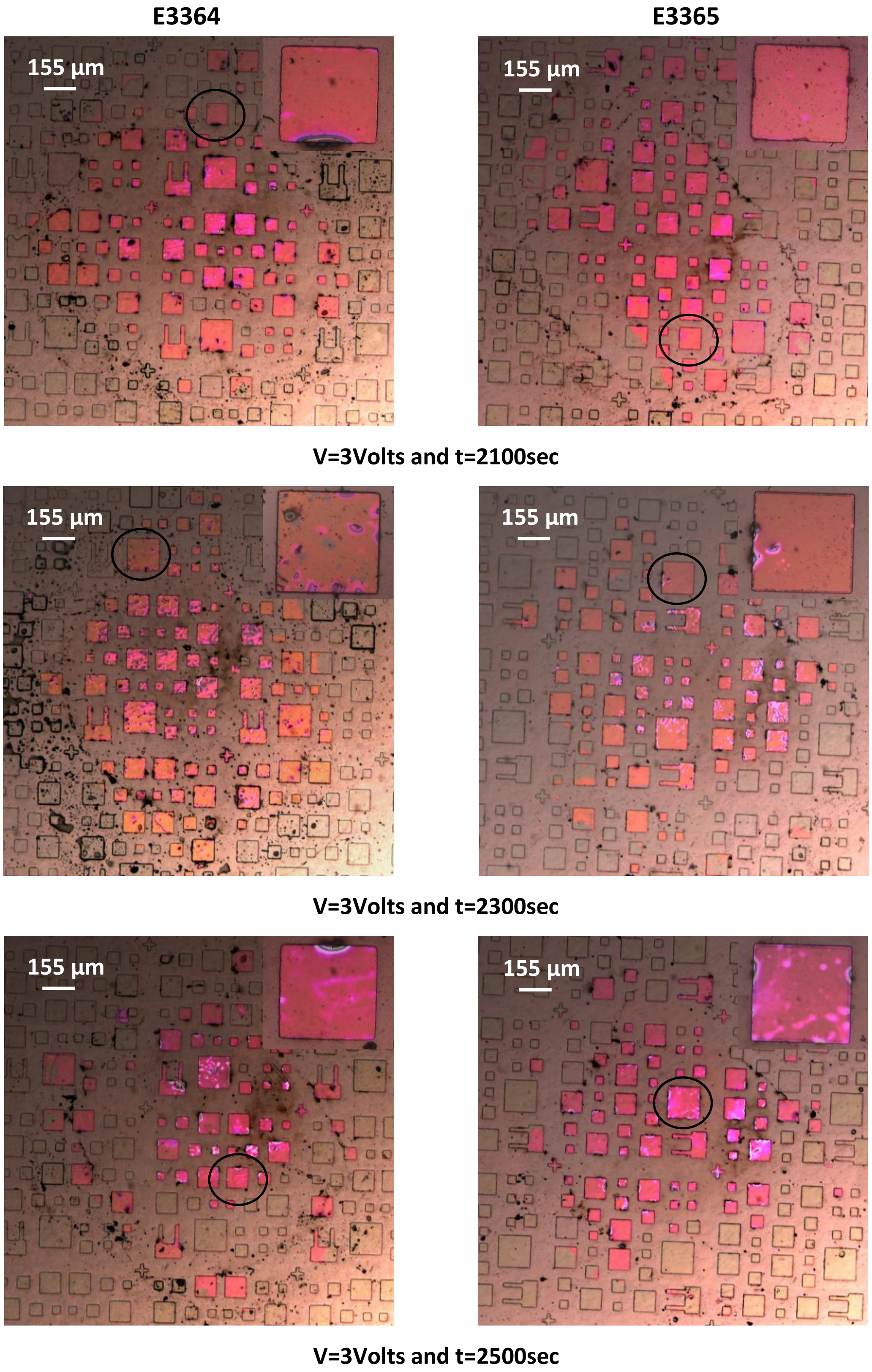

Figure 10.4 Optical microscope images of E3364 (left side) and E3365 (right side) after etching with constant reverse bias at 3 V and power at 3.5 mW for 2100, 2300 and 2500 seconds, respectively.

In the next image (Fig. 10.5), it is shown a region of etched membranes that have been moved from their mesas. Two of the three membranes pointed by the arrows seem to be moved, but be intact, while the third one seems to be broken. From this image, it was evaluated that the membranes could be used for transfer into other substrates for optical characterization. For this reason, some membranes were transferred on double polished Sapphire substrates and were excited again with the He - Cd laser by the same setup configuration. The outcome of the Photoluminescence is given in Figure 10.6, which shows the PL data of E3364 before and after the membrane fabrication. As presented the membrane is at slightly higher energies in comparison to the bulk. By making free-standing membranes, the difference was found to be around 15 meV for the E3354. Another important observation from this plot is that AlGaN is less visible in PL and that LO-phonon replicas are shifted to higher energies.

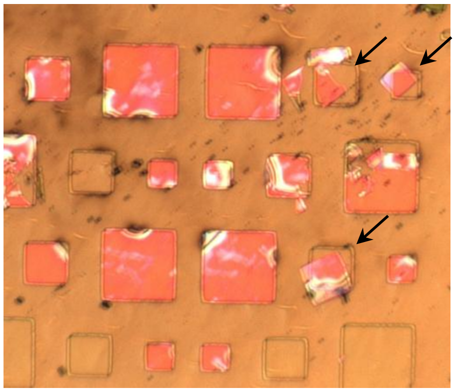

Figure 10.5 Optical microscope images of E3364 after etching indicating that some membranes have been moved from their original mesas (black arrows). As can be observed, one of the three pointed membranes has been broken in two pieces.

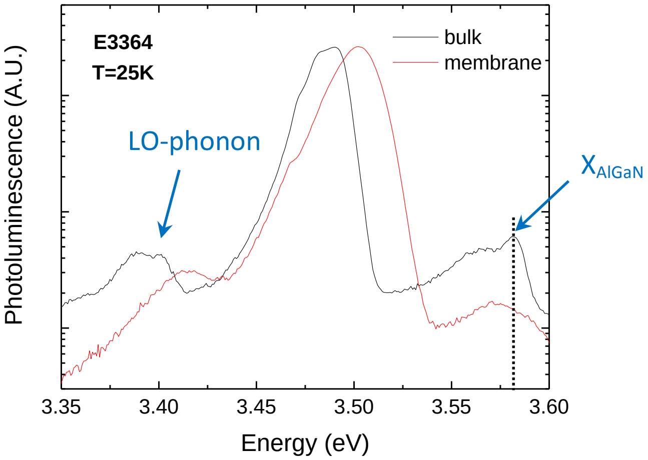

Figure 10.6 PL versus energy of bulk (black line) E3364 and membrane (red line) after PEC etching and transfer on to another substrate. AlGaN is less visible and the QW PL along with LO-phonon replicas are shifted to higher energies.

Concerning now the partial etching of the circular mesas, as the sizes were very different now, the laser power and the time extent had to be altered. On the other hand, the electrolyte concentration and cell active area remained the same. Since the circular mesas had smaller areas, less power and etching time were needed to etch them partially. For this reason, some estimates based on the square mesas results were performed in order to find the appropriate experimental etching rates. The resulted laser beam power was found to be around 100 μW. Therefore, a ND 2.0 filter with optical density 2 was used and the reduced laser power after the cell was at 67 μW.

For the microdisks only the E3364 structure was used with etching times at 20, 70 and 100 sec. Optical images of all the etched areas are illustrated in Figures 10.7 - 10.9. In the first case at 20 sec (Fig. 10.7), etching has been initialized but was not completed. Furthermore, it is visible that the disks are not homogeneously etched across the surface. At the time extent of 70 seconds (Fig. 10.8), the disks are observed to be a bit more etched than the previous timescale, but again non-uniformly. Microdisks from the last period of 100 sec (Fig. 10.9) show a uniform etching, such as the 25 μm disk that is shown on the right side. Nevertheless, further experiments have to be done for a more detailed description.

Since similar issues, having a non-homogeneous etching front as in membranes case, the problem of the microdisks was attributed to the non Si-doped GaN template, as less current density could be attributed to this problem. Previous work of Haberer and Tamboli et al. [3; 97] has shown that PEC along with electron beam lithography can be used for GaN microdisk structures with low roughness at the side-walls even for small diameter disks. As mentioned earlier, smaller disks are more intriguing as they exhibit fewer modes with increased intensities, in agreement with theoretical simulations.

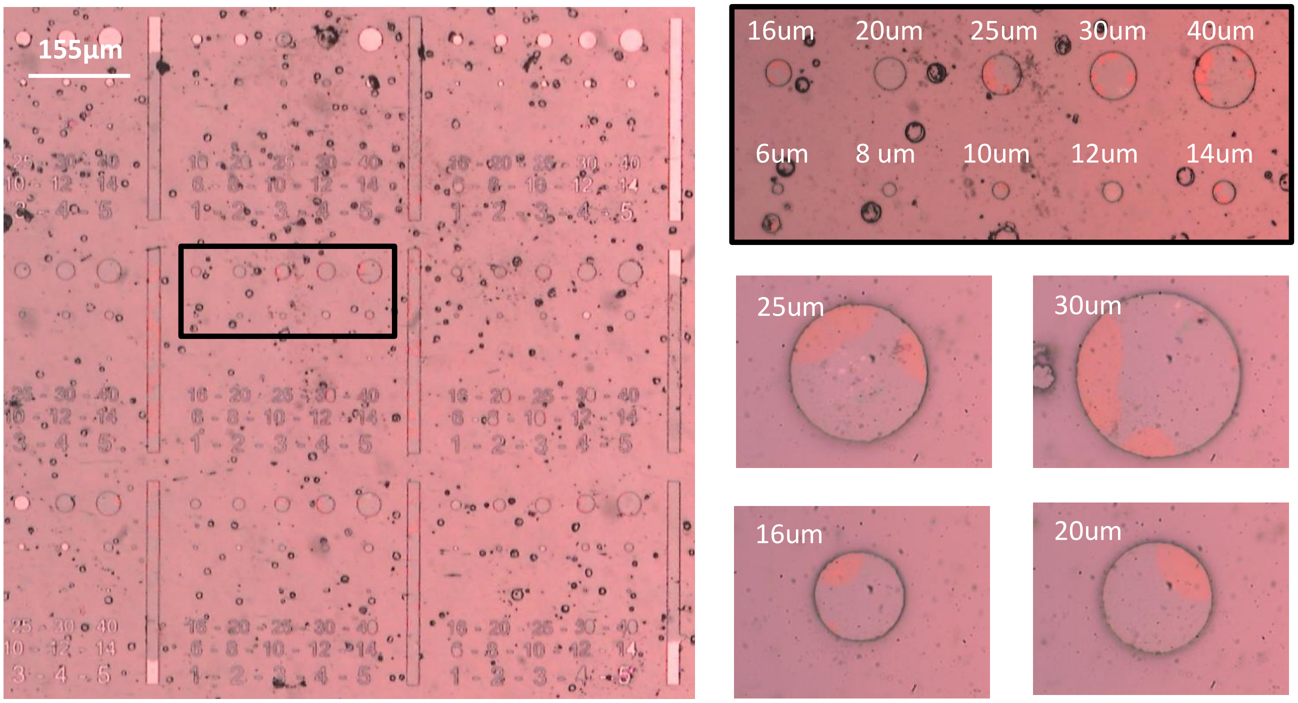

Figure 10.7 Optical microscope images of E3364 after etching with constant reverse bias at 3 V and laser power at 67 μW for 20 sec. The black rectangle denotes the enlarged region on the right, while the separate disks are from random areas.

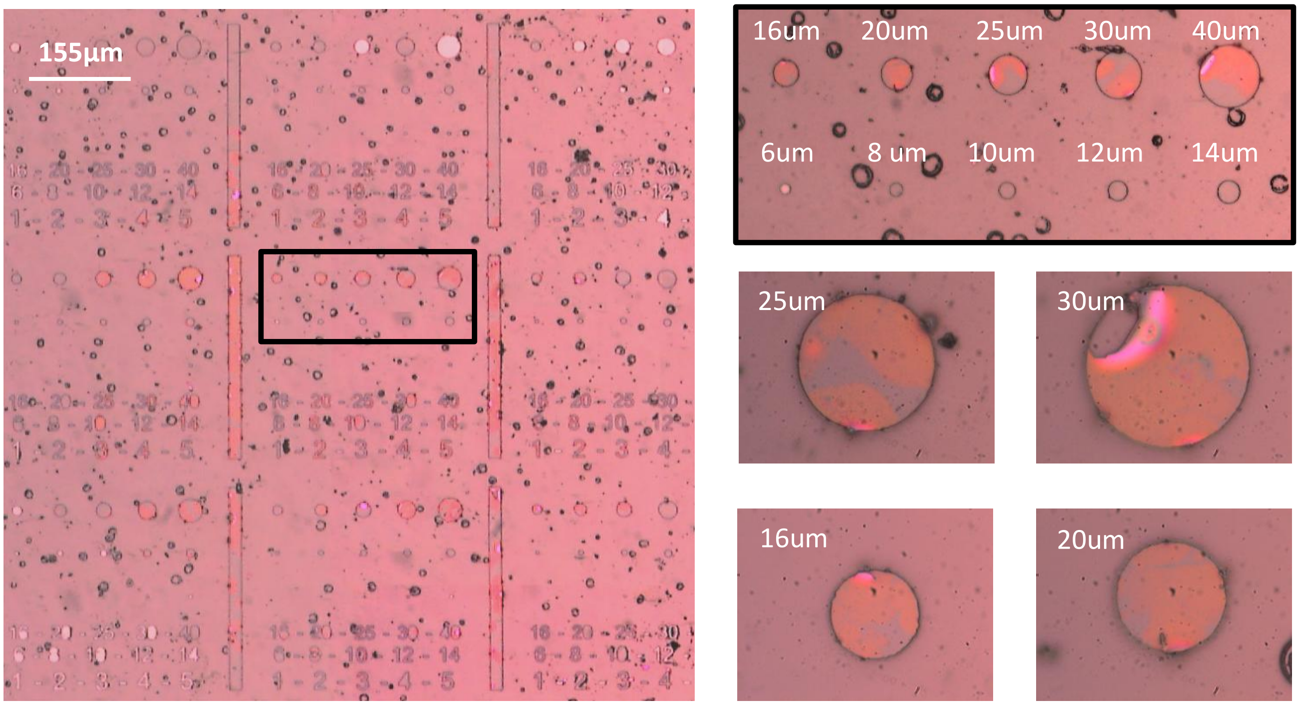

Figure 10.8 Optical microscope images of E3364 after etching with constant reverse bias at 3 V and laser power at 67 µW for 70 sec. The black rectangle denotes the enlarged region on the right, while the separate disks are from random areas.

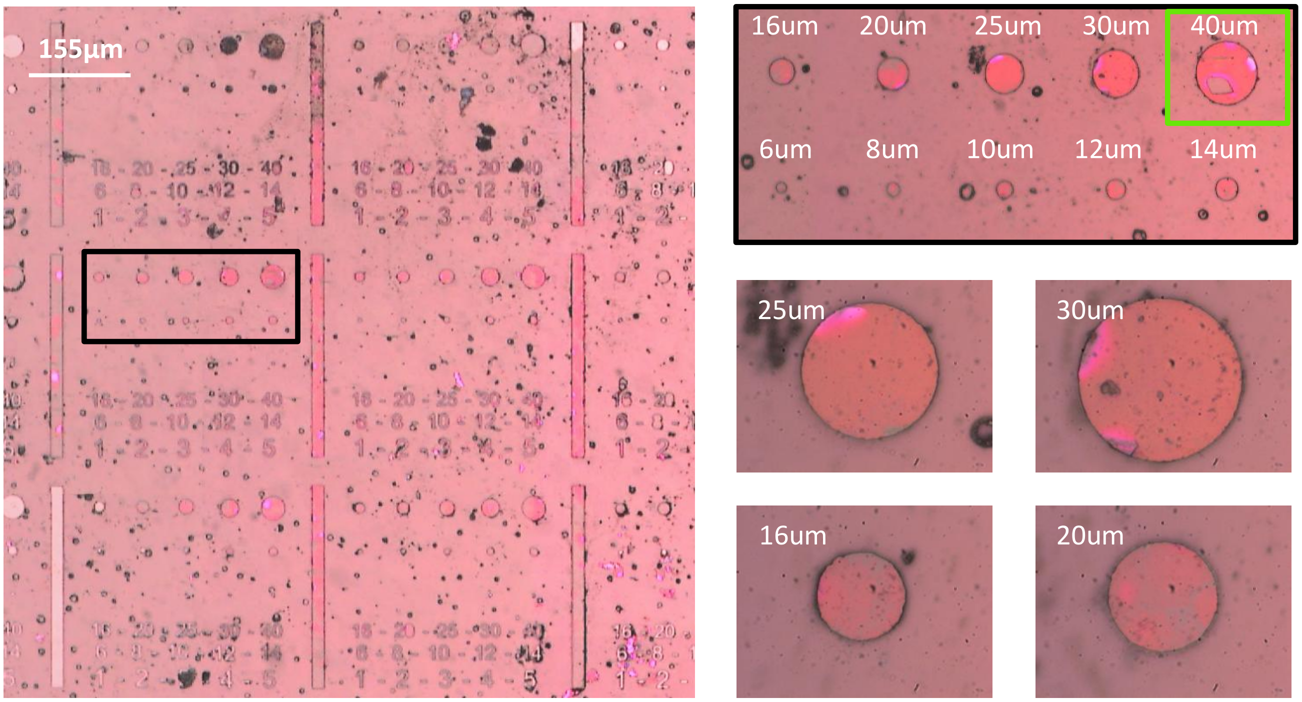

Figure 10.9 Optical microscope images of E3364 after etching with constant reverse bias at 3 V and laser power at 67 µW for 100 sec. The black rectangle denotes the enlarged region on the right, while the separate disks are from random areas. The 40 µm disk was analyzed also with SEM (green rectangle).

After taking some optical images of the fabricated microdisks, a JEOL JSM 7000F Field Emission SEM was used for a better evaluation of the results. Estimating that the most appropriate spot to check by SEM was that of 100 sec exposure time, we tried to observe the broken 40 μm disk shown in the inset of Figure 10.9. The resulting SEM images are shown in Figure 10.10. As can be seen in Figure 10.10 (b) at the edges of the broken area, etching has occurred, while there is a smooth surface under the lifted broken piece. In Figures 10.10 (c) - (d), are presented the side views of the disk. As can be observed, the InGaN layer has been etched at the edges and the microdisk tries to lift up. By taking a more careful look around the microdisk, it was found that it was etched around at most of the sides. It should be mentioned that this was the first trial in our group to etch microdisks. Clearly, further experiments are needed towards the improvement of this micro fabrication.

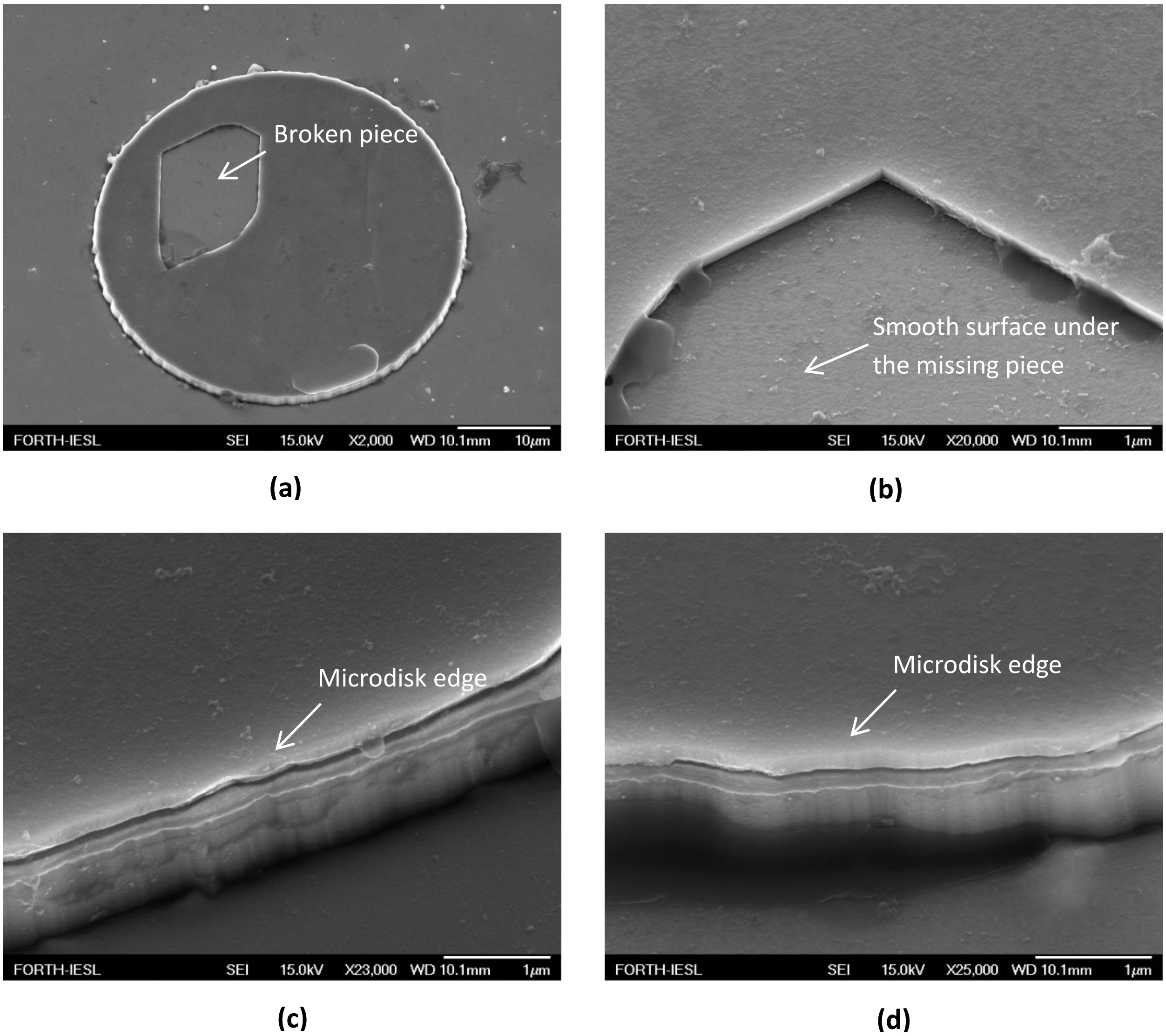

Figure 10.10 SEM images of a 40 μm diameter disk on E3364 sample after etching with constant reverse bias at 3 V and laser power at 67 μW for 100 sec (a) full disk, (b) zoom at the broken part, (c) and (d) side views.

11. Bottom DBR mirror grown on Sapphire

11.1. Characterization of bottom-DBR/Sapphire template

The growth of the bottom DBR of our microcavity was ordered to Helios Optics to make for us several samples on Sapphire (Al_2O_3) templates. The dielectrics that we decided to use were Silicon Dioxide (SiO_2) and Tantalum Pentoxide (Ta_2O_5), as low and high refractive index materials, respectively. In this case 11 alternating pairs were needed for reflectivity values of the stop-band region close to unity. The Reflectivity data were measured with the setup explained before and compared with simulations based on Transfer Matrix Method. In this method, every layer is simulated with a matrix and a total matrix of the structure can be obtained (see Appendix C).

The Sellmeier equations of the refractive indices, shown in Figure 11.1, were used as input parameters to the Matlab code for the bottom DBR mirror and were taken from reference [98]. These indices were calibrated based on the 360 nm wavelength at $n_{SiO2} = 1.5099$ and $n_{Ta2O5} = 2.0442$ to achieve the obtained values of Helios Optics Spectroscopic Ellipsometry (SE) measurements. By doing the math, one can find that the quarter wave thicknesses of the alternating layers should be $t_{theorSiO2} = 59.60$ nm and $t_{theorTa2O5} = 44.03$ nm. As in all cases, the growth thicknesses might have some deviations from the expected values. Therefore, the theoretical predicted values will be altered and the resulting stop-band will be shifted accordingly. A comparison has to be done with the experimental results in any case for this reason.

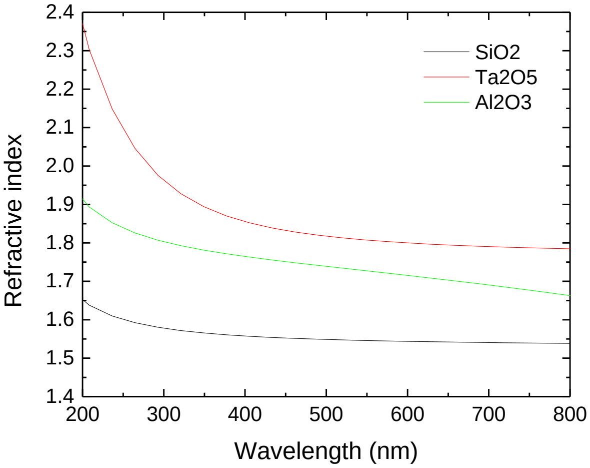

Figure 11.1 Refractive index versus wavelength of SiO_2, Ta_2O_5 and Al_2O_3 dielectric materials [98].

In Figure 11.2, is given an illustration of the bottom-DBR/Sapphire structure along with the corresponding Reflectivity spectrum obtained from experimental results, and a comparison with simulated data. The obtained output data of the simulation showed that the thicknesses of the SiO_2 and Ta_2O_5 layers were $t_{experSiO2} = 66.5 \pm 0.5$ nm and $t_{experTa2O5} = 42 \pm 0.5$ nm, respectively, with a center of the stop-band at $\lambda_{exper} \sim 374.3$ nm. The ideal stop-band center, which was simulated based on nominal thicknesses, should be at $\lambda_{optim} = 365$ nm, as can be observed from the green line in Figure 11.2 (b). This template, as we will see later, was used for the transfer of the membranes.

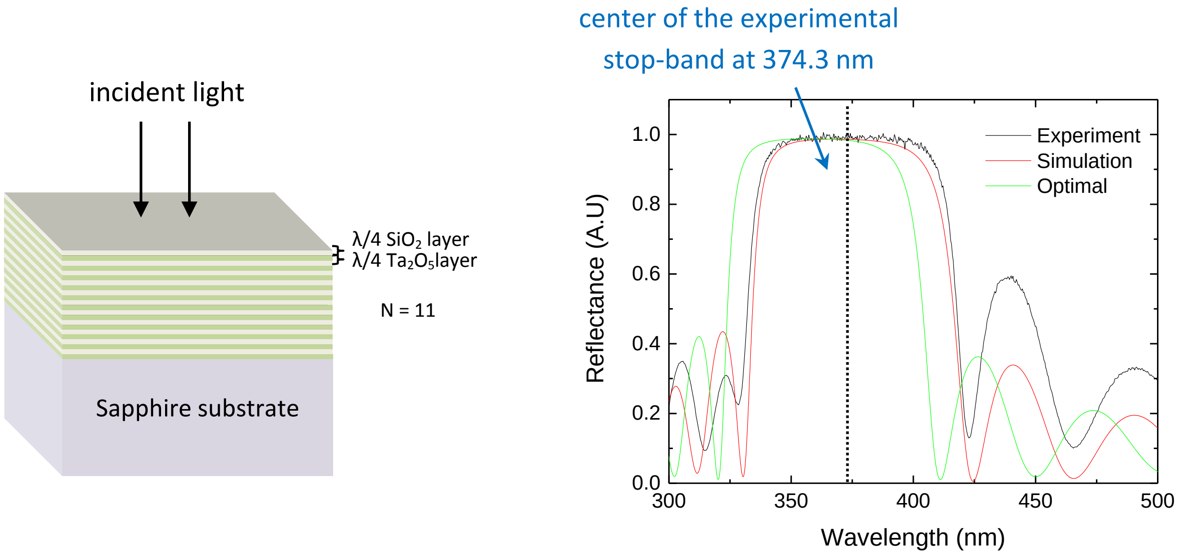

(a) **(b)**

Figure 11.2 (a) Illustration showing the 11 period alternating pairs of the bottom-DBR layers on Sapphire substrate and (b) Reflectance of the DBR sample in comparison to the Matlab code simulations.

11.2. Transfer of membranes on bottom-DBR/Sapphire templates

Membranes at this point were ready for transfer on other substrates. As they were around 200 nm thick with sizes in the order of 45 - 155 μm, special care had to be taken. For the transfer, the previously mentioned Sapphire substrates, with the 11 pairs of SiO_2/Ta_2O_5 deposited on them, were used as bottom DBRs. The transfer of the membranes was done by a wet method developed in our group, which takes advantage of Van der Waals interactions. After membranes were successfully transferred (Fig. 11.3), the plan was to deposit another DBR on top for the completion of the microcavity structure. Bear in mind that for a polariton structure, a high Quality Factor (Q-factor) is needed for the improved performance of our devices and every step in this process is of paramount importance.

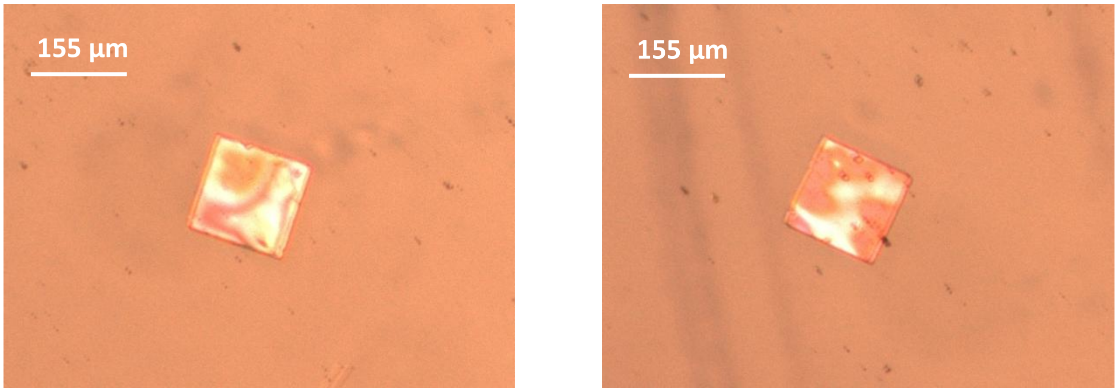

(a) **(b)**

Figure 11.3 Optical images of 155 μm membranes after their transfer on bottom-DBR/Sapphire substrates ready for a top-DBR deposition.

The Photoluminescence of the E3364 membranes with the corresponding as-grown data at 25 K and 295 K are presented in the Figure 11.4. There is a visible energy difference of around 10 meV between the membranes and the as-grown structure with the latter being at lower energies. This can be easily justified due to the strain effect as discussed in theory. An expected shift at higher energies was expected for the free standing membranes due to strain imposed to the wells by the barriers. Nevertheless, small variations in energy among membranes of the same sample exist but they are small. Similar optical characteristics were obtained also for the E3365 sample, as can be seen in Figure 11.5, with energy variations again at the same levels. What is more, in the case of the membranes there is a larger FWHM in contradiction to the as-grown structures, which exhibit finer peaks especially at higher temperatures. This increased linewidth is possible due to strain inhomogeneities.

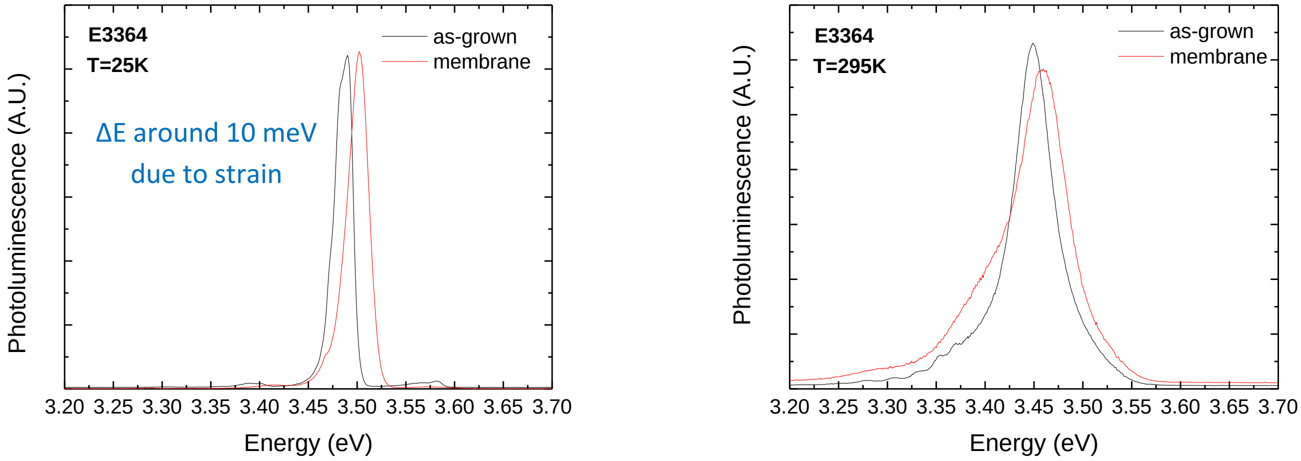

Figure 11.4 Photoluminescence of bulk E3364 (black line) before etching and free-standing membrane (red line) after transferring it on a bottom-DBR/Sapphire substrate (a) T = 25 K and (b) T = 295 K.

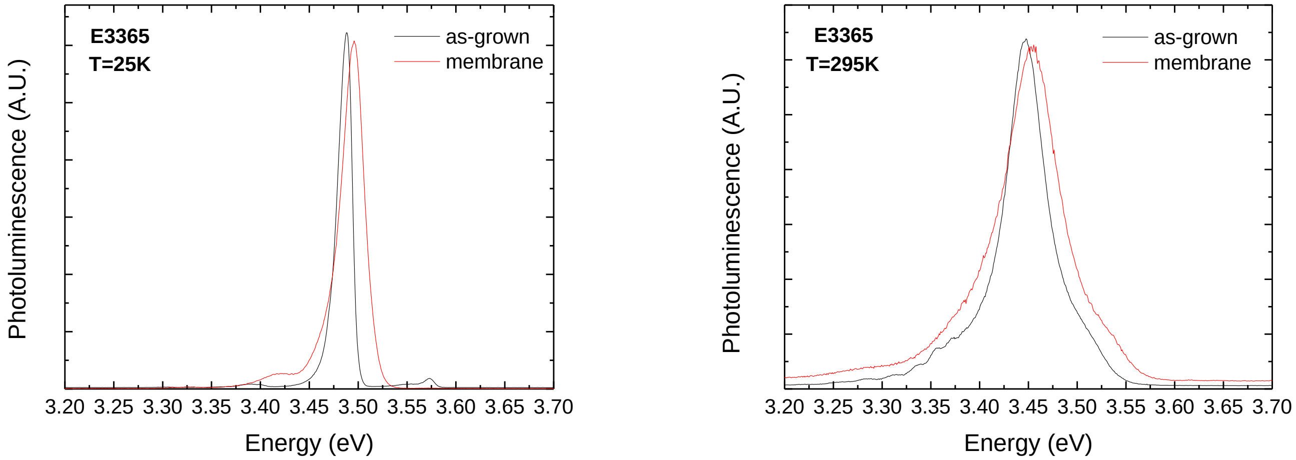

Figure 11.5 Photoluminescence of bulk E3365 (black line) before etching and free-standing membrane (red line) after transferring it on a bottom-DBR/Sapphire substrate (a) T = 25 K and (b) T = 295 K.

To continue, Reflectance data of membranes on top of the bottom-DBR were acquired as plotted in Figure 11.6 for three E3364 membranes. The Q-factor based on the three membranes was in the range of 23 – 34. These values are considered very low is respect to previous samples that we had in the past. There is a discussion in the last chapter about the low Q-factor. Maybe it is decreased due to some inclination of the membranes due to oxide residues or broken parts from other membranes. The range of the cavity mode was found to be between 358 – 365 nm (shown by the black dashed lines) for the previous membranes. In addition, in Figure 11.7 are plotted the Reflectance with the corresponding Photoluminescence of the membrane 3 (Figure 11.6) for comparison. As regards A_x and B_x, they can be clearly distinguished in the RFL plot. The reflectance data in the two last graphs are not normalized in respect to the white source lamp.

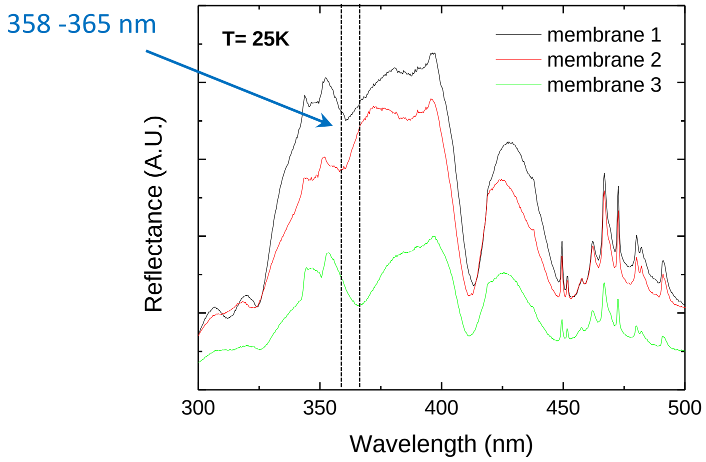

Figure 11.6 Reflectance of E3364 three different membranes after transferring them on a bottom-DBR/Sapphire substrate. The black dashed lines indicate the variation of the cavity mode among the membranes.

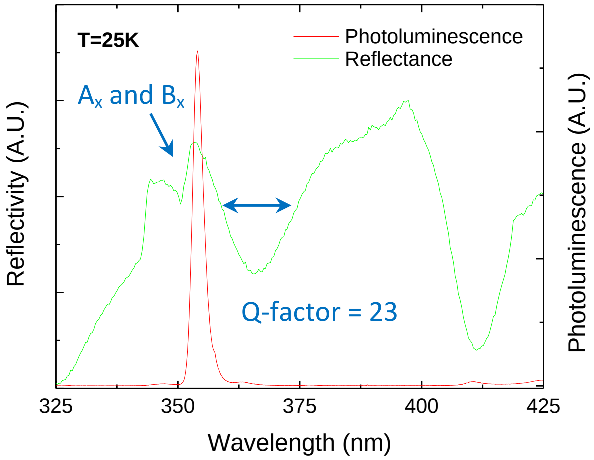

Figure 11.7 Reflectance and Photoluminescence of membrane 3 of the E3364 sample after transferring it on a bottom-DBR/Sapphire substrate.

12. Top DBR mirror growth on the transferred membranes

12.1. Top-DBR grown by rf-sputtering

For the top DBR, an initial idea was to use the sputtering method, as it has been proved a fast growing technique. In order to check the consistency to our case, we got 4 different samples from Grenoble grown by this method for characterization. The first sample was a Silicon substrate with 10 periods of Silicon Dioxide (SiO_2)/Silicon Nitride (Si_3N_4) alternating pairs and the other three samples were a Si sample with its native SiO_2 oxide and rf-sputtered SiO_2 and Si_3N_4 layer on Si substrates. The last three samples were characterized by the SE method in our lab to extract the wavelength dependence of the refractive indices of the two materials and to measure the exact thickness of the SiO_2 and Si_3N_4 layers.

The above thicknesses measured to be $t_{nativeSiO2} = 1.63 \pm 0.02$ nm, $t_{sputtSiO2} = 192.60 \pm 0.30$ nm and $t_{sputtSi3N4} = 197.80 \pm 1.00$ nm, respectively. The extracted data of the refractive indices of the two dielectric materials were simulated with the Sellmeier equation with the aid of the OriginPro 9 software to acquire the equation parameters, which were later used in the Matlab code for the Reflectivity simulation. A similar approach would be of course to use the Cauchy empirical equation for modelling dispersion. The extracted wavelength dependence is presented in Figure 12.1 (a) for SiO_2 and Si_3N_4, while in Figure 12.1 (b) is shown the Si dispersion relation taken from reference [99].

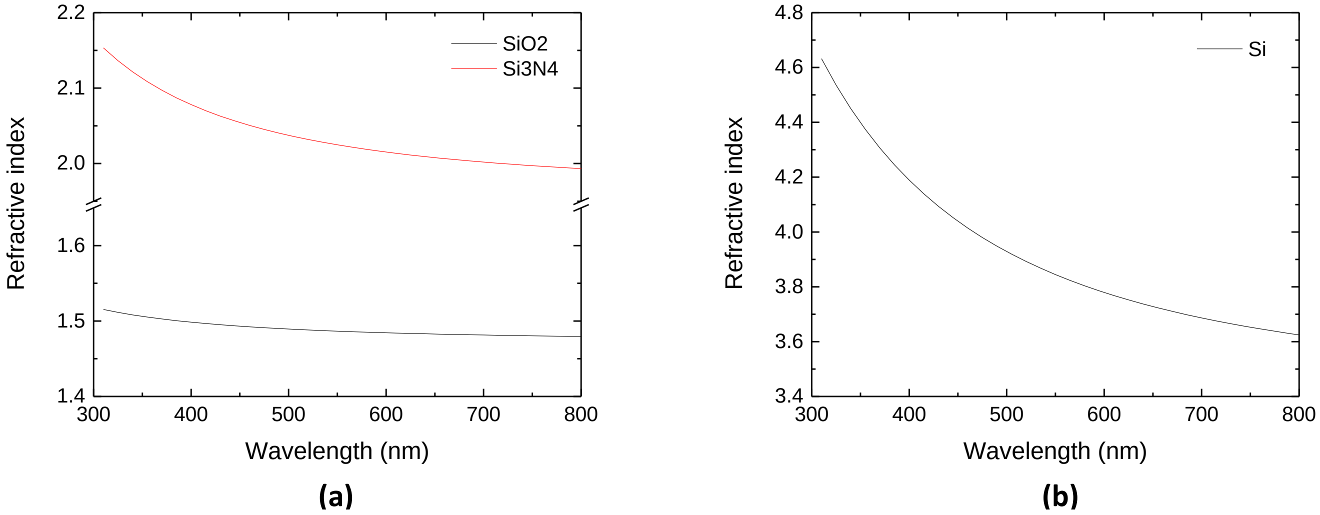

Figure 12.1 Refractive index versus wavelength of (a) rf-sputtered SiO_2 and Si_3N_4 based on SE measurements in our lab and (b) Si taken from reference [99].

The parameters of the refractive indices and the layer thicknesses were then used in the Reflectivity simulation for the top-DBR and compared with the real Reflectivity data of the 10 periods of SiO_2/Si3N_4 alternating pairs on a Silicon substrate. The reason for using some testing samples was to check the cohesion of our theoretical predictions and be able to apply any changes before the final sputtering on the membrane samples. From the acquired data, only the central spot of the DBR/Si sample is presented (Fig. 12.2) along with the corresponding simulation spectra. According to the simulation data, the thicknesses of the two layers are $t_{sputtSiO2}$ = 62.3 ± 0.5 nm and $t_{sputtSi3N4}$ = 44 ± 0.5 nm, while the center of the band was at λ_{exper} ~ 386.1 nm. Furthermore, the oscillating side-lobes were found to follow sufficiently well the experimental ones.

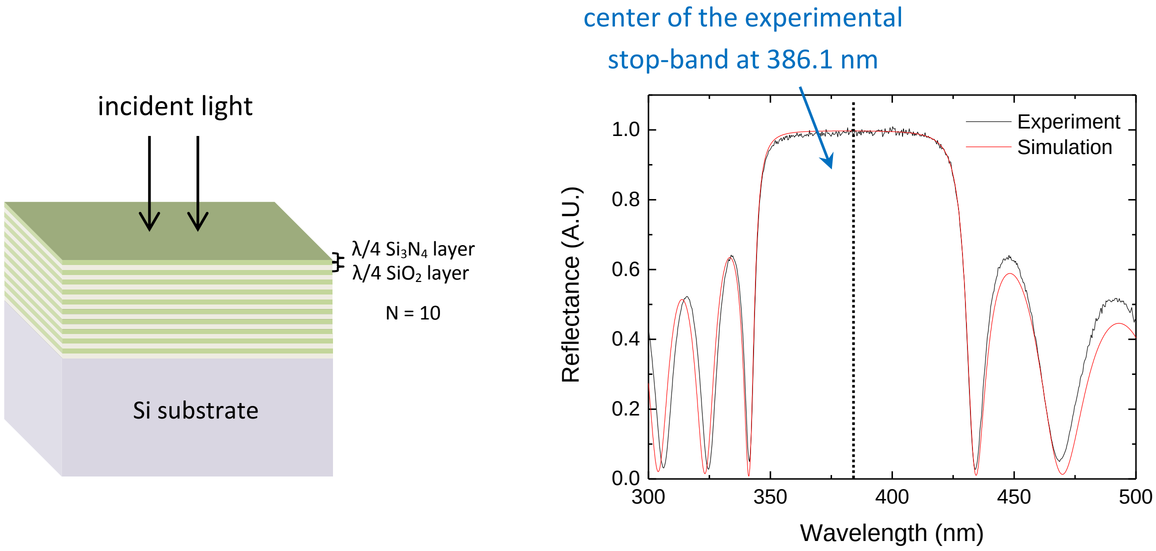

(a)

(b)

Figure 12.2 (a) Illustration showing the 10 period alternating pairs of the top-DBR mirror on Si substrate and (b) experimental data of Reflectance in comparison to the simulation data for the top-DBR mirror.

As the sputtering method gave a good DBR on Si, we adjusted all the necessary parameters based on the trial run to fabricate a DBR mirror centered at 365 nm. For the final run, 4 pieces with a few membranes on them were sent in Grenoble for a top-DBR sputtering of 10 periods of SiO_2/Si3N_4 alternating pairs. All the samples were attached on a huge double polished Sapphire piece with silver paste (not shown here). This was done for 2 reasons, the first was for mechanical stability, since they had to be sent in France, and the second was that after sputtering, we could characterize the top-DBR mirror on it with reflectance.

To move on, according to experimental data fitting displayed in Figure 12.3, from a central spot on the newly deposited DBR/Sapphire, the thicknesses of the dielectric materials were $t_{sputtSiO2}$ = 61.5 ± 0.5 nm and $t_{sputtSi3N4}$ = 42.2 ± 0.5 nm. As a result, the center of the DBR mirror was located at 365.8 nm, which is ideally close to the ideal value of 365 nm. Here, the fitting of the side-lobes is not as precise as the one on Silicon substrate, but is in a very good approximation. Therefore, we adopted again the values from reference [98] and did not proceed to further analysis of the Sapphire refractive index.

The next step at this point was to examine the effect of the top-DBR mirror stop-band region to the full microcavity structure. To do so, a simulation of the reflectivity spectrum for the full cavity was performed by using the theoretical thicknesses of the membrane layers in the Matlab code and the resulting data are placed in Figure 12.4. The wavelength value of the cavity mode based on the nominal value of membrane thickness was found to be at λ_c = 369.05 nm. As will be shown later, the overall membrane thickness was deviated from the nominal value. Therefore, this can move the cavity mode at higher or lower wavelengths accordingly. A simulation analysis was also performed for this reason.

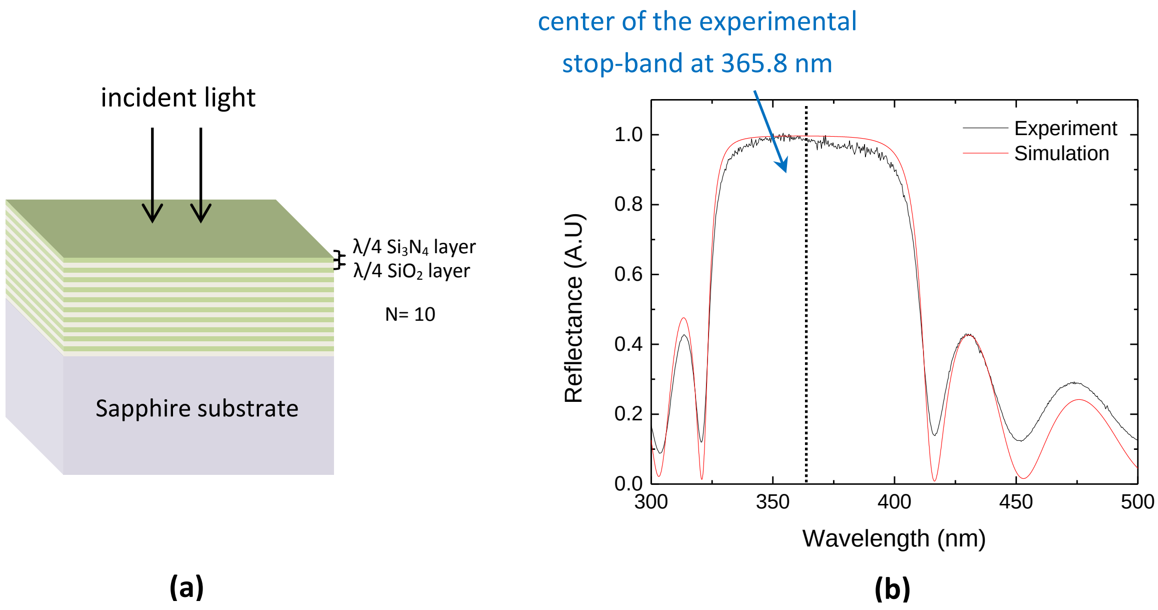

Figure 12.3 (a) Illustration showing the 10 period alternating pairs of the top-DBR mirror on Sapphire substrate and (b) experimental data of Reflectance in comparison to simulation data for the top-DBR.

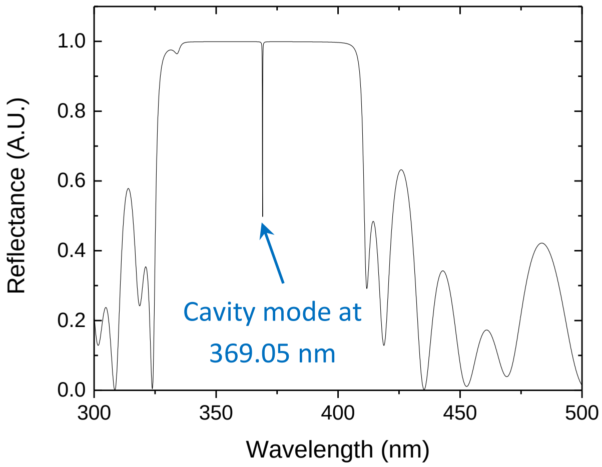

Figure 12.4 Full microcavity reflectance simulation by using the designed thicknesses for the membrane layers, while the top and bottom DBR thicknesses were based on the previous simulations. The cavity mode was indicated at λ_c = 369.05 nm.

After completing Reflectivity measurements, the samples were observed in the optical microscope and it was found that all of the membranes were cracked and in some cases they were completely destroyed or have moved from their position. Since it was difficult to find a physical explanation for their damage, it was attributed to mistreatment at their transfer to France. On the other hand, sputtering method was not considered to be able to destroy them, although it is known to alter their optical propertied. Two optical images of membranes from different pieces are presented in Figure 12.5. All the previous samples were tested with imaging mode of the PL setup, but neither cavity mode nor strong-coupling were observed. After that, instead of losing time to figure out what was the problem of the previous fabrication, it was decided that a more accurate method should be utilized to deposit our dielectric materials.

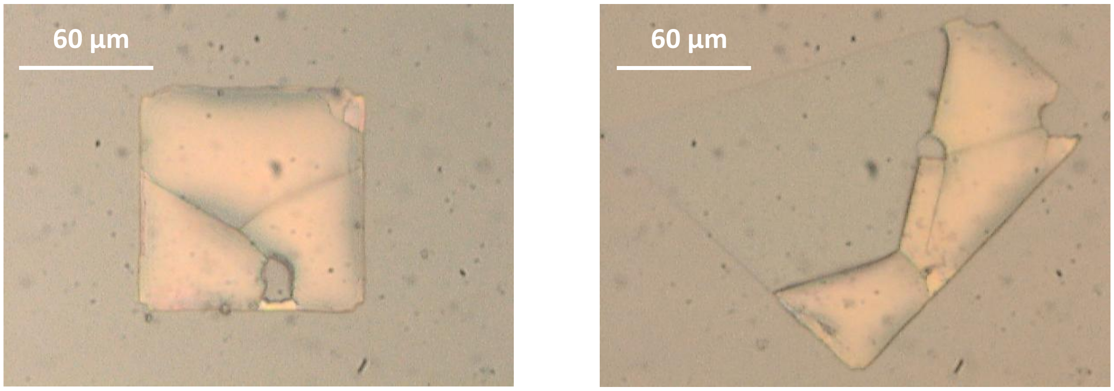

Figure 12.5 Optical microscope images of the damaged membranes after the final top-DBR sputtering.

12.2. Top-DBR grown by e-gun deposition

To proceed, e-gun deposition was thought to be a better adapted technique for the fabrication of the top-DBR mirror. Consequently, some membranes were transferred again on bottom-DBR/Sapphire substrates and were sent to Grenoble. Before doing any final deposition, we also asked for some test samples of the two dielectrics on Si substrates for SE characterization. The materials employed at this time were SiO_2 and Ta_2O_5 similar to the bottom mirror and the resulted refractive indices are shown in Figure 12.6. The surface roughnesses (rms), measured by a Multimode AFM Nanoscope IIIA in our group, were 0.7 nm and 1.2 nm, respectively, in an area of 4 µm^2.

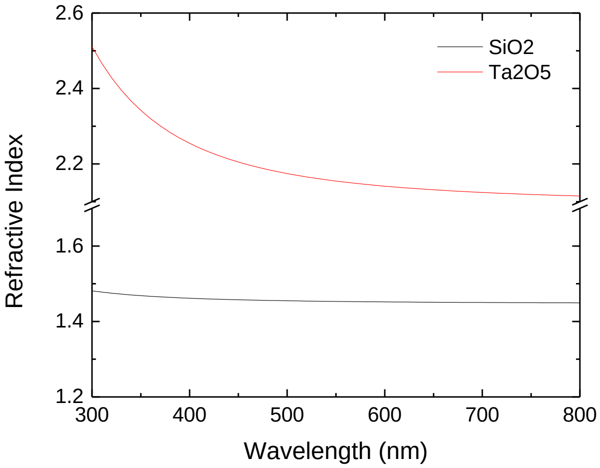

Figure 12.6 Refractive index versus wavelength of SiO_2 and Ta_2O_5 materials based on SE measurements.

The Reflectivity of the top-DBR was estimated based on the refractive index values measured with SE and compared with the experimental data, as illustrated in Figure 12.7. The refractive index of

Sapphire was taken again from reference [98]. The characteristic thicknesses of the 10 alternating deposited pairs, fabricated in France, were $t_{e\text{-}gunSiO2} = 65.5 \pm 0.5$ nm and $t_{e\text{-}gunTa205} = 40.2 \pm 0.5$ nm for the SiO2/Ta2O5 pair, with the center of the top-DBR mirror located at $\lambda_{exper} \sim 381.0$ nm. As it is visible in Figure 12.8, which shows the reflectivity of the full cavity for the nominal thickness of the membrane, the cavity mode of the full structure is located at $\lambda_c = 371.2$ nm and seems to be much weaker than that described in Figure 12.4. This probably arises due to higher reflectivity value of top-DBR based on the larger index-difference. To overcome this, one has to reduce the number of the top-DBR pairs, in our case N < 10.

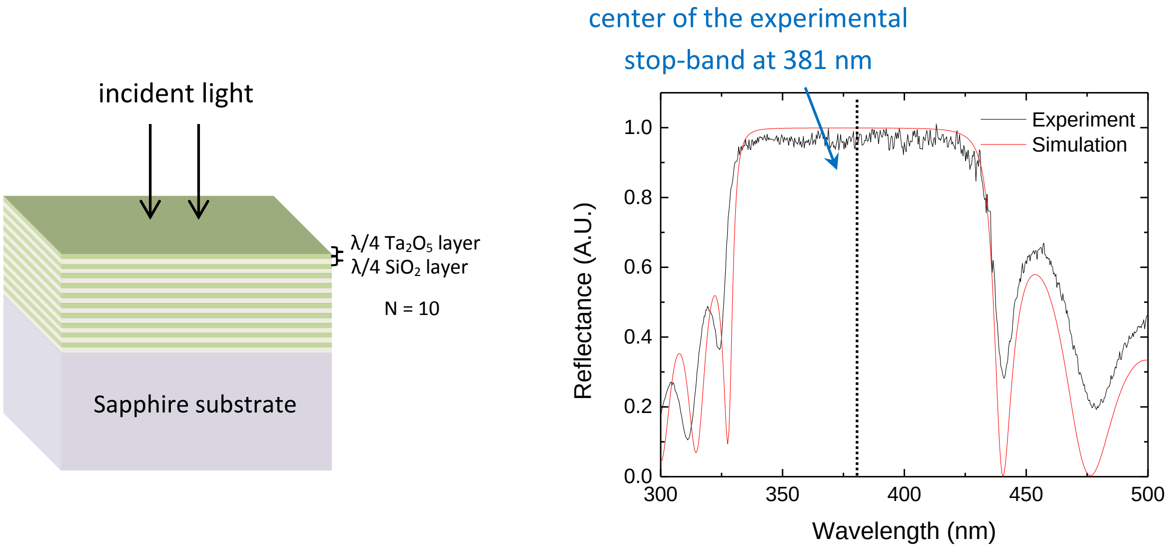

(a) **(b)**

Figure 12.7 (a) Illustration showing the 10 period alternating pairs of top's DBR layers on Sapphire substrate and (b) experimental and simulation data of Reflectance for the top-DBR mirrors.

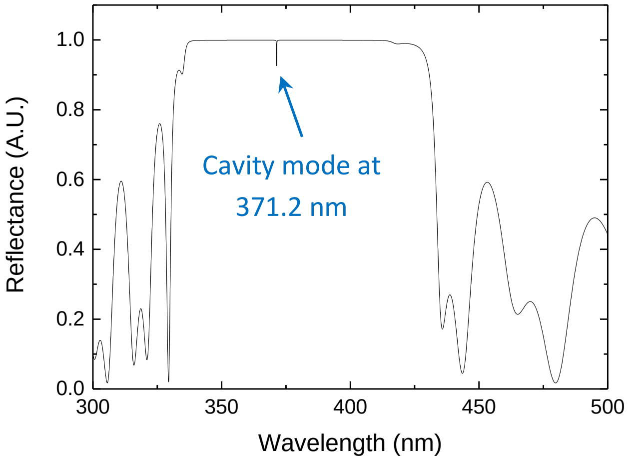

Figure 12.8 Full-microcavity reflectance simulation by using the theoretical thicknesses for the membrane layers, while the DBR thicknesses were based on the previous simulations. The cavity mode is located at $\lambda_c = 371.2$ nm.

Before doing any PL measurements, we observed the samples with an optical microscope to locate the membranes and check their quality. The resulted images presented in Figure 12.9, show that the membranes are slightly tilted in respect to the z-axis and do not fully adhere to the substrate plane. As measured in PL, the cavity mode could not be observed at any microcavity. In order to understand the reason why, we examined other membranes transferred on bottom-DBR substrates for further characterization. As was referred earlier, and will be explained in the next section, an E3364 membrane thickness was measured based on SEM at 232 nm, confirming the deviation that was observed by XRD analysis. Therefore, a new simulation of Reflectance for the 230-membrane thickness took place, as presented in Figure 12.10. As can be seen, the previous mentioned cavity mode is now shifted at higher wavelengths, λ_c = 386.7 nm, and a secondary cavity mode appears at λ_{c2} = 345.7 nm.

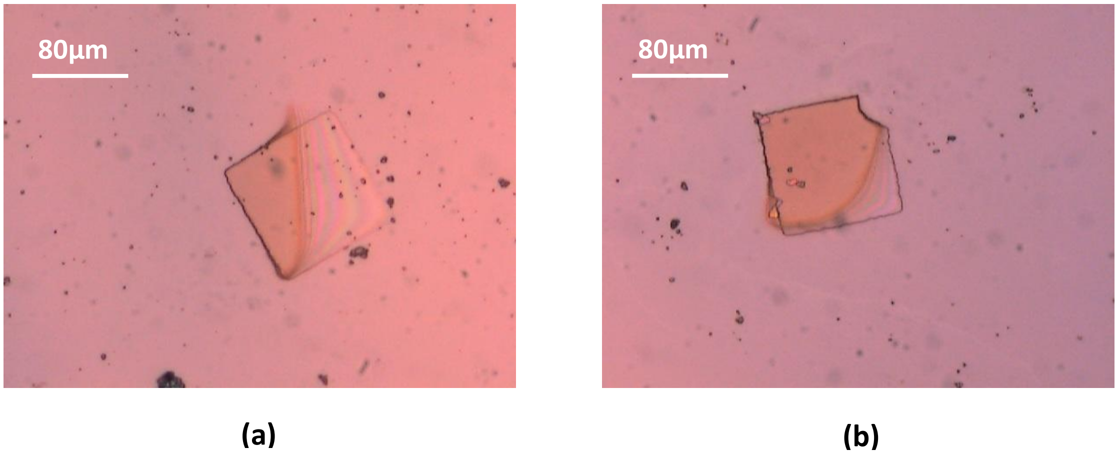

Figure 12.9 Optical images of membranes after e-gun deposition of top-DBR mirror. As can be observed optically, the membranes seem to have an inclination in respect to the substrate plane due to different colorization coming from the focused light.

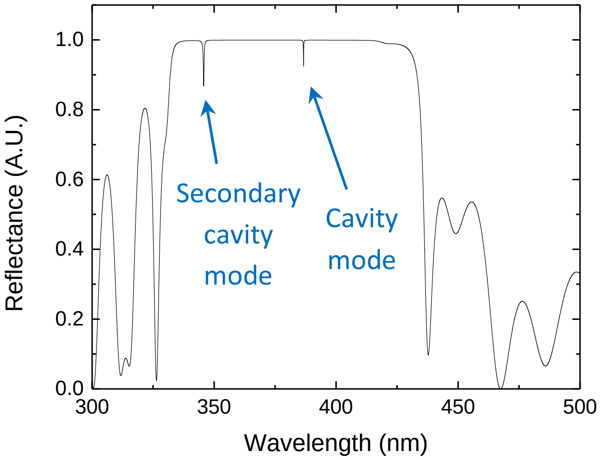

Figure 12.10 Full-microcavity reflectance simulation by using 232 nm membrane thickness, while the top- and bottom-DBR thicknesses were based on the previous simulations. The cavity mode is shifted at λ_c = 386.7 nm and a secondary mode appears at λ_{c2} = 345.7 nm.

13. Effect of membrane and air-gap thickness on cavity mode

13.1. SEM characterization and simulations of membrane thickness

Since it was difficult to observe the cavity mode in our devices, we tried to take a more careful look on the thickness of the membranes. This was achieved by doing SEM on a single membrane of the E3364 sample (Fig. 13.1), which was transferred on a bottom-DBR/Sapphire template, as well as, by Reflectivity simulations, based on the Matlab code, for various thicknesses. For the latter, the range was between – 20 up to 20 % (Fig 13.2) of the nominal cavity layer thickness, which was $L_{c\text{-ideal}}$ = 211.2 nm.

As seen in Figure 13.1 (b), the thickness of the specific memrbane was measured $L_{c\text{-SEM}}$ ~ 232 nm. Apart from SEM characterization, profilometry measurement was previously performed on the same membrane, which gave a $L_{c\text{-prof}}$ ~ 245 nm thickness. These results, further validate the earlier shown XRD data for the as-grown samples, which in the case of E3364 the total thickness was $L_{c\text{-XRD}}$ ~ 234.1 nm. Profilometry of an E3365 membrane gave a value of $L_{c\text{-prof-E3365}}$ ~ 240 nm (no SEM was performed here), confirming again the increased thickness that was found in XRD analysis ($L_{c\text{-XRD-E3365}}$ ~ 228.6 nm). By carefully observing the Figure 13.1 (b), we can see that the rms roughness of the membrane is maintained at low value. Previous work in our group showed that an rms of 0.6 nm can be achieved by utilizing the same etching process for the free-standing membrane fabrication [88].

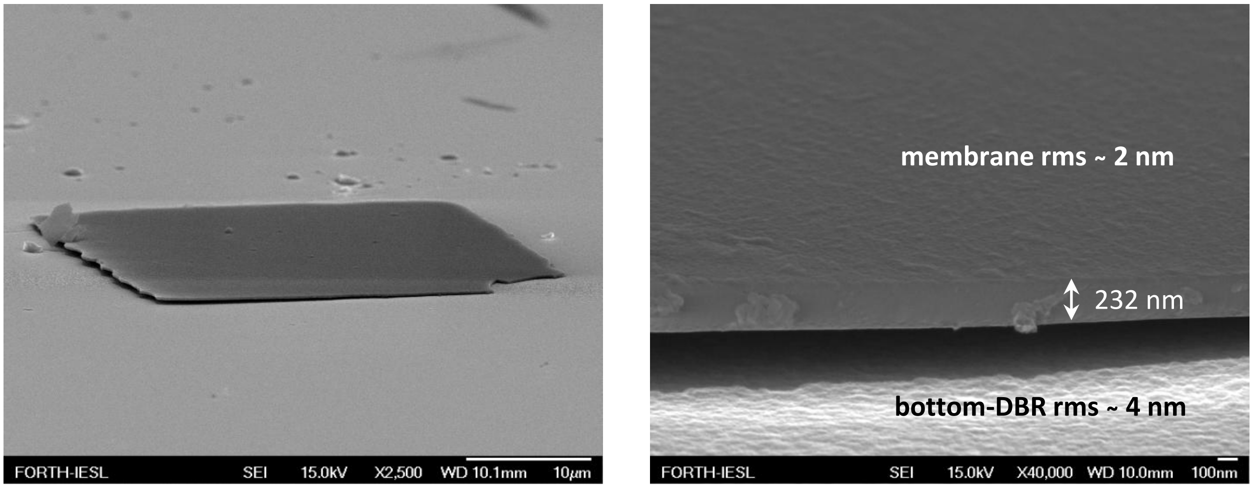

(a) **(b)**

Figure 13.1 SEM image of a single membrane from E3364 sample, which was transferred on a bottom-DBR/Sapphire template at (a) 10 μm and (b) 100 nm scale. The obtained membrane thickness based on SEM is $L_{c\text{-SEM}}$ ~ 232 nm as pointed with the white arrows.

The underlying gap and the small crack in one of the corners of the membrane, as shown in Figure 13.1, were caused during profilometry measurements. The force from the tip and/or electrostatic interactions moved the membrane in another position of the template, while wrong manipulation of it led to breaking a part. The lifting of the membrane, of several hundrend nanometers from the left side, was attributed to some broken piece or dirt underneath. Nevertheless, strain effects due to lattice mismatch between GaN and AlGaN materials should not be excluded from the overal observed curvature.

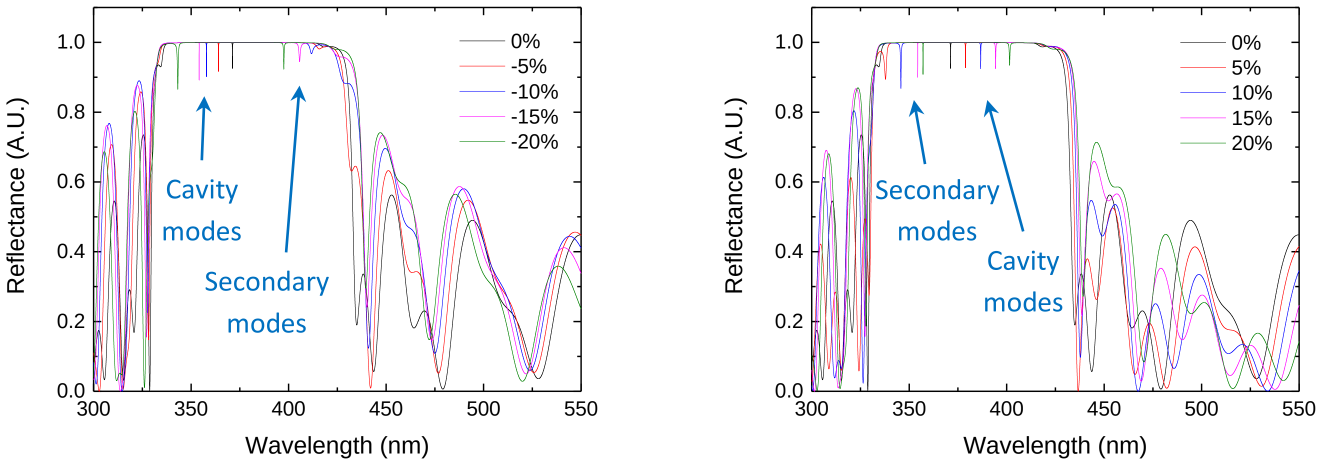

(a) **(b)**

Figure 13.2 Simulation of Reflectance for (a) 0 to - 20 % smaller and (b) 0 to + 20 % higher membrane thicknesses (L_c) based on e-gun DBR. The 0 % (black color) represents the nominal value of membrane thickness at 211.2 nm having no deviation in both cases.

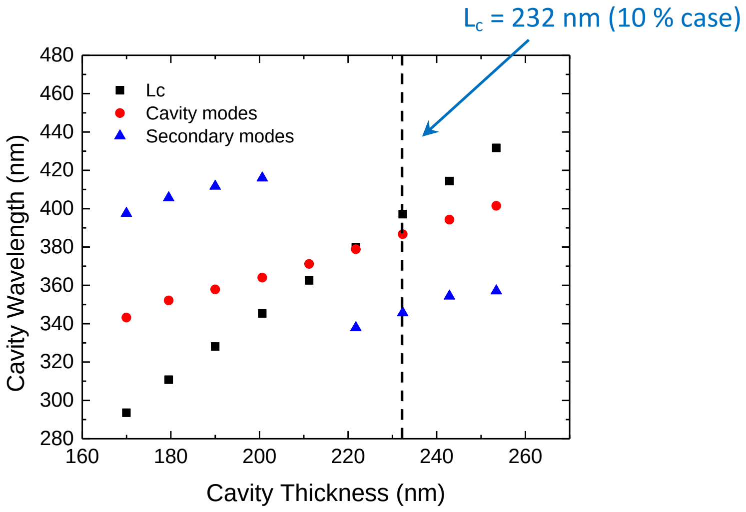

Figure 13.3 Cavity wavelength versus cavity thickness considering the effect of the DBR mirror length (L_{DBR}) to the total thickness. Above and below the designed thickness of 211.2 nm, secondary cavity modes arise at lower and higher wavelengths inside the stop-band region (blue color). The black line indicates the thickness of E3364 at 232 nm (10 % case) based on SEM.

As concerns the simulations, it was found that the previously mentioned increased thicknesses of the cavity layer (L_c) in combination with the DBR mirrors exhibit in all cases cavity modes inside the stop-band of the Reflectance spectra. This outcome is accepted by considering the significant contribution from the penetration of the electric field inside the DBR mirrors (L_{DBR}), which is responsible for the total effective length of the cavity mode, as was referred earlier in theory. Particularly for the E3364 membrane, the L_c = 232 nm value corresponds to 10 % higher thickness than the nominal value (blue color in Fig 13.2), therefore, results in a cavity mode based on simulations at 386.7 nm. On the other hand, the prediction accounting only for L_c would result in a cavity mode at 397.2 nm. Last but not least, even for the 20 % case, which should result in a cavity mode at 431.7 nm, the simulated mode is at 401.5 nm (green color in Figure 13.2).

13.2. Simulations of Reflectance by varying air-gap thickness

In this part, as the title reveals, a theoretical approximation based on simulation for various air-gap thicknesses took place. As shown before, if a broken piece of the same or from another membrane is underneath the membrane, which is under examination, it will create an inclination of the membrane in respect with the z-axis. Therefore, an estimation of the cavity mode shift had to be performed in order to understand this influence for different values of air-gap thickness, since the membranes did not adhere to the surface (Fig. 13.1). In addition, three values of membrane thicknesses (L_c) were used in the simulations of Reflectance, namely, 220, 230 and 240 nm in order to consider all the possible combinations corresponding to our samples (Fig. 13.5).

The outcome of these simulations (Fig 13.5) is summarized in Figure 13.4 showing the variation of air-gap for each value of L_c. As seen from the plot, the air-gap thickness range was from 0 up to 250 nm. The reason for using these values was to simulate the case where a broken piece of similar height as the membrane is placed underneath. This can result in a gradient of air-gap thicknesses similarly to the range that we used. All the previous can be supported by the SEM results shown earlier. By carefully looking at the data, it can be understood that a high number of cavity modes can coexist inside the stop-band of the DBR. Following this result, the superposition of FWHMs, coming from each one of these modes, will result in a new cavity mode of a very low Q-factor. This could explain our failure of observing a cavity mode in our structures.

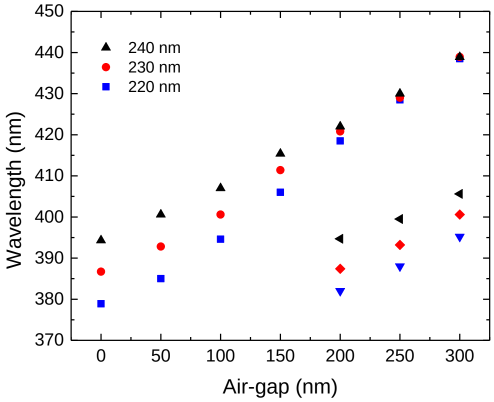

Figure 13.4 Simulation of the cavity mode versus air-gap thickness for three values of L_c = 220, 230 and 240 nm. As the air-gap increases, the three cavity modes tend to converge to a Bragg mode and new cavity modes arise at lower wavelengths inside the stop-band region.

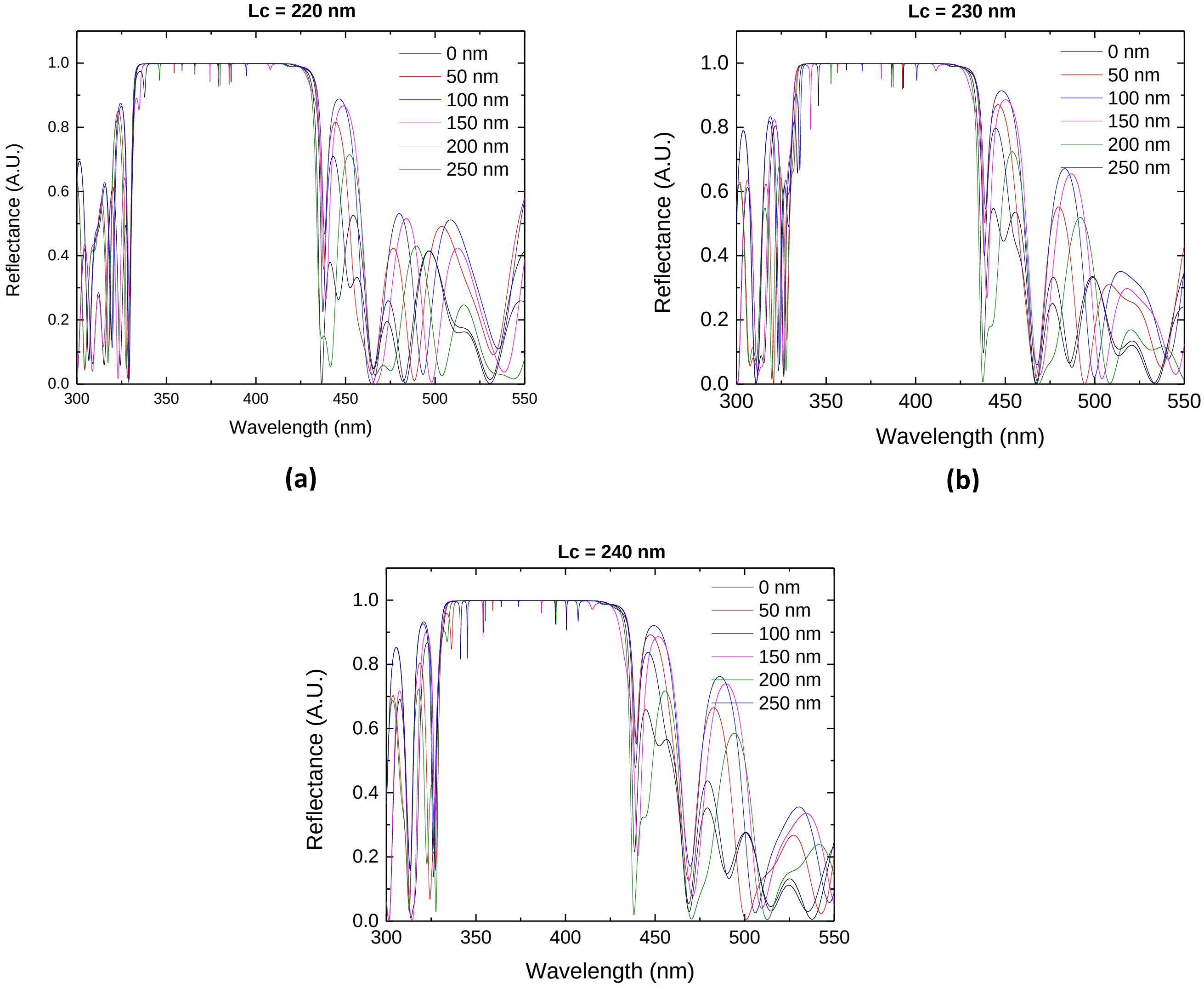

(a)

(b)

(c)

Figure 13.5 Simulation of Reflectance versus air-gap thickness for a membrane thickness (L_c) of (a) 220 nm, (b) 230 nm and (c) 240 nm. Black colored data illustrate the nominal value without any air-gap underneath.

Moreover, in the case where thicker impurities, perhaps coming from residual oxides, are mistakenly or accidentally placed under the membranes, they would create even worse issues than the previous. The inclination will be much higher then, and light could easily escape from the open sides instead of being confined between the two DBR mirrors. Based on optical images in Figure 12.9, it is considered that we had also this problem apart from having slightly titled membranes due to broken pieces. Observing the membranes prior to top-DBR growth, can be done only with the optical microscope, which makes it difficult to estimate small variations in inclination. SEM characterization cannot be used before growth, since the deposited metal has to be removed from the membranes. However, this may cause other kind of problems which would result in damaging the membranes.

14. Summary

Summarizing the above, we designed and tried to fabricate a $3\lambda_c/2$ microcavity by implementing high-quality AlGaN membranes with two sets of 4 QWs embedded inside. The QWs were positioned at the two antinodes of the electric field in order to investigate the strong coupling regime when these membranes are sandwiched by two distributed Bragg reflectors (DBRs). The Aluminum content, in the AlGaN layer, was selected to be around 7 % to reduce any lattice mismatch and strain effects. Our samples, named as E3364 and E3365, were grown by molecular beam epitaxy (MBE) on c-Sapphire substrates by the CEA group in France.

Various characterization techniques were utilized to characterize our samples such as XRD, PL, RFL, SEM, AFM, SE and Profilometry. Furthermore, temperature dependent measurements took place by the use of a Hellium-cooled cryostat with an attached heater and connected to a temperature meter. The excitation of the structures was done by a He - Cd cw laser for the PL and a Deuterium - Halogen white lamp source for the RFL, respectively. The resulting data for the QW exciton states showed a deviation from Varshni's empirical relation due to exciton localization at low temperatures. In particular, the obtained localization energies based on the fitting curve were 21.1 meV and 23.6 meV for E3364 and E3365, respectively. Apart from that, the evolution of A_x exciton versus temperature, and it's merging with the B_x exciton, were analyzed up to room temperature. By mapping the samples in PL, it was observed that the InGaN layer, in both as-grown samples, had a variation between 1 – 1.5 % in Indium concentration along the sample's surface. The first and second LO-phonons of the maximum peak were visible and located at energy distances ~ 91 and ~ 182 meV.

Moreover, simulations were performed to confirm the experimental data by the use of Nextnano software and a TMM Matlab code written in our group, according to which, deviations from the theoretically designed structures were confirmed, as the total thicknesses of the membranes were found to be ~ 10 % higher than the nominal ones. As regards DBR mirrors, the variations in layer thicknesses were found to be not that significant. In addition, simulations based on 8x8 k.p perturbation theory of A_x and B_x exciton states inside the GaN/AlGaN QWs showed very good agreement (< 0.5 nm error) to the ones from RFL measurements. Polarization fields arising from piezoelectric and spontaneous polarizations, due to lattice mismatch and wurtzite symmetry, they were also taken into consideration, since by acting on the wells, they tend to reduce the emission energies of the exciton states.

To continue, membranes were fabricated by laterally etching of the sacrificial InGaN layer with the use of Photo-electrochemical (PEC) wet etching method on pre-patterned rectangular mesas. Besides this, a first trial towards making various size cylindrical microdisks in one of the samples was attempted with the same method for exploring the whispering gallery modes (WGMs). For the PEC process, a 405 nm diode laser was used for the lateral selective etching of the InGaN layer. Three most promising characteristic times for etching our membranes were in the range 35 – 40 min. Membranes, from all time extents, were possible to be detached from the original substrates. Therefore, they were transferred on bottom-DBR/Sapphire substrates, which were made by alternating pairs of high and low refractive indices, in order to be sandwiched by the top-DBR mirror. On the other hand, microdisks were not removed from their original substrates, since no mirror deposition was necessary.

For the top-DBR deposition, two promising growth methods were utilized, namelly as rf-sputtering and e-gun evaporation. The growth of the top mirrors was made in France, in collaboration again with the CEA group. Refractive indices and thicknesses of the dielectric materials were extrapolated from SE measurements for more accurate simulations of the manufactured DBR mirrors. From the two methods, e-gun evaporation concluded to be a better technique, as rf-sputtering resulted in membrane cracking. Based on AFM, mirror quality was found to exhibit very good results in both techniques, since rms roughness was measured to be unexpectedly low. Additionally, by using the TMM model, the simulated RFL spectra of the DBR mirror layers were in accordance with our experimental data, especially for the layers grown on Si substrate.

Nevertheless, it was not possible to make a working polariton device, since it was difficult to observe any well-defined cavity modes in our microcavities. In the samples made by rf-sputtering, the membranes were cracked and, in some cases, the broken pieces had left away. On the contrary, e-gun evaporation showed better mirror-quality, but it was indicated that the membranes did not adhere to the bottom-DBR surface. An inclination of the membranes was observed due to some residues or broken pieces of membranes underneath them. Hence, a very huge number of cavity modes can coexist covering most of the range of the stop-band region, meaning that light can conveniently escape from the open sides of the tilted membrane. More analytically, by considering the superposition of FWHMs of all the existing cavity modes inside the stop-band, we are led to a really low Q-factor. Thus, photons will not be possible to stay long enough inside the cavity and they will have a very short lifetime.

Appendix A

k.p perturbation theory

To calculate the band structure of a material in the vicinity of band extrema or extrapolate the whole Brillouin zone, one has to account k.p perturbation theory. This is done by using the Hamiltonian of a periodic structure

$$H = \frac{p^2}{2m_o} + V(r) \quad \text{(A1)}$$

where $V(r) = V(r+R)$ and $p = \frac{\hbar}{i}\nabla$. By inserting the Bloch wavefunction $\varphi_{nk}(r) = e^{ikr}u_{nk}(r)$ in the time-independent Schrödinger equation, it yields

$$\left(\frac{p^2}{2m_o} + \frac{\hbar^2 k.p}{m_o} + \frac{\hbar^2 k^2}{2m_o} + V(r)\right)u_{n,k}(r) = E_n(k)u_{n,k}(r) \quad \text{(A2)}$$

For k=0 the above relation simplifies to

$$\left(\frac{p^2}{2m_o} + V(r)\right)u_{n,0}(r) = E_n(0)u_{n,0}(r) \quad \text{(A3)}$$

Assuming that the solution for k=0 is known, we can use the terms $\frac{\hbar^2 k.p}{m_o}$ and $\frac{\hbar^2 k^2}{2m_o}$ in equation A2 as perturbations of first and second order in k. The dispersion relation for a non-degenerate band is given by

$$E_n(k) = E_{n,o} + \frac{\hbar^2 k^2}{2m_o} + \frac{\hbar^2}{{m_o}^2}\sum_{n\prime\neq n}\frac{|\langle u_{n,0}|k.p|u_{n\prime,0}\rangle|^2}{E_{n,o}-E_{n\prime,o}} \quad \text{(A4)}$$

From equation A4, it is easy to deduce the relation for effective mass of the conduction band n shown below as

$$\frac{1}{m_e} = \frac{1}{m_o} + \frac{2}{{m_o}^2k^2}\sum_{n\prime\neq n}\frac{\langle u_{n,0}|k.p|u_{n\prime,0}\rangle}{E_{n,o}-E_{n\prime,o}} \quad \text{(A5)}$$

k.p perturbation arises from the coupling between the various bands and depends on the momentum matrix element which is related to the dipole matrix element. This coupling modifies the effective mass by adding a second term to the relation A5.

From the previous, it can be obtained that the appearance of the effective mass is a consequence of level repulsion between the bands and the coupling between them from the k.p term.

Appendix B

Quality factor (Q)

When describing optical cavities, one of the very common cavity parameters, the well-known quality factor (Q), is of high importance since it gives information about the photon lifetime τ_{ph}, corresponding to the time-dependent solution of the energy dissipated from a cavity. In essence, it means how much time a photon of the cavity mode stays in the microcavity before it escapes. Hence, larger values of the quality factor force photons to stay more time inside the resonator. The mathematical definition of the quality factor is shown below.

$$Q = \frac{\omega_o E_c}{P_{loss}}$$

where E_c is the energy stored in the cavity, ω_o is the resonant frequency and P_{loss} the power dissipated by the cavity. In the case that there is no photon source inside the cavity, the expression for the P_{loss} is

$$P_{loss} = -\frac{dE_c}{dt}$$

Combining the above equations, they give a time dependent differential equation

$$\frac{dE_c}{dt} = -\frac{\omega_o}{Q} E_c$$

which yields a solution of the form

$$E_c(t) = E_c(0) e^{-\frac{\omega_o t}{Q}}$$

The factor $\frac{Q}{\omega_o}$ in the above solution is defined as the photon lifetime τ_{ph}. When time is analyzed into frequencies by using the Fourier transformation, another formula of the quality factor can be used and for large values it can be approximated by

$$Q \approx \frac{\omega_o}{\delta\omega} \; or \; \frac{\lambda_o}{\delta\lambda}$$

where ω_o (λ_o) is again the resonant frequency (wavelength) and $\delta\omega$ ($\delta\lambda$) is the full width at half maximum (FWHM) of the resonant peak. For an ideal cavity Q - factor goes to infinity ($Q \to \infty$).

Another important parameter is the free spectral range (FSR), which is defined as the frequency separation between two adjacent cavity modes. The expression is as follows

$$FSR = \Delta\lambda = \lambda_m - \lambda_{m+1} \approx \frac{{\lambda_{m+1}}^2}{2Ln_g cos\theta}$$

where n_g is the group refractive index, L is the cavity length and θ is the angle of incidence.

Last but not least, there is the Finesse (F), which is defined as the ratio of the FSR to the resonant linewidth, as follows

$$F = \frac{FSR}{\delta\lambda} = \frac{\Delta\lambda}{\delta\lambda} = \frac{\pi\sqrt{R}}{1-R} \approx \frac{\pi(R_1R_2)^{\frac{1}{4}}}{1-(R_1R_2)^{\frac{1}{2}}}$$

where R_1 and R_2 the reflectivity coefficients of the front and back mirror, respectively. Cavities with high Finesse values show sharper transmission peaks. The physical explanation of the Finesse is the round trip number of the photon in the cavity. Transmittance and reflectance of cavity for arbitrary angle of incidence are given by the following formula

$$T = \frac{(1-R_1)(1-R_2)}{[1-\sqrt{R_1R_2}]^2 + 4\sqrt{R_1R_2}\sin^2\delta}$$

$$R = \frac{[1-\sqrt{R_1R_2}]^2 + 4\sqrt{R_1R_2}\sin^2\delta - (1-R_1)(1-R_2)}{[1-\sqrt{R_1R_2}]^2 + 4\sqrt{R_1R_2}\sin^2\delta}$$

where $\delta = \left(\frac{2\pi}{\lambda}\right) 2n_g L \cos\theta$.

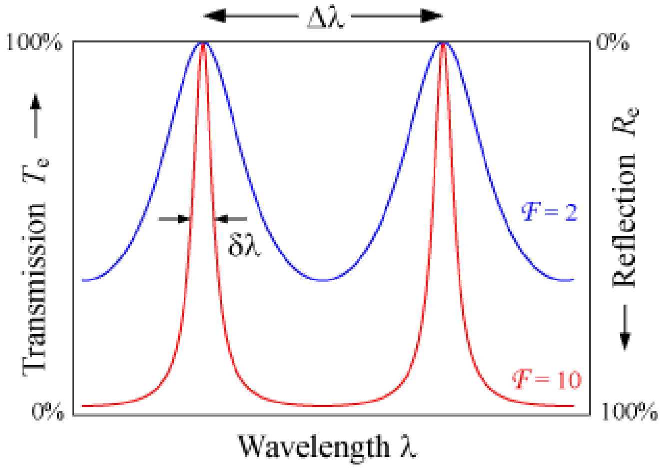

Figure B.1 Transmission and Reflectance spectra corresponding to different Finesse values [100]

Appendix C

Transfer matrix method (TMM)

By taking into account that when light is travelling through a medium with a refractive index n changes its wavelength we need a proper model describing this phenomenon in DBRs where we have N pairs of alternating layers without solving Maxwell's equations analytically every time. This model is known as transfer matrix method and it uses the matrix formulation to express light's electric and magnetic field characteristics when passing through a layer with a refractive index n_i and thickness d_i. Similar formulation is used when extracting Fresnel equations for the electromagnetic waves. Solving Maxwell equations for electric and magnetic fields being perpendicular to each other and using the boundary conditions we can derive Fresnel's equations. Maxwell equations in vacuum where the current density vector J = 0 and the charge density ρ = 0 are reduced to

$$\nabla\, x\, E = -\frac{\partial B}{\partial t}$$

$$\nabla\, x\, B = +\frac{1}{c^2}\frac{\partial E}{\partial t}$$

$$\nabla\, .\, E = 0$$

$$\nabla\, .\, B = 0$$

where E is the electric field, B is the magnetic field vector and c = $2.99\text{x}10^8$ m/s the speed of light in vacuum. Solutions of these equations can be considered plane waves of the form

$$E = E_o\, e^{i[k(n'.r)-\omega t]} \text{ and } B = B_o\, e^{i[k(n'.r)-\omega t]}$$

where k = 2π/λ is the wave vector, n' = n_xi+n_yj+n_zk the unit vector, r = xi+yj+zk the space vector and ω = 2π/T the angular velocity and υ = ω/k the phase velocity (for light υ = c). At this point it should be noted that these plane waves follow the superposition principle and that the components of E and B are related by

$$|B| = \frac{n}{c}|E|, \qquad where\; n = 1\; for\; vacuum$$

When a wave is incident on a surface or interface of a different medium, a part of it will be reflected and the rest of it will be transmitted through until it finds another interface to interact again and so on. An incident plane wave (TE or TM mode) is taken to hit a plane and by applying the boundary conditions at the interface for both electric and magnetic field one may find the amplitudes of the reflected and transmitted waves. In simple words, the tangential components must be equal for the E and B before and after the plane for each interface. The result of all the above is summarized below in a matrix form for m interfaces

$$\begin{pmatrix} E_{m,d=t} \\ n_m B_{m,d=t} \end{pmatrix} = M_m \ldots\ M_1 \begin{pmatrix} E_{1,d=0} \\ n_1 B_{1,d=0} \end{pmatrix}$$

where M_m is the M_L or M_H depending on the stack of layers eg. H-L-H-L or L-H-L-H.

$$M_m = \begin{pmatrix} \cos(\delta_m) & \dfrac{i\sin(\delta_m)}{\gamma_m} \\ i\gamma_m \sin(\delta_m) & \cos(\delta_m) \end{pmatrix} \text{ with } \mathrm{\delta_m} = \mathrm{k_m d_m} = \frac{(2\pi n_\mathrm{m} \mathrm{d_m} \cos(a_\mathrm{m})\ )}{\lambda}$$

Depending on the polarization we can distinguish the following main cases

$$\gamma_\mathrm{m} = n_\mathrm{m} \cos(a_\mathrm{m})\ for\ TE$$

$$\gamma_\mathrm{m} = \frac{n_\mathrm{m}}{\cos(a_\mathrm{m})} for\ TM$$

In the case where m is an absorbing layer it yields

$$\cos(a_\mathrm{m}) = \frac{\sqrt{n"^2_m - n_1^2 \sin^2(a_0)}}{n"_m}\ \ with\ n"_m = n_m - ik_m$$

Distributed Bragg Reflectors (DBRs) are a multiple dielectric layer structure consisting of alternating high and low refractive indices with a thickness of each layer being one quarter of wavelength. Thus, the product k.d equals to π/2 and the matrix for N bilayers ($M_H M_L$) becomes

$$M_{DBR} = \left(\begin{pmatrix} 0 & \dfrac{i}{\gamma_H} \\ i\gamma_H & 0 \end{pmatrix} \begin{pmatrix} 0 & \dfrac{i}{\gamma_L} \\ i\gamma_L & 0 \end{pmatrix} \right)^N = \begin{pmatrix} \left(-\dfrac{\gamma_L}{\gamma_H}\right) & 0 \\ 0 & \left(-\dfrac{\gamma_H}{\gamma_L}\right) \end{pmatrix}^N \text{for any angle of incidence}$$

The complete matrix M of an incident beam from the air to the DBR on a substrate is

$$M = \begin{pmatrix} M_{11} & M_{12} \\ M_{21} & M_{22} \end{pmatrix} = D_{air}^{-1}\ M_{DBR}\ D_{substrate}$$

where D_i are the refraction matrices and hence, Reflectance of the DBR is equal to

$$R = |r|^2 = |\frac{M_{21}}{M_{11}}|^2$$

where r is the Fresnel coefficient and M_{ij} are the matrix elements.

Appendix D

Fourier plane imaging ($k_{//}$ space)

Imaging of the Fourier plane emission pattern of a polariton device can be accomplished, since the internal polariton eigenmodes are coupled to cavity photons, and hence, they emit photoluminescence. To analyze and image the emitted spectrum on the slit of the spectrometer, a microscope objective with a high value of NA is utilized. The higher the value of the NA, the higher the range of angles that can be observed in the $k_{//}$ space image. The magnification (M) of the configuration is defined by the ratio of the imaging lens focal length f and the microscope objective focal length f_o. Moreover, at the output of the spectrometer, a CCD camera is used to record the spatial and spectral PL data with the angle resolution depending on the pixel size.

In Figure D.1 is illustrated the experimental setup for both real and Fourier plane imaging in order to explain the difference between the two configurations. Depending on the position of the imaging lens, as presented in the figure, it is possible to image the PL of the real plane from a spot area (upper case) or the PL of the Fourier plane for a number of angles, of a specific spot, determined by the NA (lower case). The Fourier plane is formed at a focal distance f_o defined by the microscope objective. Nowadays there are setups containing both configurations, in which both PL data PL data can be obtained in a single measurement (not shown here). The trick for achieving this is to use an achromatic imaging lens as has been reported in reference [101].

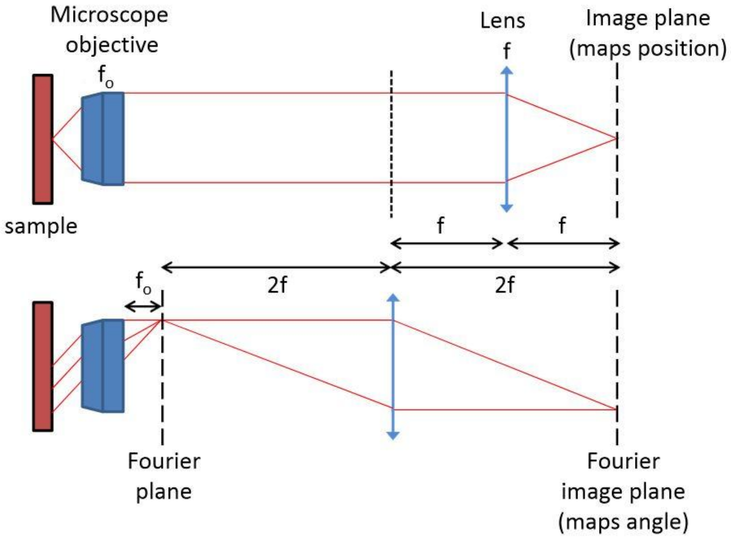

Figure D.1 Experimental configuration for imaging (a) real and (b) $k_{//}$ space emission patterns depending on the position of an imaging lens of focal length f. In the second case, Fourier plane is formed at a distance f_o of the microscope objective, where f_o is the microscope objective focal length distance [102].

Bibliography

1. **Alexey V. Kavokin, Jeremy J. Baumberg, Guillaume Malpuech and Fabrice P. Laussy.** *Microcavities.* s.l. : Oxford University Press, 2007.

2. *Review Article Optical Microcavities.* **Kerry J. Vahala.** 2003, Nature, Vol. 424, pp. 839-846.

3. *Room-temperature continuous-wave lasing in GaN/InGaN microdisks.* **Adele C. Tamboli, Elaine D. Haberer, Rajat Sharma, Kwan H. Lee, Shuji Nakamura & Evelyn L. Hu.** 2007, Nature Photonics 1, pp. 61-64.

4. *Bose–Einstein condensation of excitons polaritons.* **J. Kasprzak, M. Richard, S. Kundermann, A. Baas, P. Jeambrun, J. M. J. Keeling, F. M. Marchetti, M. H. Szymanska, R. André, J. L. Staehli, V. Savona, P. B. Littlewood, B. Deveaud & Le Si Dang.** Nature, Vol. 443, pp. 409-414.

5. *Nonequilibrium condensates and lasers without inversion: Exciton-polariton lasers.* **A. Imamoglu, R. J. Ram, S. Pau, and Y. Yamamoto.** 1996, Physical Review A, Vol. 53, pp. 4250-4253.

6. *An electrically pumped polariton laser.* **Christian Schneider, Arash Rahimi-Iman, Na Young Kim, Julian Fischer, Ivan G. Savenko, Matthias Amthor et al.** 2013, Nature, Vol. 497, pp. 348-352.

7. *Room Temperature Electrically Injected Polariton Laser.* **Pallab Bhattacharya, Thomas Frost, Saniya Deshpande, Md Zunaid Baten, Arnab Hazari and Ayan Das.** 2014, Physical Review Letters, Vol. 112, pp. 236802-1.

8. *The method of effective electron mass in crystals.* **S. Pekar.** 1946, Zhurnal Eksperimental'noi i Teoreticheskoi Fiziki, Vol. 16, p. 933.

9. *Motion of Electrons and Holes in Pertrubed Periodic Fields.* **J. M. Luttinger and W. Kohn.** 1955, Physicsl Review, Vol. 97, pp. 869-883.

10. **Stefan Birner.** [Online] Nextnano software . http://www.nextnano.de/nextnano3/.

11. *Temperature dependence of the energy gap in semiconductors.* **Y. P. Varshni.** 1967, Physica, Vol. 34, pp. 149-154.

12. *Spontaneous polarization and piezoelectric constants of III-V nitrides.* **F. Bernardini, V. Fiorentini, and D. Vanderbilt.** 1997, Physical Review B, Vol. 56, pp. R10024-R10027.

13. *A versatile phenomenological model for the S-shaped temperature dependence of photoluminescence energy for an accurate determination of the exciton localization energy in bulk and quantum well structures.* **V. K. Dixit, S. Porwal, S. D. Singh, T. K. Sharma, Sandip Ghosh and S. M. Oak.** 2014, Journal of Physics D: Applied Physics, Vol. 47, p. 065103.

14. *Transfer Matrix Method in Nanophotonics.* **Ryan B. Balili.** 2012, International Journal of Modern Physics: Conference Series, Vol. 17, pp. 159-168.

15. *GaN, AlN and InN: A review.* **S. Strite and H. Morkoç.** 1992, Journal of Vacuum Science & Technology B, Vol. 10, pp. 1237-1266.

16. [Online] http://ellipsometry.unl.edu/research/Exchange-Polarization1.php.

17. *GaN Growth Using Gan Buffer Layer.* **Shuji Nakamura.** 1991, Japanese Journal of Applied Physics, Vol. 30, pp. 1705-1707.

18. *Structural, optical and electrical study of undoped GaN layers obtained by metalorganic chemical vapor deposition on Sapphire substrates.* **Victor-Tapio Rangel-Kuoppa, Cesia Guarneros Aguilar and Victor Sanchez-Resendiz.** 2011, Thin Solid Films, Vol. 519, pp. 2255-2261.

19. *Photoluminescence and Raman studies of GaN fimls grown by MOCVD.* **Luong Tien Tung, K L Lin, E Y Chang, W C Huang Y L Hsiao and C H Chiang.** 2009, Journal of Physics: Conference Series , Vol. 187.

20. **Joachim Piprek.** *Nitride Semiconductor Devices: Principles and Simulation.* s.l. : WILEY-VCH Verlag GmbH & Co. KGaA, 2007.

21. *High- Resolution Photoluminescence and Reflectance Spectra of Homoepitaxial GaN layers.* **K. Kornitzer, T. Ebner, M. Grehl, K. Thonke, R. Sauer, C. Kirchner, V. Schwegler, M. Kamp, M. Leszczynski, I. Grzegory and S. Porowski.** 1999, Physica Status Solidi (b), Vol. 216, pp. 5-9.

22. *First-principles calculations of effective-mass parameters of AlN and GaN.* **Masakatsu Suzuki, Takeshi Uenoyama and Akira Yanase.** 1995, Physical Reviews B, Vol. 52, p. 8132.

23. *Absorption coefficient, energy gap, exciton binding energy, and recombination lifetime of GaN obtained from transmission measurements.* **J. F. Muth, J. H. Lee, I. K. Shmagin, R. M. Kolbas, H. C. Casey et al.** 1997, Applied Physics Letters, Vol. 71, pp. 2572-2574.

24. *Growth and properties of GaxAl1-xN compounds.* **J. Hagen, R. D. Metcalfe, D. Wickenden and W. Clark.** 1978, Journal of Physics C, Vol. 11, pp. L143-6.

25. *Growth and properties of AlxGa1-xN Epitaxial Layers.* **B. Baranov, L. Daweritz, V. B. Gutan, G. Jungk, H. Neumann and H. Raidt.** 1978, Physica Status Solidi A, Vol. 29, pp. 629-636.

26. *Optical properties of InxGa1-xN alloys grown by metalorganic vapor deposition.* **W. Shan, W. Walukiewicz and E. E. Haller.** 1998, Journal of Applied Physics, Vol. 84, pp. 4452-4458.

27. *Vegard's law deviation in band gaps and bowing parameters of the wurtzite III-nitride ternary alloys.* **Bo-Ting Liou, Sheng-Horng Yen and Yen-Kuang Kuo.** 2005, Semiconductor Lasers and Applications II, Vol. 5628, pp. 296-305.

28. *High electron mobility GaN/Al x Ga1−x N heterostructures grown by low-pressure.* **M. Asif Khan, J. M. Van Hove, J. N. Kuznia and D. T. Olson.** 1991, Applied Physics Letters, Vol. 58, pp. 2408-2410.

29. **Takafumi Yao and Soon-Ku Hong.** *Oxide and Nitride Semiconductors: Processing, Properties and Applications.* s.l. : Springer, 2009.

30. *First-principles investigation of lattice constants and bowing parameters in wurtzite AlxGa1-xN, InxGa1-xN and InxAl1-xN alloys.* **Z Dridi, B Bouhafs and P Ruterana.** 2003, Semiconductor Science and Technology, Vol. 18, pp. 850-856.

31. *Photoluminescence Investigations of AlGaN on GaN Epitaxial Films.* **B. K. Meyer, G. Steude, A. Goldner, A. Hoffmann, H. Amano and I Akasaki.** 1999, Physica Status Solidi (b), Vol. 216, pp. 187-191.

32. **Pierre Ruterana, Martin Albrecht and Jörg Neugebauer.** *Nitride Semiconductors: Handbook on Materials and Devices.* s.l. : WILEY-VCH Verlag GmbH & Co. KGaA, 2003.

33. *Study of the Polarizations of (Al,Ga,AlGa)N Nitride Compounds and the Charge Density of Various Interfaces Based on Them.* **I. A. Supryadkina, K. K. Abgaryan, D. I. Bazhanov and I. V. Mutigullin.** 2013, Semiconductors, Vol. 47, pp. 1621-1625.

34. *Spontaneous and piezoelectric polarization effects in III-V nitride heterostructures.* **E. T. Yu, X. Z. Dang, P. M. Asbeck, S. S. Lau and G. J. Sullivan.** 1999, Journal of Vacuum Science & Technology B, Vol. 14, pp. 1742-1749.

35. *Piezoelectric charge densities in AlGaN/GaN HFETs.* **P. M. Asbeck, E. T. Yu, S. S. Lau, G. J. Sullivan, J. Van Hove and J. M. Redwing.** 1997, Electronics Letters, Vol. 33, pp. 1230-1231.

36. *Photoluminescence Study of Piezoelectric Polarization in Strained AlxGa1-xN/GaN Single Quantum Wells.* **V. Kirilyuk, P. R. Hageman, P. C. M. Christianen, F. D. Tichelaar and P. K. Larsen.** 2001, Physica Status Solidi (b), Vol. 228, pp. 563-566.

37. *Giant electric fields in unstrained GaN single quantum wells.* **R. Langer, J. Simon, V. Ortiz, N.T. Pelekanos, A. Barski, R. André and M. Godlewski.** 1999, Applied Physics Letters, Vol. 74.

38. *Measurement of piezoelectrically induced charge in GaN/AlGaN heterostructure field-effect transistors.* **E. T. Yu, G. J. Sullivan, P. M. Asbeck, C. D. Wang, D. Qiao, and S. S. Lau.** 1997, Applied Physics Letters, Vol. 71, pp. 2794–2796.

39. *Influence of the substrate grade on structural and optical properties of GaN/AlGaN superlattices.* **F. Schubert, S. Zybell, J. Heitmann, T. Mikolajick and S. Schmult.** 2015, Journal of Crystal Growth, Vol. 425, pp. 145-148.

40. *Optimization of optical gain in AlxGa1-xN/GaN/AlxGa1-xN strained quantum well laser.* **A. Asgari and S. Dashti.** 2012, Optik, Vol. 123, pp. 1546-1549.

41. *Electronic properties and optical-absorption spectra of GaAs-AlxGa1-xAs quantum wells in externally applied electric fields.* **G. D. Sanders and K. K. Bajaj.** 1987, Physical Review B, Vol. 35, pp. 2308-2320.

42. *Temperature dependence of exciton life-time in GaAs/AlGaAs quantum wells.* **S. K. Pandey, M. Ramrakhiani and B. P. Chandra.** 2003, Indian Journal of Pure & Applied Physics, Vol. 41, pp. 719-722.

43. [Online] http://www.physik.hu-berlin.de/sfb951/program/topics-1/topic3.

44. *On the Transformation of light into Heat in Solids. I.* **J. Frenkel.** 1931, Physical Review, Vol. 37, p. 17.

45. **Vladimir M. Agranovich.** *Excitations in Organic Solids.* s.l. : Oxford university press, 2008.

46. *The Structure of Electronic Excitation Levels in Insulating Crystals.* **G. Wannier.** 1937, Physical Review, Vol. 52, p. 191.

47. **H. Haug and S. W. Koch.** *Quantum Theory of the Optical and Electronic Properties of Semiconductors.* s.l. : World Scientific, 2009. p. 216.

48. [Online] http://web.missouri.edu/~ullrichc/research.htm.

49. *Photoluminescence characteristics of AlGaN-GaN-AlGaN quantum wells.* **M. A. Khan, R. A. Skogman, J. M. Van Hove, S. Krishnankutty and R. M. Kolbas.** 1990, Applied Physics Letters, Vol. 56, pp. 1257-1259.

50. *Polarization effects in photoluminescence of C- and M- plane GaN/AlGaN multiple quantum wells.* **E. Kuokstis, C. Q. Chen, M. E. Gaevski, W. H. Sun, J. W. Yang, G. Simin, M. Asif. Khan, H. P. Maruska, D. W. Hill, M. C. Chou, J. J. Gallagher and B. Chai.** 2002, Applied Physics Letters, Vol. 81, pp. 4130-4132.

51. *Effect of n-type modulation doping on the photoluminescence of GaN/Al0.07Ga0.93N multiple quantum wells.* **H. Haratizadeh, P. P. Paskov, G. Pozina, P. O. Holtz, B. Monemar, S. Kamiyama, M. Iwaya, H. Amano and I. Akasaki.** 2002, Applied Physics Letters, Vol. 80, pp. 1373-1375.

52. *Effects of well thickness and Si doping on the optical properties of GaN/AlGaN multiple quantum wells.* **K. C. Zeng, J. Y. Lin, H. X. Jiang, A. Salvador, G. Popovici, H. Tang, W. Kim and H. Morkoç.** 1997, Applied Physics Letters, Vol. 71, pp. 1368-1370.

53. *Photoluminescence study of Si-doped GaN/Al0.07Ga0.93N multiple quantum wells with different dopant position.* **H. Haratizadeh, B. Monemar, P. P. Paskov, J. P. Bergman, B. E. Sernelius, P. O. Holtz, M. Iwaya, S. Kamiyama, H. Amano and I. Akasaki.** 2004, Applied Physics Letters, Vol. 84, pp. 5071-5073.

54. *Piezoelectric effects on the optical properties of GaN/AlxGa1-xN multiple quantum wells.* **H. S. Kim, J. Y. Lin, H. X. Jiang, W. W. Chow, A. Botchkarev and H. Morkoç.** 1998, Applied Physics Letters, Vol. 73, pp. 3426-3428.

55. *Well-width dependence of the ground level emission of GaN/AlGaN quantum wells.* **A. Bonfiglio, M. Lomascolo, G. Traetta, R. Cingolani, A. Di Carlo, F. Della Sala, P. Lugli, A. Botchkarev and H. Morkoç.** 2000, Journal of Applied Physics, Vol. 87, pp. 2289-2292.

56. *Exact quantum calculation of polariton dispersion in semiconductor microcavities.* **V. Savona and F. Tassone.** 1995, Solid State Communications, Vol. 95, pp. 673-678.

57. *Impact of inhomogeneous excitonic broadening on the strong exciton-photon coupling in quantum well nitride microcavities.* **G. Cristman, R. Butte, E. Feltin, J. Carlin and N. Grandjean.** 2006, Physical Review B, Vol. 73, p. 153305.

58. *Polaritons in high reflectivity microcavities: semiclassical and full quantum treatement of optical properties.* **Andreani L C, Savona V, Schwendimann P and Quattropani A.** 1994, Superlattices and Microstructures, Vol. 15, pp. 453-458.

59. *Theory of the Contribution of Excitons to the Complex Dielectric Constant of Crystals.* **J. J. Hopfield.** 1958, Physical Review, Vol. 112, pp. 1555-1567.

60. *Theoretical and Experimental Effects of Spatial Dispersion on the Optical Properties of Crystals.* **J. J. Hopfield and D. G. Thomas.** 1963, Physical Review, Vol. 132, pp. 563-572.

61. *Measurement of cavity-polariton dispersion curve from angle resolved photoluminescence experiments.* **R. Houdré, C. Weisbuch, R. P. Stanley, U. Oesterle, P. Pellandini and M. Ilegems .** 1994, Physical Review Letters, Vol. 73, pp. 2043-2046.

62. [Online] http://www.uam.es/personal_pdi/ciencias/fmarchet/research_interests.html.

63. *Radiative lifetime of free excitons in quantum wells.* **Andreani L C, Tassone F and Bassani F.** 1991, Solid State Communications, Vol. 77, pp. 641-645.

64. *Quantum well excitons in semiconductor microcavities: unified treatment of weak and strong coupling regimes.* **V. Savona, A. Quattropani. L. C. Andreani and P. Schwendimann.** 9, 1995, Solid State Communications, Vol. 93, pp. 733–739.

65. *Excitonic light reflection and absorption in semiconductor microcavities at oblique incidence.* **A. V. Kavokin and M. A. Kaliteevski.** 1995, Solid State Communications, Vol. 95, pp. 859-862.

66. *Large vacuum Rabi splitting in a multiple quantum well GaN-based microcavity in the strong-coupling regime.* **Gabriel Christmann, Raphaël Butté, Eric Feltin, Anas Mouti, Pierre A. Stadelmann, Antonino Castiglia, Jean-François Carlin and Nicolas Grandjean.** 2008, Physical Review B, Vol. 77, p. 085310.

67. *Strong coupling phenomena in quantum microcavity structures.* **M. S. Skolnick, T. A. Fischer and D. M. Whittaker.** 1998, Semiconductor Science and Technology, Vol. 13, pp. 645-669.

68. *Room temperature polariton luminescence from a GaN/AlGaN quantum well microcavity.* **E. Feltin, G. Christmann, R. Butté, J.-F. Carlin, M. Mosca and N. Grandjean.** 2006, Applied Physics Letters, Vol. 89, p. 071107.

69. *Room temperature lasing in a GaN/AlGaN multiple quantum well microcavity.* **Gabriel Christmann, Raphaël Butté, Eric Feltin, Jean-François Carlin and Nicolas Grandjean.** 2008, Applied Physics Letters, Vol. 93, p. 051102.

70. *GaN hybrid microcavities in the strong coupling regime grown by metal-organic chemical vapor deposition on sapphire substrates.* **A. Alyamani, D. Sanvitto, A. A. Khalifa, M. S. Skolnick, T. Wang, F. Ranalli, P. J. Parbrook, A. Tahraoui and R. Airey.** 2007, Journal of Applied Physics, Vol. 101, p. 093110.

71. *Room temperature polariton lasers based on GaN microcavities.* **Guillaume Malpuench, Aldo Di Carlo, Alexey Kavokin, Jeremy J. Baumberg, Marian Zamfirescu and Paolo Lugli.** 2002, Applied Physics Letters, Vol. 81, pp. 412-414.

72. *Large vacuum Rabi splitting in ZnO-based hybrid microcavities observed at room temperature.* **Jun-Rong Chen, Tien-Chang Lu, Yung-Chi Wu, Shiang-Chi Lin, Wei-Rein Liu, Wen-Feng Hsieh, Chien-Cheng Kuo and Cheng-Chung Lee.** 2009, Applied Physics Letters, Vol. 94, p. 061103.

73. *Coexistence of low threshold lasing and strong coupling in microcavities.* **Pavlos G. Lagoudakis, M. D. Martin, Jeremy J. Baumberg, Guillaume Malpuench and Alexey Kavokin.** 2004, Journal of Applied Physics, Vol. 95, pp. 2487-2489.

74. *Ultrahigh optical Q factors of crystalline resonators in the linear regime.* **Ivan S. Grudinin, Vladimir S. Ilchenko and Lute Maleki.** 2006, Physical review A, Vol. 74, pp. 063806-1.

75. *Whispering gallery resonances in semiconductor micropillars.* **V. N. Astratova, S. Yang, S. Lam, B. D. Jones, D. Sanvitto, D. M. Whittaker, A. M. Fox, M. S. Skolnick, A. Tahraoui, P. W. Fry and M. Hopkinson.** 2007, Applied Physics Letters, Vol. 91, pp. 071115-1.

76. *Ultra-high-Q tunable whispering-gallery-mode microresonator.* **M. Pöllinger, D. O'Shea, F. Warken and A. Rauschenbeutel.** 2009, Physical Review Letters, Vol. 103, pp. 053901-1.

77. *Demonstration of ultra-high-Q small mode volume toroid microcavities.* **T. J. Kippenberg, S. M. Spillane and K. J. Vahala.** 2004, Applied Physics Letters, Vol. 85, pp. 6113-6115.

78. *Spherical whispering-gallery-mode microresonators.* **Alessandro Chiasera, Yannick Dumeige, Patrice Féron, Maurizio Ferrari, Yoann Jestin, Gualtiero Nunzi Conti, Stefano Pelli, Silvia Soria and Giancarlo C. Righini.** 2010, Laser and Photonic Reviews, Vol. 4, pp. 457-482.

79. *Whispering-gallery mode microdisk lasers.* **S. L. McCall, A. F. J. Levi, R. E. Slusher, S. J. Pearton and R. A. Logan.** 1992, Applied Physics Letters, Vol. 60, pp. 289-291.

80. *Blue-green emitting microdisks using low-temperature-grown ZnO on patterned silicon substrates.* **Marcel Ruth, Thomas Zentgraf and Cedrik Meier .** 2013, Optics Express, Vol. 21, pp. 25517-25525.

81. *Exciton-phonon interactions, exciton binding energy, and their importance in the realization.* **A. K. Viswanath, J. I. Lee, D. Kim, C. R. Lee and J. Y. Leem.** 1998, Physical Review B, Vol. 58, pp. 16333-16339.

82. Wikipedia. [Online] https://en.wikipedia.org/wiki/Distributed_Bragg_reflector.

83. *Optical investigations of bulk and multi-quantum well nitride-based microcavities.* **F. Réveret, F. Médard, P. Disseix, J. Leymarie, M. Mihailovic, A. Vasson, I. R. Sellers, F. Semond, M. Leroux and J. Massies.** 2009, Optical Materials, Vol. 31, pp. 505-509.

84. *Effects of layer thickness and incident angle variations on DBR reflectivity.* **N. M. Ahmed, M. R. Hashim and Z. Hassan.** 2006, Materials Science Forum, Vol. 517, pp. 29-32.

85. *Room temperature photoenhanced wet etching of GaN.* **M. S. Minsky, M. White and E. L. Hu.** 1996, Applied Physics Letters, Vol. 68, pp. 1531-1533.

86. *Dry and wet etching characteristics of InN, AlN and GaN deposited by electron cyclotron resonance metalorganic molecular beam epitaxy.* **S. J. Pearton, C. R. Abernathy, F. Ren, J. R. Lothian, P. W. Wisk and A. Katz.** 1993, Journal of Vacuum Science & Technology A, Vol. 11, pp. 1772-1775.

87. *Bragg polariton luminescence from a GaN membrane embedded in all dielectric microcavity.* **E. Trichas, N. T. Pelekanos, E. Iliopoulos, E. Monroy, K. Tsagaraki, A. Kostopoulos and P. G. Savvidis.** 2011, Applied Physics Letters, Vol. 98, p. 221101.

88. *Ultra-smooth GaN membranes by photo-electrochemical etching for photonic applications.* **R. Jayaprakash, F. G. Kalaitzakis, M. Kayambaki, K. Tsagaraki, E. Monroy and N. T. Pelekanos.** 2014, Journal of Materials Science, Vol. 49, pp. 4018-4024.

89. *Room-temperature cavity polaritons in a semiconductor microcavity.* **R. Houdré, R. P. Stanley, U. Oesterle, M. Ilegems and C. Weisbuch.** 1994, Physical Review B, Vol. 49, pp. 16761-16764.

90. *Observation of the coupled exciton-photon mode splitting in a semiconductor quantum microcavity.* **C. Weisbuch, M. Nishioka, A. Ishikawa and Y. Arakawa.** 1992, Physical Review Letters, Vol. 69, pp. 3314-3317.

91. *Linewidths of excitonic luminescence transitions in AlGaN alloys.* **Giuliano Coli, K. K.Bajaj, J. Li, J. Y. Lin and H. X. Jiang.** 2001, Applied Physics Letters, pp. 1829-1831. 78.

92. *Energy gaps and bowing parameters of InAlGaN ternary and quaternary alloys.* **M. Androulidaki, N. T. Pelekanos, K. Tsagaraki, E. Dimakis, E. Iliopoulos, A. Adikimenakis, E. Bellet-Amalric, D. Jalabert and A. Gewrgakilas.** 2006, Physica Status Solidi (c), Vol. 3, pp. 1866-1869.

93. *Localization Effects in GaN/AlGaN Quantum Well -- Photoluminescence Studies.* **B. Chwalisz, A. Wysmołek, R. Bożek, K. P. Korona, R. Stępniewski, W. Knap, K. Pakuła, J.M. Baranowski, N. Grandjean, J. Massies, P. Prystawko and I. Grzegory.** 2003, Acta Physics Polonica A, Vol. 103, pp. 573-578.

94. *Exciton localization behavior in different well width undoped GaN/Al0.07Ga0.93N nanostructures.* **M. Sabooni, M. Esmaeili, H. Haratizadeh, B. Monemar, P. Paskov, S. Kamiyama, M. Iwaya, H. Amano and I. Akasaki.** 2007, Opto-Electronics Review, Vol. 15, pp. 163-167.

95. *Band parameters for nitrogen-containing semiconductors.* **I. Vurgaftman and J. R. Meyer.** 2003, Journal of Applied Physics, Vol. 94, pp. 3675-3696.

96. *Selective photochemical etching for GaN films and laser lift-off for microcavity fabrication.* **E. Trichas, C. Xenogianni, M. Kayambaki, P. Tsotsis, E. Iliopoulos, N. T. Pelekanos and P. G. Savvidis.** 2008, Physica Status Solidi (a), Vol. 205, pp. 2509-2512.

97. *Free-standing, optically pumped, GaN ⁄ InGaN microdisk lasers fabricated by photoelectrochemical etching.* **E. D. Haberer, R. Sharma, C. Meier, A. R. Stonas, S. Nakamura, S. P. DenBaars and E. L. Hu.** 2004, Applied Physics Letters, Vol. 85, pp. 5179-5181.

98. Refractive index database. [Online] http://refractiveindex.info/.

99. *University of Reading.* [Online] http://www.reading.ac.uk/ir-infraredmaterials-si.aspx.

100. Wikipedia. [Online] https://en.wikipedia.org/wiki/Fabry%E2%80%93P%C3%A9rot_interferometer.

101. **Jacek Kasprzak.** *Condensation of exciton polaritons.* 2006.

102. **Gaël Nardin.** *Phase - Resolved imaging of Exciton Polaritons.* 2011.